UNIVERSITÀ DEGLI STUDI DI
CASSINO E DEL LAZIO MERIDIONALE

Corso di Dottorato in
Metodi, modelli e tecnologie per l'ingegneria

curriculum Ingegneria Civile e Meccanica

Ciclo XXXIV

Analysis and modelling of innovative technologies on natural gas transportation and distribution networks

SSD: ING/IND 10

Coordinatore del Corso
Chiar.mo Prof. Marco Dell'Isola

Dottorando
Linda Moretti

Supervisore
Chiar.mo Prof. Fausto Arpino

A Renato

ACKNOWLEDGEMENTS

This thesis represents the end of a profound human and professional experience, result of a research work that would not have materialised without the intellectual input and the support of great researchers. Many people dedicated me their time for review and discussion and provided me with indispensable help for the achievement of this academic aim. To all those, I express my sincere gratitude.

I would like to thank my supervisors and all professors with which I had the opportunity to collaborate, for guiding me along this journey and for all the moments of useful discussion we had along this path.

First of all, I would like to thank the professor Marco Dell'Isola for believing in my possibilities and giving me the opportunity to undertake this prestigious journey. I thank him for the significant guidance provided. The trust placed in me and his human and professional teachings are an expertise that I will always carry with me.

I would like to thank the professor Fausto Arpino for his persistent help and his valuable cooperation, as well as for his availability in all circumstances and his incessant attention to details.

I would like to thank the professor Giorgio Ficco for patiently proofreading my work on collaboration opportunities, teaching me the scientific rigour and the intellectual integrity.

I would also like to thank the professor Alessandra Perna for giving me the chance to collaborate with her on an interesting engineering research topic, as well as for dedicating me her time for teaching me a new subject.

All of them provided me with substantial support for the publication of this thesis and of numerous research articles. I am infinitely grateful for them who share with me this academic path allowing me to growth professionally and humanly.

Finally, I would like to acknowledge with gratitude, the support and the love of my partner, Renato, my parents and my brother, who all kept me going through this journey.

Without all these contributes, this thesis would not have been possible.

ABSTRACT

Renewable energy sources (RESs), such as wind, solar and biomass, are the keystone of the energy policy of the EU to fulfil the target of a carbon neutral economy by 2050 [1]. However, the integration of a significant share of RESs pose significant challenges to the EU energy systems as it requires, on the one hand, storing large energy volumes to match intermittent renewable supply with the pattern of energy consumption and, on the other hand, transporting renewable energy from where it can be most efficiently and feasibly produced to where it is consumed.

To overcome such challenges, it will be effective to consider the reuse of the existing natural gas (NG) infrastructure. The latter will play a crucial role in the development of a decarbonized energy system based on a large usage of RESs due to its widespread presence and its capacity to provide a cost-effective option for transporting and storing large amounts of energy for long-term period exploiting the NG transportation and distribution networks, as well as the storage complexes of the existing NG infrastructure.

This thesis aims to address, with a multi-thematic approach, the issue of innovative uses of, as well as the development of innovative technologies on, NG transport and distribution networks. To this aim, a number of five case studies were investigated to: i) evaluate the fault management strategies for NG distribution networks to minimize the disservice and to define possible structural improvement measures; ii) assess the technical feasibility of the Power to Gas concept to store intermittent RESs; iii) analyse the impact of hydrogen injection on NG networks; iv) evaluate the effectiveness of the equilibrium gasification models as a modelling tool for the design and optimization of biomass gasification systems integrated into polygenerative plants coupled with energy networks.

Results of this thesis provide useful insights to researchers, designers and policy makers, filling some of the gaps highlighted in the existing scientific literature in all the analysed areas.

TABLE OF CONTENTS

LIST OF FIGURES

LIST OF TABLES

INTRODUCTION

To move towards a low-carbon economy and to comply with commitments under the Paris Agreement, the European Union (EU) has set ambitious binding climate and energy targets for 2030. By 2050, the EU aims for 80 – 95 % of emissions reduction targets, but also declare its aspiration to meet higher ambition levels, by adopting the 2018 EU Long Term Greenhouse Gas Emissions (GHGs) reduction strategy with the view to achieve net-zero GHGs emissions by 2050, as announced in the plan for European Green Deal.

Renewable energy sources (RESs), such as wind, solar and biomass, are the keystone of the energy policy of the EU to fulfil the target of a carbon neutral economy by 2050 [1]. According to the European Directive 2018/2001 on the promotion of the use of energy from renewable sources, Member States shall collectively ensure that the share of energy from RESs in the EU's gross final consumption of energy is at least 32% by 2030 [2]. Such a percentage has been recently judged to be not sufficient to reach the goals set in the EU Long Term Strategy. Therefore, the European Commission has started to review the old regulatory packages relating to climate change. It is expected that the new renewable energy directive will set an increased target, in which 40% of the European final energy consumption should come from RESs by 2030 [3].

However, the integration of a significant share of RESs pose significant challenges to the EU energy systems as it requires, on the one hand, storing large energy volumes over weeks, months and seasons, to match intermittent renewable supply with the pattern of energy consumption and, on the other hand, transporting renewable energy from where it can be most efficiently and feasibly produced to where it is consumed, encompassing both long-distance transports.

To overcome such challenges, it will be effective to consider the reuse of the existing natural gas (NG) infrastructure. The latter will play a crucial role in the

development of a decarbonized energy system based on a large usage of RESs due to its widespread presence and its capacity to provide a cost-effective option for transporting and storing large amounts of energy for long-term period exploiting the NG transportation and distribution networks, as well as the storage complexes of the existing NG infrastructure.

NG infrastructure has historically been designed to bridge long distances between production points and consumption ones at low cost and with low energy losses. The current European NG transportation system is wide-ranging and well-established, in addition to having a transmission capacity that greatly exceeds electricity transmission grid capacity. Similarly, European NG distribution system is extensive and existing. Within the EU almost half of household end-energy consumers are connected to the gas distribution network. On EU average, the volume delivered via the distribution grid to households is around four times higher for gas than for electricity. Also, the storage capacity of European NG infrastructure is larger than electricity storage volume. Thus, due to its inherent features, NG infrastructure can help to handle the challenges of transport and storage of RESs in the short and medium term.

On the other hand, the existing NG infrastructure is suited for the transport of renewable gases, such as biomethane, hydrogen and substitute natural gas. The use of existing NG infrastructure for the injection and the transport of renewable gases, mixed or, in the future, also pure, as in the case hydrogen, can help to achieve the goals of the decarbonisation and the integration between the electricity and gas sectors, as indicated in the 2020 EU Strategy for Energy System Integration.

An interlinkage between the gas and electricity systems based on synergies between these two energy carriers (i.e., Power to gas) will provide benefits to the whole energy system, in particular:

i. integration of RESs: maximised integration of renewable energy, especially non-programmable RESs;
ii. flexibility: growing shares of RESs electricity generation make the electricity system exposed to weather patterns; this creates the need for back up and short- and long-term flexibility technologies working in the base load and ensuring the hourly to seasonal balance between production and

demand; gas decarbonisation technologies can bring the required flexibility for balancing the variable input from wind and photovoltaic power generation units;

iii. sector coupling: the electricity system and the gas system should be seen as complementary; the electric system allows for the production of large quantities of renewable energy but has challenges with regards providing long-term energy storage, handling peak production and consumption as well as facilitating long-distance transportation;

iv. sectoral integration: hydrogen and Power to Gas (PtG) will bring renewable energy into other sectors where substantial amounts of energy are required and where some processes are otherwise difficult or expensive to electrify;

v. cybersecurity: risks could be higher in an all-electricity system; the two energy systems together will offer more resilience, more time to react and better options to recover when needed;

vi. robust system: an integrated energy system will provide a higher level of security of supply and better integration of renewables in general, due to the capabilities on long term, seasonal gas storage and peak production and demand.

Depending on the evolution of hydrogen, biomethane and synthetic natural gas supply potential and user demand, NG infrastructure functioning will change, depending also on Member States' choice of technologies (e.g., P2G, biomethane, etc.) best serving their national needs and circumstances. The future EU energy system will have to combine the specificities of each Member State or region intending to make best use of their potential, whilst achieving the decarbonisation targets in a cost-effective manner.

In the above-described context, it is clear how NG gas infrastructure can play a central role to meet decarbonisation targets, obtain flexibility, storage options, cross-border transportation capacities and security of supply in the most efficient way. Nevertheless, to effectively promote an optimal management and an innovative use of the existing NG infrastructure, as well as the development of innovative technologies on natural gas transportation and distribution networks, the support for technologies to

mature will be needed, especially as regards the following research topic, which will be all analysed within the framework of the present research:

i. methods and tools for the optimized management of NG transport and distribution networks;
ii. impact of the injection of renewable gases into NG transport and distribution networks;
iii. technologies for the production of renewable gases.

Aim of the work

The present research aims to address some of the gaps in the current scientific literature concerning the subject of innovative uses of NG transport and distribution networks, which have been described in the above introductory section. The different topics have been approached from different perspectives. For this reason, the chapters of the thesis have been compiled in a thematic way and consistently with the candidate's research experiences.

In the following, an overview about the research outline together with the thesis structure will be given in order to allow a clear understanding during the reading of the present work.

Research outline and thesis structure

The thesis is organized in four main thematic chapters, each containing an introductory section in which the scientific relevance of the research topic and the gaps in current scientific literature are highlighted.

Chapter 1 addresses the problem of NG networks management in the event of fault occurrence through the application of resilience concept. An overview about the definition of resilience for Critical Infrastructures and the state of the art of methodologies for the resilience assessment of NG networks and the analysis of a case study (*case study #1*) is provided. In *case study #1*, a novel a resilience assessment methodology for NG distribution networks able to simulate fault conditions leading to quality-of-service issues and to disservice is proposed and described. The proposed methodology is experimented in case of a real distribution network and the results is presented and discussed.

Chapter 2 is dedicated at evaluating the technical feasibility of the PtG concept to store intermittent RESs. After the description of the current state of the art of core technologies in the PtG process, two different case studies are analysed and discussed. In *case study #2*, a PtSNG plant coupled with a RES facility is designed and investigated by evaluating nominal and annual efficiencies for different sizes of the electrolysis unit. Specifically, a detailed and comprehensive simulation model for PtSNG system analysis under steady state and dynamic operation is provided and useful criteria for the PtSNG systems design and sizing are defined. In *case study #3*, a novel thermal management strategy for a PtSNG plant and how it impacts on the annual plant performances is analysed.

Chapter 3 presents an overview of the effect of hydrogen injection on NG networks. The analysis of impact of hydrogen injection on the reliability of measuring devices that currently run on the existing NG infrastructures, both from a theoretical and an experimental point of view, is proposed as *case study #4*. In detail, a comprehensive analysis of the changes of thermo-physical properties, when gases with different hydrogen content are used, is carried out, as well as of the theoretical effects on the accuracy of volume conversion at standard conditions. The impact of the hydrogen injection on the accuracy of static ultrasonic domestic gas meters is also experimentally investigated and the related results is presented and discussed. Finally, the impacts of hydrogen injection on NG quality measurements are discussed from a theoretical point of view.

Finally, *Chapter 4*, is aimed at evaluating the reliability of the equilibrium gasification models currently available in the scientific literature to establish whether they can be employed to build new control and optimization schemes and operating maps of biomass gasification systems integrated into polygenerative plants coupled with energy networks. In particular, the main objective consists in the assessment of thermodynamic equilibrium models as a function of biomass type and composition to better understand in which conditions of practical interest such models con be applied with acceptable reliability. To this aim, a thermodynamic equilibrium model using a simulation tool implemented is described (*case study #5*) and applied to the simulation

of different biomasses gasification, employing experimental data available in the scientific literature.

CHAPTER 1. ANALYSIS OF RESILIENCE OF NATURAL GAS NETWORKS

1.1 Defining resilience for Critical Infrastructures

European Union Critical Infrastructures (CIs) include those physical resources, services, and information technology facilities, networks, and infrastructure assets which, if disrupted or destroyed, would have a serious impact on the health, safety, security or economic well-being of citizens or the effective functioning of governments [4]. CIs can be damaged, destroyed or disrupted by deliberate acts of terrorism, natural disasters, negligence, accidents or computer hacking, criminal activity, and malicious behaviour. To save the lives and property of people at risk, any disruption or manipulation of CIs should be, to the extent possible, brief, infrequent, manageable, geographically isolated, and minimally detrimental to the welfare of the state and its citizens.

It is therefore necessary that such infrastructural systems are highly reliable and safe. In other words, it is imperative that CIs are highly resilient to potential threats. In order to develop action plans that efficaciously assure the resilience of CIs, it is crucial to define the concept of resilience to make it operational and subsequently, to quantify it using a suitable metric [5].

The term resilience is derived from the Latin word *resilĭens – ĕntis*, the present participle of *resilīre* meaning "bounce back". The concept was, for the first time in academic research, employed by Holling to denote the ability of ecological systems to absorb change and disturbance maintaining the same relationships between populations or state variables within the systems themself [6]. Since that time, several definitions of the notion of resilience have been proposed in a wide range of disciplines ranging from environmental research to materials science and engineering, psychology, sociology, and economics [7]. Even though the consensus view is that the definition introduced by Holling have significantly influenced the common usage of the term resilience, a univocal definition applicable indiscriminately to the various

research areas has not proposed still now. But the notion changes according to the discipline and application domain [5,8].

In the engineering domain, the concept of resilience implies different attributes depending on the specific system analysed and the scope of analysis, as can be deduced by comparing the different definitions from engineering literature, policy directives and academic community.

Bruneau et al. [7] defined the seismic resilience of physical systems as the ability to reduce the occurrence of a shock, to absorb a shock if it occurs and to recover quickly after a shock, identifying four main attributes of resilient systems: i) robustness; ii) rapidity; iii) resourcefulness; iv) redundancy. The US Department of Homeland Security denoted the resilience as the capacity of a system or network to resist, absorb, recover from, or successfully adapt to adversity or a change in conditions [9]. The National Infrastructure Advisory Council (NIAC) similarly stated that the effectiveness of a resilient infrastructure depends upon its ability to anticipate, absorb, adapt to and/or rapidly recover from a potentially disruptive event [10]. The American Society of Mechanical Engineers (ASME) defined the engineering resilience as the capability of a system to sustain external and internal disruptions without discontinuity of performing the system's function or if the function is disconnected, to fully recover the function rapidly [11]. According to Haimes [12], the resilience of a system is the ability to withstand a major disruption within acceptable degradation parameters and to recover within an acceptable time and composite costs and risks. Vugrin et al. [13] defined the resilience of a system to a particular disruptive event (or set of events) as the ability to efficiently reduce both the magnitude and duration of the deviation from targeted system performance levels. Alessandri and Filippini [14] regarded the resilience of network of interconnected systems as a sort of structural property, more precisely the ability to resist to internal drift and cascading failures, and recover back to the initial operation state. Lately, Hollnagel et al. [15] introduced the notion of engineering resilience defining it as the ability of a system to keep, or recover quickly to, a safe stable state, allowing it to continue operations during and after a major mishap or in the presence of continuous significant stresses. Erker et al. [16] presented the concept of regional energy resilience as the preservation and protection of the basic functions of living (i.e., housing, working, supply and mobility) within an energy region despite an immediate disruptions.

Based on all of the abovementioned definitions, resilience can be denoted as the response of a system to a disruptive event and its behaviour throughout the response time. For the infrastructure systems, the response to a disruption is represented by the

state of service supplied by the system. Thus, in this case, resilience describes the extent of disruption across multiple dimensions including quality, time, and geography of service provision. The state of service resulting from a disruptive event is determined by the nature of disruptive event itself, design of the system, and mode in which the system is operated. Such factors impact on the time of disruption and rate of service decrease, as well as the duration of disruption and the rate and extent of recovery. A key aspect of resilience emphasized by some authors is the speed of recovery. In this sense, it is deemed that the increasing speed of recovery is associated with a greater resilience of the system. Moreover, it can be observed that some definitions, such as the one proposed by ASME [11], underline the need of system to restore the performance level previous to the disruptive event; conversely, other definitions do not entail that the system returns to the pre-disaster state. Lastly, note that resilience as a concept is often related to other concepts as reliability, robustness, recoverability, sustainability, redundancy.

The growing interest in the CIs resilience, both within academic field and infrastructure system management, denotes that resilience is considered a promising concept to better understand and improve the performance of complex and highly inter-connected infrastructures that are indispensable for the functioning of our modern society and the products and services it depends on. Contextually, the system's complexity, the exchange of goods, services, information and people and the risk of disruptive events have increased. This continues to rise calls for a methodological approach that in a consistent and comprehensive manner can contribute to successfully master future challenges.

1.2 Title Literature review on resilience analysis of natural gas networks

The literature on resilience analysis of NG pipeline systems is not extensive. As reported by Liu and Song [17], such topic has not been widely investigated and more emphasis on risk and vulnerability assessment of NG pipeline network systems rather than resilience one has given in the academic field.

Esposito et al. [18] investigated the physical impact of L'Aquila 2009 earthquake on the performance of the local medium and low pressure NG distribution networks. To this aim, the authors assessed the resilience of the system as the integral area of functionality recovery curve defined by the number of users supplied/disrupted from the time of shock to that at which the pre-event level of performance is fully recovered.

Ellison et al. [19] assessed the resilience of the NG network to a potential NG outages in a ShakeOut scenario earthquake. The consequences to the overall infrastructure from the failure of components have been analysed using a network model. Carvalho et al. [20] analysed the response of the European NG pipeline system to supply shortages in case of human conflict, geopolitical crises, terrorist attacks and natural disasters. A resilient response strategy has been presented and its effectiveness has been quantified for several scenarios. In particular, a network has been considered resilient to a scenario if the vectors of country throughput per capita for the scenario and the baseline scenario are similar. Cimellaro et al. [21] proposed a performance assessment methodology for NG distribution networks, which includes the restoration phase right after an extreme event to evaluate the resilience index of the entire network. The proposed resilience index has been defined as the normalized shaded area underneath the functionality curve of the system analysed, which has been determined as a combination of the normalized gas flow rate and the total length of the network in service before and after the disruptive event. Golara et al. [22] developed a comprehensive model for NG networks resilience estimation under natural disasters such as earthquakes and fires, or artificial hazards such as deliberate attacks on the system. To evaluate the resilience of the NG network, an index measuring delivery importance of the system has been suggested. In particular, the delivery importance has been quantified through the amount of NG distributed to fixed nodes in a given time period. Wadhawan et al. [23] investigated the resilience of the NG pipeline systems under different cyber-physical attack scenarios using a time-related index that is the time required by a network to reach the failure state and to define the system performance afterward a cyber-attack. Hauser et al. [24] evaluated the resilience of the northeast German NG pipeline system during critical situations. For this purpose, a detailed model of pipelines, storages, border points and exit points of the system has been developed and a cost minimization approach has been used to investigate demand utilisation of NG infrastructure and curtailment of demand on two representative days. Kyriakidis et al. [25] employed a simulation approach to quantify a resilience metric of a NG distribution network and, more generally, a critical infrastructure. Specifically, two recovery metrics of resilience has been examined: the first metric consists in the time to recover to 100 % level of service, whereas the second one consists in the integral loss of service. The results have indicated that the former is a rather poor measure, and it does not represent well the integral loss of service. Su et al. [26] developed a supply resilience analysis based on an integrated dynamic model that has been used to evaluate the ability of NG pipeline networks to maintain stable

supply of gas for customers. The proposed method allows evaluating the capacities of the overall system and customers to withstand disturbances and recover to an equilibrium state. Marino and Zio [27] developed an original resilience analysis framework for a complex NG pipeline transmission network considering the cybernetic interdependence of the physical gas pipeline network with the SCADA system. In this study, the resilience of the NG networks has been quantified using the robustness and recoverability indices that are based on the integration of the area under a resilience function between different time intervals.

Based on the literature review, one of challenges integral to assess the resilience of complex infrastructural systems, such as NG pipeline systems, is the development a holistic methodology able to take into account multiple factors, such as geometrical and topographic characteristic of the system, type of the fault, consumption scenario, recovery strategy etc., that impact on the state of service resulting from an unpredictable event. In the following paragraph, a resilience assessment methodology for acquiring, simulating, and processing the impact of failures on NG distribution networks. The aim of the proposed methodology is to evaluate the behaviour and fragility of distribution networks, under different fault scenarios and network structures, as well as to evaluate the fault management strategies to minimize the disservice and to define possible structural improvement measures.

1.3 *Case study #1: A resilience analysis simulation tool for natural gas distribution networks*

1.3.1 Theory and methods

The proposed resilience analysis methodology is based on a software framework that is able to assess the impacts of these faults on the network itself, starting from possible faults that could affect the quality of service of a NG distribution network. Specifically, the methodology allows to: i) evaluate the behaviour and fragility of the network under different fault scenarios and assets (e.g., summer, winter, day, night); ii) identify possible critical areas with end-users out of services (e.g., too high or too low pressures, flow reduction, flow interruption) or danger to citizens; iii) evaluate the operational recovery strategies to minimize the inefficiency necessary for the drafting of intervention plans to guarantee a safer and more efficient service; iv) evaluate selectively any structural improvements of the network to reduce the risk of faults and to improve its resilience (e.g., increase in the redundancy of components, the meshing

of the network, the segmentation of the control). Figure 1.1 represents the proposed methodology.

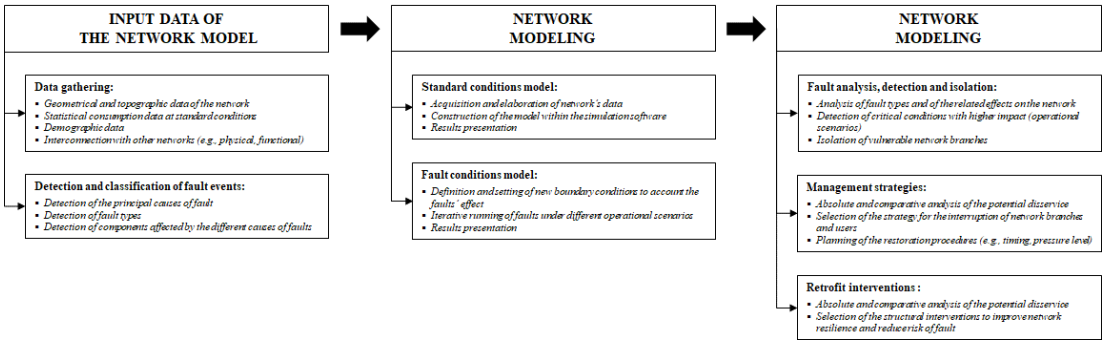

Figure 1.1 – Schematic representation of the recovery strategy model.

One of the inputs of the framework is represented by the geo-referenced map of the network containing both structural (e.g., position, length and diameter of the pipes) and technical information (e.g., material of the tubes, PRPs, valves). Indeed, a NG distribution network is constituted of a number of (generally underground) pipelines that starting from physical supply and/or interconnection points allow the delivery to residential, technological, and industrial end-users. From a structural point of view, NG distribution networks mainly consist of a series of City Gates plants (i.e., pressure regulation and measurement at the border with the transport network), highly branched distributed pipelines connecting adjacent nodes and supplying end-users, PRPs, redelivery points (RDPs, i.e., the physical network points, at which the distribution company redelivers gas to the user, and where gas is metered). In particular, the nodes represent: i) entry points where the gas enters into the system (City Gates); ii) points where the gas is delivered to end-users (RDPs); iii) points where a pipeline undergoes a change in diameter, or it is split into two or more branches. An important source of data of the framework is represented by the network GIS maps developed by the distribution operators as they use GIS maps for planning and to analyse the risk of actions (for example, laying underground cables, excavations and earthmoving) that can affect the functionality of the network [28]. However, GIS maps almost always represent exclusively the underground medium/low pressure distribution networks. Whereas, the last section of the above-ground redelivery network, on which the supply meters of end-users are installed, it is not represented in GIS tools. Consequently, the terminal nodes traced on the GIS maps represent groups of redelivery points (i.e., they represent group of end users) and, generally, they do not refer to single RDP except for large users. Therefore, one of the most critical points of the network modelling

196 activity is represented by the accurate representation of end-users and citizens served
197 by individual nodes. For this purpose, to measure the impact of a failure on citizens
198 served at each node of the network, an updated demographic model, developed in Italy
199 by ISTAT (Italian National Statistics Institute), was associated with the network GIS
200 Model, by overlapping the maps. Another relevant input for the simulation framework
201 is represented by the knowledge of load profiles in terms of distributed NG in the
202 network terminal nodes, which reliably describes the real end-user's consumption
203 trends. In general, it is possible to identify different kind of end users. Residential end
204 users use NG for heating/cooling, cooking and domestic hot water production (often
205 not all services at the same time) and the relative consumptions are generally measured
206 through traditional mechanical gas meters [29]. Commercial, technological, and larger
207 residential users (e.g., buildings with central heating systems) consume greater NG
208 volumes and they are often equipped with larger smart gas meter. Generally, they are
209 hybrid mechanical gas meters, static ultrasonic or capillary thermal mass meters,
210 which are becoming increasingly spread in urban distribution networks [30]. In fact,
211 in Italy, the Regulatory Authority for Energy Networks and the Environment
212 (ARERA) in 2008 launched a roll-out program setting the obligation to gradually
213 replace the old meters in the gas distribution networks with smart meters. To date, the
214 installation of new smart meters of a higher size than G10 has been completed, whereas
215 the use of residential G4 smart meters is not yet spread especially in medium and small
216 networks. The loads of the network can therefore be obtained from the statistical data
217 obtained from the smart meters (when installed) or, alternatively for non-remote users,
218 from forecast models used by the operators for the NG balance sheet. These forecasting
219 models are generally based on: i) at least 2-m readings per year to characterize the
220 intensity of user consumption; ii) climatic conditions (e.g., average temperature, wind
221 speed, solar radiation); and iii) a classification of end-users categories. These models
222 are based on real historical consumption data which allow to set standard consumption
223 profiles associated with different end-user categories, as a function of the intended use
224 of the gas (e.g., heating, cooling, cooking, technological or commercial use) and of the
225 expected annual consumptions. Standard load profiles can be obtained through
226 regression analysis (linear, exponential or polynomial) for which regressors are
227 represented by climatic or dichotomous parameters capable, as for example, to
228 consider differences between working days and holidays or through the use of sigmoid
229 functions whose shape fits to the typical gas consumption trend due to climatic
230 conditions [31,32]. Therefore, the estimation of daily consumptions of single users is
231 obtained per Equation (1.1).

$$NDMDC = CV \cdot SLP_d \cdot CF_d \quad (1.1)$$

In which CF_d is a corrective factor taking into account different parameters affecting gas consumptions (i.e., climatic condition, holiday), SLP_d is the standard consumption profile and CV is the customer value depending on the number of meter readings performed by the Distribution System Operator (DSO) at the single end user's premise (L_1 and L_n) according to Eq. (1.2).

$$CV = \frac{L_1 - L_n}{\sum_{d=1}^{365} SLP_d} \quad (1.2)$$

Although these methods are designed to be used for the NGN monthly balancing, their accuracy is greater when longer periods are considered. Furthermore, the forecast reliability increases significantly as a function of the available number of readings.

Generally, the available consumption forecast models allow obtaining quite reliable average daily load profiles, but not the hourly ones. To overcome this limitation, actual consumption measured by smart meter has been integrated with consumption prediction models. In this way, starting from the hourly data of the NG entering the network through the city gates and outgoing at the redelivery points (technological and residential users) measured with smart meters, it was possible to estimate the global hourly consumption at the redelivery points not measured with smart meter (average hourly value). This latter is obtained by calculating the difference between the NG distribution network (measured at the City Gates) and the sum of the hourly consumption of the largest commercial and industrial users equipped with smart meters.

Moreover, with the increasing development of smart grids it is essential to consider the interconnections of the gas network with other networks. In fact, the more NG distribution networks are interconnected with other networks (such as those of NG transmission, electricity, district heating, etc.), the more a failure in a network can propagate to the interconnected ones increasing the impact on end-users. Therefore, interdependency (i.e., interconnection and interaction) between networks should be carefully localized, qualified, and included in the modelling framework. The NG transmission networks are interconnected with the distribution networks through the regulation and measurement systems (the so-called City Gates) in which the main input parameters are represented by entering flowrates, pressure and temperature, gas quality and odorization. In addition, the NG transmission network can be interconnected with electricity networks through plants for the production of electricity from NG and/or

Power to Gas plants. Given the spread of district heating in cities, the interconnection of natural gas distribution networks with district heating networks is also highly critical. The district heating plant, generally located in a central position with respect to the users served, can be considered a technological-industrial delivery point connected to the distribution network and, due to the high consumption and the non-interruptible nature of the service, it represents a critical point to ensure adequate flow rates and pressure levels.

A key element of the proposed resilience assessment methodology is the classification of the faults that may occur in the NG distribution networks and/or in the interconnected networks and related potential impacts. Table 1.1 shows some of the main causes of failure and the related impacts, divided by type (e.g., failures from interactions with other networks, intrinsic failures of the distribution network, natural events and damages of third parties). The classification of Table 1.1 has been produced in collaboration with the gas distribution operator of the city of Salerno that shared with the author their experience and know-how. Anyway, the classification can be refined to reflect specific requirements of each single operator.

This analysis allows the network manager to partially disengage from the experiences of individual technicians and make this knowledge a collective strength of the company. For each event, the Network Operator may also report event statistics, analysis of incorrect behaviour, analysis of impacts, average recovery times, etc. These elements would allow the training of new technicians and to develop management strategies while maintaining a greater historical memory of the specificity and criticality of the network itself.

Table 1.1 – Fault classification in a distribution NG network.

Type	Fault	Impact on distribution NG pipeline system
External interconnected network failure	Technical failure: - NG transmission network failure - Electric breakdown - District heating network failure - ICT network failure	- Service interruption - Deliveries irregularities
Internal distribution network failure	Pipeline faults: - Defects and Cracks - External corrosion - Internal corrosion - Stress Corrosion Cracking Systems and components faults: - Failure of Valve and PRPs - Failure of control and discharge devices - Failures of Filters - Failure of Odorization system	- Low pressure - High pressure - Deliveries irregularities - Gas losses - Carbon monoxide generation - Fire - Explosion - Service interruption

	- Failures of ICT systems Management Fault: - Operative and maintenance procedures - Human fault	
Natural failure cause	Extreme natural events: - Hydro-geological events (landslides, earthquakes, erosion, etc.) - Extreme meteorological events (floods, hurricanes, thunderbolts, …)	- Fire - Explosion - Service interruption
Third-party damage	Accidental events: - Overloads - Accidents (fire, explosion) - Third party damages - Intentional damage - Targeted attacks and sabotages - Cyber attacks	- Fire - Explosion - Service interruption

Then, the next phase of the proposed framework is the network modelling phase. For the modelling of the network pressure, the energy conservation law is used, assuming isothermal conditions, as per Eq. (1.3):

$$\frac{dP}{dx} + \frac{\lambda}{d\rho}\frac{w|w|}{2} + \rho \cdot g \cdot \sin\alpha = 0 \tag{1.3}$$

where: i) P is the pressure (bar), λ is the pipe friction factor (dimensionless), d is the inner diameter of the pipe (m), w is the gas speed ($m \cdot s^{-1}$), g is the gravity ($m \cdot s^{-2}$), ρ is the gas density ($kg \cdot m^{-3}$), α is the angle of inclination (◦).

In the technical literature there are several fluid dynamic models for the calculation of λ in closed conduits [32]. For the case study described in the next paragraph, the author used Hagen-Poiseuille's model in the case of laminar flow and Colebrook-White's model in the case of turbulent flow, as described in Eqs. (1.4) and (1.5), respectively.

$$\lambda = \frac{64}{Re} \tag{1.4}$$

$$\frac{1}{\sqrt{\lambda}} = -2log\left(\frac{K_S}{3{,}71 \cdot d} + \frac{2{,}51}{Re}\frac{1}{\sqrt{\lambda}}\right) \tag{1.5}$$

Where Re is the Reynolds number (dimensionless) and Ks is the sand roughness (mm).

For the estimation of the pressure at the nodes and of the flow-rates through the pipeline stretches, the principles of mass and energy conservation are used, that is the

first and second Kirchhoff's law [33], as represented in Figure 1.2 and in Eqs. (1.6) and (1.7).

$$\sum_{i=1}^{N} Q_{i,k} = 0 \tag{1.6}$$

$$\sum_{i=1}^{N-1} \Delta P_{i,i-1} = 0 \tag{1.7}$$

where: $Q_{i,k}$ is the flowrate entering or leaving the K-th node, $\Delta P_{i,i-1}$ is the pressure variation in the stretch between nodes i and i+1.

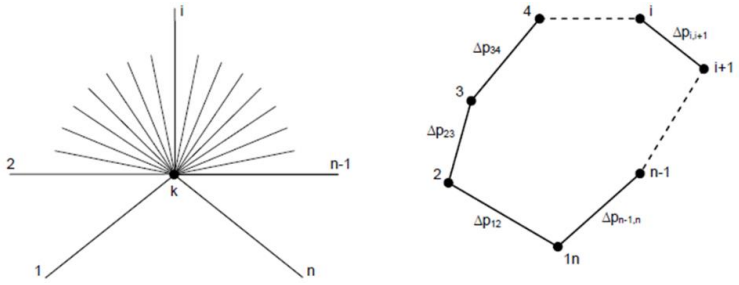

Figure 1.2 – Mass and energy conservation laws in network nodes and meshes [34].

The solution of the above-described system of equations is carried out by the PSS-Sincal commercial simulator through the Hardy Cross iterative method of flow-rates balancing. This latter is a method widely used in the resolution of optimization problems concerning looped pipeline networks [35], the application of which requires the definition of an initial flow distribution within the pipelines, capable to meet the first Kirchhoff law in each node. Kirchhoff's second law for each closed loop must be meet at the end of the iterative calculation process. To this aim, the choice of the initial flow distribution does not have a significant influence on the convergence properties of the method [36]. At each iteration, in fact, the Hardy Cross method does not directly calculate the flow through the pipe segments but calculates a correction to be added algebraically to the flow obtained in the previous iteration. Since the sign of the flow determines the direction the gas travels through the pipeline, this algebraic sum operation requires the application of complex rules that represent the major flaw of this method. In fact, while accurate results even on meshed networks are expected, due to the complexity of the rules necessary for defining the signs of the corrections to be applied to the flows at each iteration, this method may require a not negligible number of iterations in the case of very large networks. There are methods in the literature

which, by directly calculating the flows at each iteration, show the advantage of reducing the computational complexity of the problem [37]. In this work, once the gas demand at each node has been set, which also determines the quantity introduced into the network through the city gates, flows and pressures in the entire network have been calculated through the system of equations just described. Thus, the uniqueness of the obtained solution is guaranteed by the simultaneous application of the conservation equation of mass and energy (i.e., Kirchhoff's laws), in fact, although in theory there can be an indefinite number of flow distributions satisfying the conservation of mass, there is a unique solution which simultaneously satisfies the conservation of energy in each grid network [38].

The analysis performed is related to steady regime before and after the simulated fault. Furthermore, although this method is strictly applicable to not compressible fluids, in the investigated case study of natural gas distribution networks, pressure drop in pipes is minor and thus the Hardy Cross method can be used without significant errors [38]. Therefore, by applying the principle of energy and mass conservation in the nodes and branches of the network, flow rates and pressures are obtained at the relevant points of the network under standard operating conditions. On the other hand, in the presence of network failures, variations in supply pressure, extensive or localized inefficiencies are observed which affect the distribution service quality and put the safety of users of the distribution service and citizens at risk. When a network failure occurs, pressure drop in some nodes become likely. Consequently, if the demand is kept constant, the nodes whose pressure is below a threshold limit (for example 15 mbar) can be considered out of service because, due to the modified network structure, it is not possible to safely supply the required flow at the specific nodes. In this condition, the effectiveness of the distribution service is not guaranteed, and the quality of the service will deviate from the reference level. Thus, adequate recovery strategies must be promptly defined and adopted by the Network Operator.

In order to model the operation of the network under fault conditions summarized in Table 1.1, corresponding simulation scenarios are developed (see Figure 1.3), by means of a simulation tool for modelling the physical behaviour of the network.

Two approaches are currently available for simulating a gas distribution network: i) pressure-driven approach and ii) demand-driven approach (which is the most widely used). In this latter case, the model input is represented by the load profiles in each node, while the simulated pressures in the nodes and the flowrates in single branches represent the output. To allow the results of the numerical modelling to be used effectively, it is necessary to post-process the output data according to the simulation

approach used. In the case of a demand driven approach, the simulation returns the values of the nodal pressures ensuring that imposed hourly demand of gas does not vary. On the other hand, in the case of pressure driven approach, the simulation returns the flowrates at the nodes, calculated as a function of the network pressure, starting from the input hourly demand.

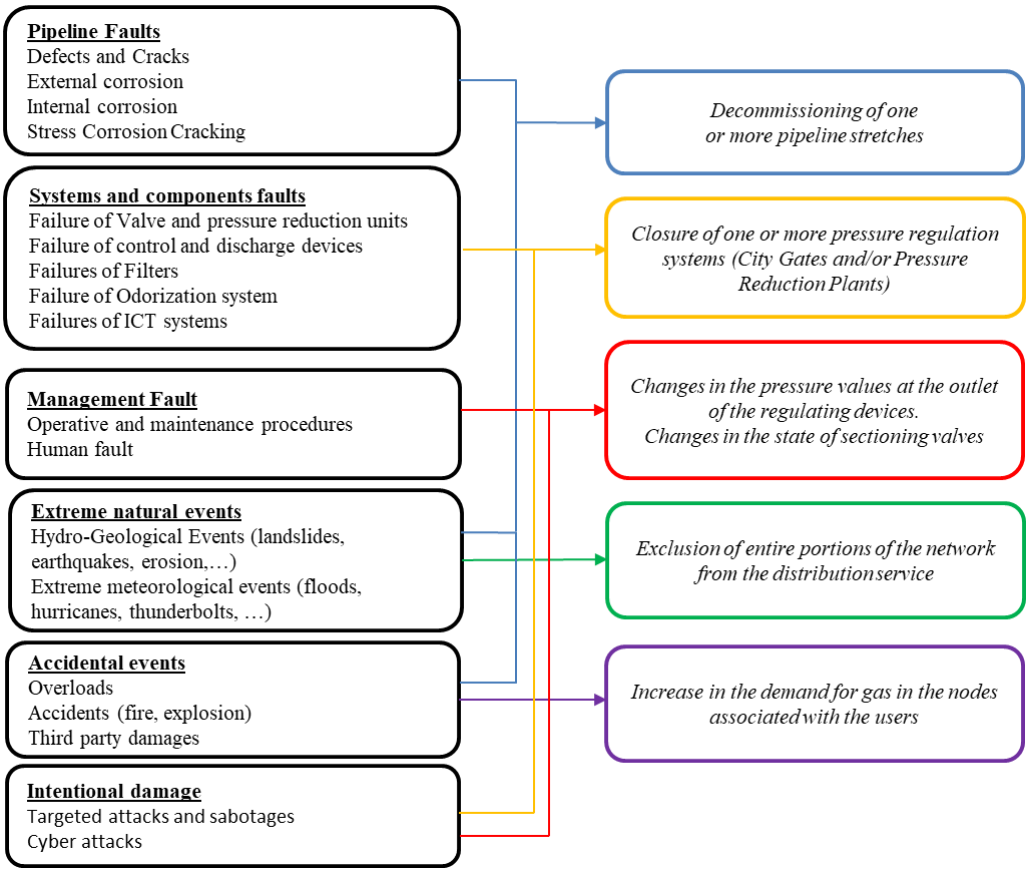

Figure 1.3 – Simulation scheme for different NG network faults.

The abovementioned approaches allow assessing the network efficiency by varying physical parameters such as pressures and flowrates at specific points, and then calculating the corresponding quality level of the service. By changing the status of PRPs or of the pipelines in the model, it is therefore possible to simulate the operating mode under different faults, critical overload conditions or irregularity of the service. The proposed methodology does not allow simulating fires or explosions caused by gas leaks from the network, for example due to damage by third parties or natural events (e.g., earthquakes, landslides). In this case, the historical data related to fires and explosions recorded in the natural gas transmission and distribution networks [39–42] can be generally used, together with the safety concerns for users and citizens, as

well as that of network integrity. Starting from such knowledge, it is possible to associate the corresponding occurrence frequencies to the types of accidents and to assess the associated individual, social and economic risk [43,44].

The output of the resilience assessment strategy proposed here includes: a) assessment of the resilience of the network with respect to the typical standard operational conditions at different assets; b) identification of nodes and critical stretches both for the quality of the service and for the safety of users and citizens. Consequently, appropriate recovery operational strategies can be defined together with prompt intervention plans, possibly also by SCADA systems for remote control and command. The aforementioned strategies must also rely on: i) the identification of structural adjustment interventions in the network to reduce the risk of breakdowns and improve the resilience of the network itself (e.g., increase in the redundancy of the components, meshing of the network, control segmentation), ii) scheduling of predictive maintenance operations that require the interruption of network segments or the temporary closure of pressure regulation devices.

1.3.2 Application of the resilience analysis simulation tool to a real natural gas distribution network

The analysed case study is represented by an urban distribution network in Southern Italy consisting of approximately 200 km of pipelines and supplying approximately 50,000 inhabitants in an area of about 57 km^2. The network is connected to the national transmission network through two city gates where the gas is measured, odorized and expanded up to about 5 bar, characteristic of the medium pressure branch of the network (about 42% in length). A further reduction is subsequently performed from the medium to the low-pressure network (which represents the remaining 58% in network length) in 31 PRPs. The distribution network presents 17,096 redelivery points (of which 48 industrial users) connected to 9372 nodes (of which 8195 in low pressure).

Redelivery points include 76 users equipped with smart meters allowing a daily metered (DM) analysis of consumptions. Indeed, these users are commonly defined as daily metered since the daily consumption obtained by summing the hourly measurements recorded by the meter is available for them. Furthermore, hourly consumption data are also available, and these latter are useful for defining the demand diagram which is one of the inputs of the simulations. Even though DM users are a small percentage of the total redelivery points, they represent approximately 50% of

the consumed volume, since they are mainly technological users (i.e., small and medium industries and public offices also including few apartment buildings equipped with centralized heating system). In detail, 48 DM users are small and medium industrial users and the remaining 28 are public offices and apartment buildings equipped with centralized heating system (domestic use). An overview of the analysed urban network is given in Figure 1.4 and Table 1.2. In particular, Figure 1.5 shows a plan representation of the urban area supplied by the network.

For this study, three sets of data have been used: i) the geometrical characteristics of the network (i.e., diameters and length of single branches, reciprocal positions of the components); ii) total natural gas entering the network in a year on an hour basis; iii) DM readings (from smart gas meters) in a year on a daily basis; iv) DM readings (from smart gas meters) on hourly basis. The investigated distribution network was entirely transposed in the GIS environment, digitizing, and defining the information of all the physical elements of the system. Such data was imported into the PSS-SINCAL simulation software.

Table 1.2 – Battipaglia's NG distribution network data.

NG distribution network data	
Low pressure network length, [km]	110
Medium pressure network length, [km]	80
Number of PRPs	31
Number of City Gates	2
Total number of Redelivery Points	17096
Number of residential customers	17048
Number of industrial users (Daily metered)	48
Number of supplied citizens	50464
Number of public offices and apartment buildings (Daily metered)	28

In order to define the required input loads for the numerical simulation, consisting of the hourly gas demand for 24 consecutive hours, the author built the hourly load diagram for each DM user equipped with Smart Gas Meter. To this aim, twenty-four continuous hours were simulated, obtaining the hourly pressure trend.

Figure 1.4 – The investigated NG distribution network of Battipaglia.

Furthermore, aimed at assessing the effect of a fault in the network in terms of disrupted citizens, author associated to single redelivery points the corresponding average number of supplied citizens. This has been obtained by disaggregating the available data from the 15th ISTAT population census at sub municipal level. Figure 1.5 shows the distribution of citizens in four sub urban areas in which the modelled network is divided. Through the open-source software QGIS, these data have been integrated with the node position. It can be also pointed out that ISTAT and single municipalities identify homogeneous portions of territory in terms of demographic and social characteristics. Therefore, assuming that the population is uniformly distributed in these areas and the location of the citizens does not change over time during the day, the approximate number of citizens can be attributed to each node. Furthermore, this was aimed at enhancing the accuracy of the model, since the DSO provided information only about the number of redelivery points.

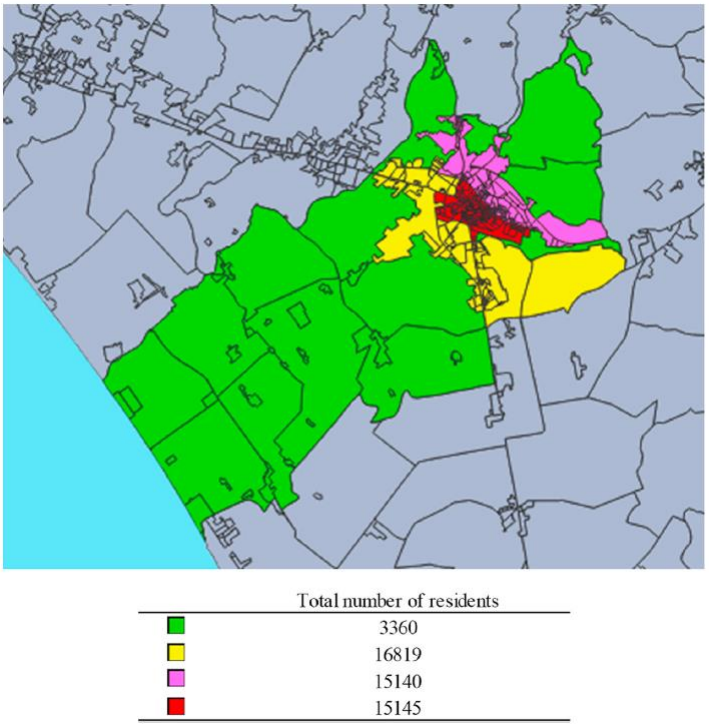

Figure 1.5 – Distribution of citizens.

1.3.3 Results and discussion

This section presents and discusses the results of the proposed network simulation framework. In particular, the analysis considers the load profiles related to the winter period that is crucial in terms of gas demand and simulates 24 h. The different simulation scenarios are obtained by considering 21 significant PRPs, identified according to their position in the network (see Figure 1.6), which in turn are set out of service for the whole simulation. The choice of the 21 meaningful PRPs was made by excluding the reduction groups dedicated to single users or to small groups of users located in peripheral areas of the network at medium pressure. These latter, in fact, represent trivial simulation scenarios since, the out of service of a PRP feeding a small number of isolated users, regardless of the surrounding conditions (i.e., hourly gas demand), always leads to the disruption of only this number of users. PRPs feeding isolated areas of the network have been considered as trivial cases since the number of disrupted customers is known a priori.

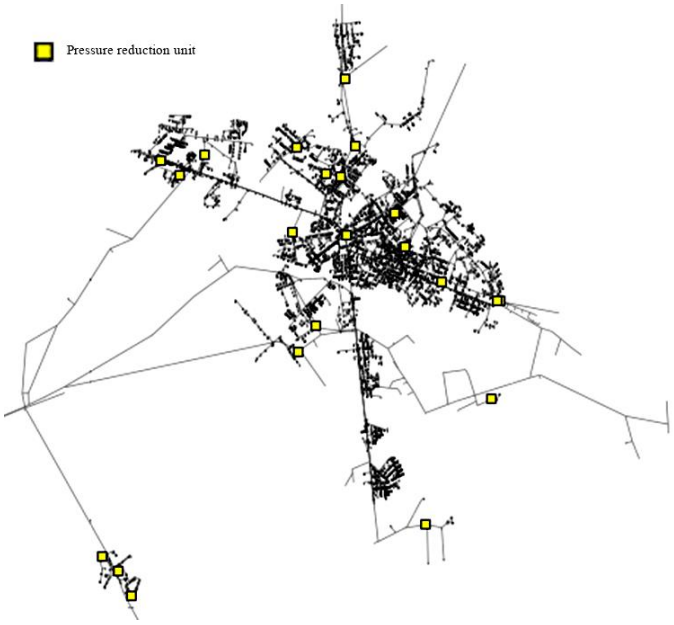

a)

b)

Figure 1.6 – a) Pressure reduction units location in the network; b) Detail of natural gas distribution network in the city centre.

Figure 1.7 shows the trend of average, minimum and maximum pressure at redelivery points as the gas demand changes under standard operating conditions. It is clear that as the volumes consumed in the network increase, the average (minimum) pressure is normally between 1.0248 (1.0245) bar and 1.0228 (1.0220) bar. Furthermore, both the average pressure and the minimum tend to decrease in correspondence with the maximum absorption hours (evening operating hours) when space heating consumptions become more relevant and can lead to greater criticalities.

Figure 1.8 shows the average pressure of all nodes of the network during the 24 h when a single PRP is out of order. The graph shows that in the different scenarios, the average pressure ranges from 1.0228 to 1.0250 bar. In almost all scenarios, the dispersion is smaller during the first hours of the day (with limited hourly gas demand), whereas it increases as consumption increase. In general, the average hourly pressure lowers in all the analysed scenarios. In particular, the heaviest operating conditions have been recorded for the scenario in which PRP 9468 is faulty. This can be ascribed to a localized pressure drop, downstream of the PRP under failure.

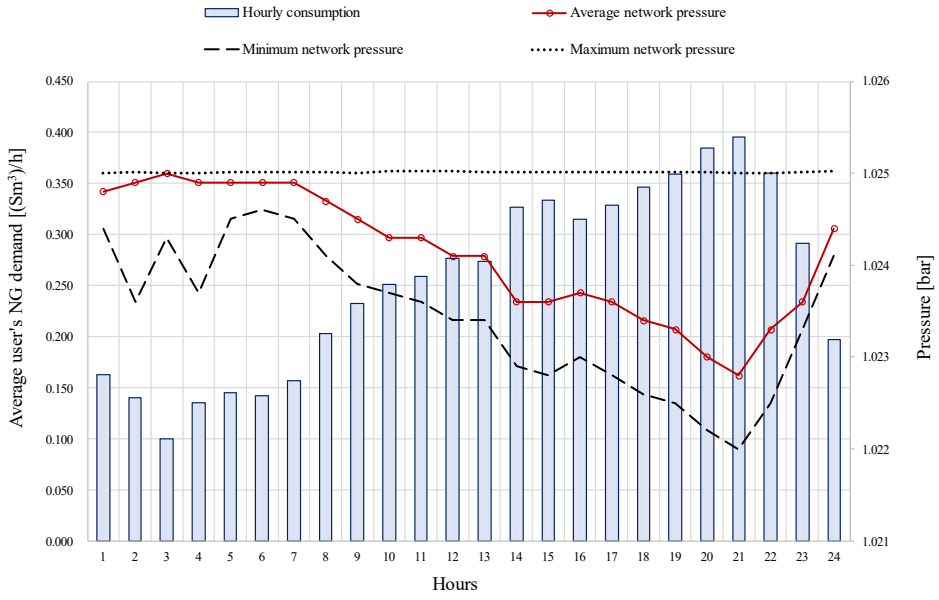

Figure 1.7 – Hourly trend of pressure and flowrate at standard conditions.

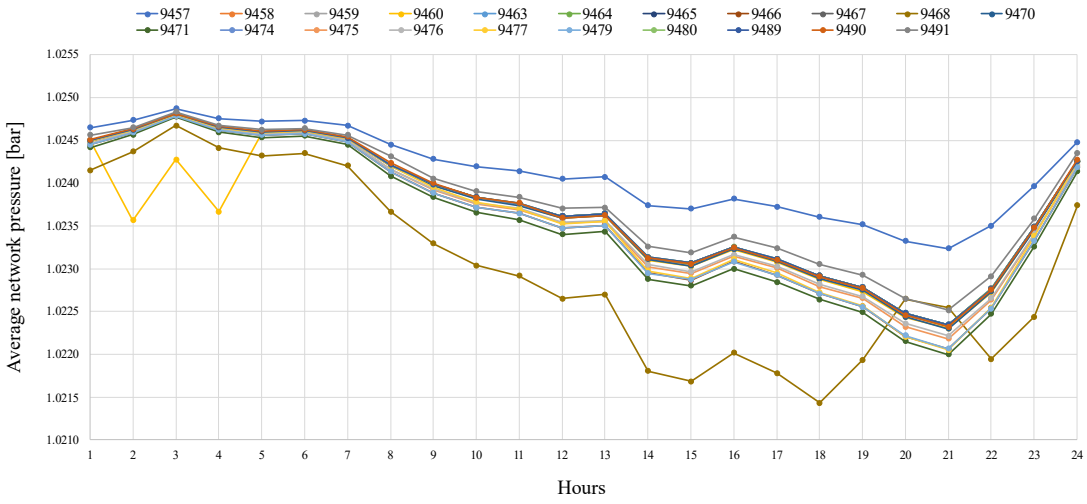

Figure 1.8 – Average pressure trend in the 21 investigated scenarios.

Whenever the pressure is not sufficient to grant the gas demand above a minimum threshold, the redelivery points connected to the aforementioned nodes can be considered out of service. As for example, Figure 1.9 shows the number of disrupted nodes (i.e., presenting pressure level lower than the threshold respectively set equal to 15, 10 and 5 mbar) for the more critical failure scenario (id. 9468).

The most interesting results are those obtained with the threshold value of 15 mbar, that is the value typically adopted by the DSO to guarantee the downstream gas demand. In this case, it was observed that the number of disrupted nodes varies from 130 (i.e., 1.6% of the network nodes) at 8 a.m. up to 1300 nodes (i.e., 16% of nodes of the network) at 9 p.m. when the peak of the gas demand occurs. Therefore, due to the dependence of the pressure on the volumes withdrawn from the network, the hours with higher gas demand are also the most critical for the level of service disruption observed under failure. Therefore, prior and timely knowledge of the temporal evolution of the failure in the network allows DSOs to guarantee the minimum level of distribution service even during the emergency phase (that immediately follows the failures of PRPs). DSOs may also schedule maintenance interventions involving temporary out of service of a device by choosing a time slot that guarantees the lowest disservice, thus limiting service interruptions.

The results obtained with the threshold of 15 mbar are summarized in Figure 1.10. In particular, the graph allows to identify the most critical scenarios (e.g., 9468) and, consequently, to obtain useful information to plan structural network interventions to increase its resilience. The dispersion of the number of nodes out of service in the different simulated scenarios is due both to the position of PRPs and to the simulated flow rates. Indeed, the most meshed sections of the network are less affected by the failure (see scenario 9457). For a more thorough analysis of the effects of network failure, the author also estimated the number of citizens not supplied under failure conditions. In Figure 1.10 the hourly trend of disrupted citizens under scenario 9648 is reported. It can be pointed out that, when the demand increases (i.e., between 8 a.m. and 9 a.m. see Figure 1.10), the number of citizens not supplied is greater than 5000 (about 10% of the total citizens). In the absence of restoration interventions, this figure increases to a maximum of 10750 disrupted citizens (i.e., 21% of the total) between 8 p.m. and 9 p.m. and only after 11 p.m. the percentage of disrupted citizens will be less than 2%.

The simulation results show how the DSO must adopt prompt countermeasures to recover the failure. If the DSO fails to adopt proper recovery procedures and the number of disrupted citizens becomes not acceptable, it will be necessary to limit the

disservice by selectively reducing the gas demand of users. Indeed, the pressure of the network strongly depends on the gas demand (i.e., delivered volumes). To this end, different options for reducing the gas demand have been investigated by the author: i) 10% (scenario # 1); ii) 15% (scenario # 2), iii) 20% (scenario # 3); iv) 25% (scenario # 4); v) 30% (scenario # 5); vi) 35% (scenario # 6); vii) 40% (scenario # 7).

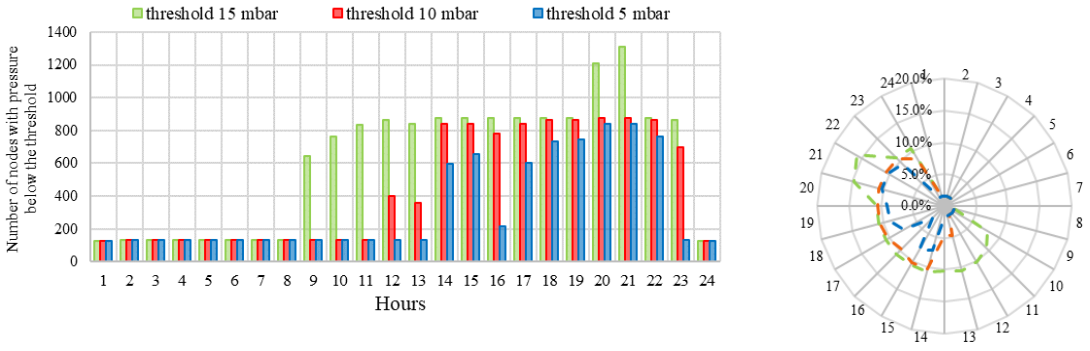

a) b)

Figure 1.9 – Scenario id. 9468: a) Number of disrupted nodes; b) Percentage of disrupted nodes in respect of total low-pressure nodes.

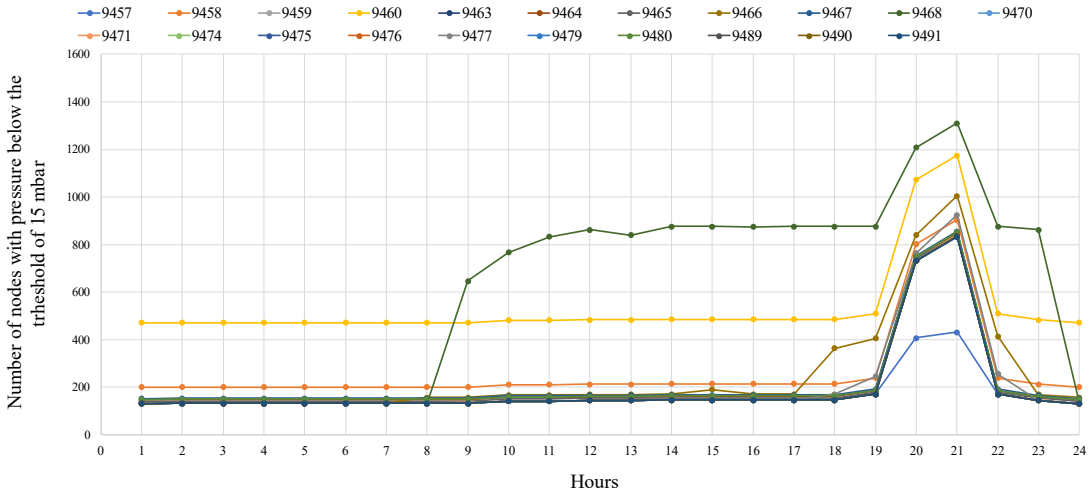

Figure 1.10 – Number of disrupted nodes under different failure scenarios.

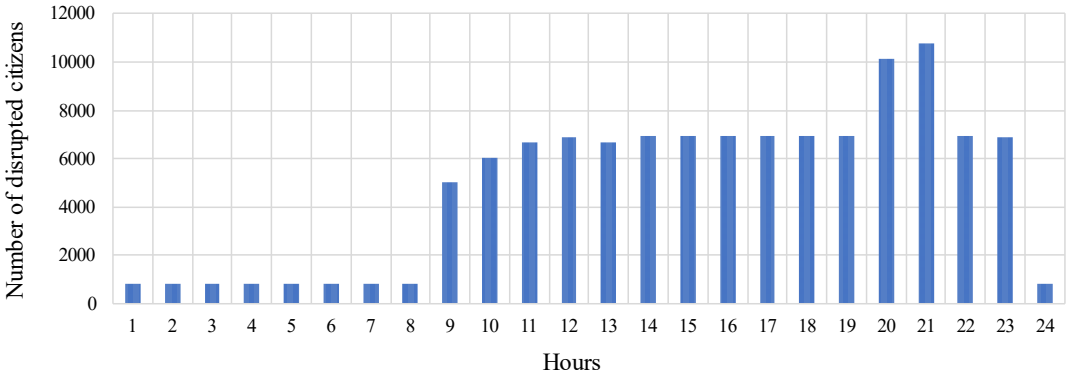

Figure 1.11 – Hourly trend of disrupted citizens under scenario 9648.

Figure 1.11 shows the results in terms of disrupted nodes, for each hour, in the different scenarios of simulated gas demand reduction. As for example, reducing the gas demand of 40%, the disservice in the critical hours (i.e., in the evening) is very limited. In particular, a 10% reduction in demand allows the disservice to be restored by 10 a.m. In the investigated case study, a homogeneous consumption reduction has been applied to all users in the network, which is a common emergency practice adopted by DSOs in presence of faults. The fact that there are no changes in the level of disservice following the imposed consumption reduction (i.e., hour 13 reduced from 10 to 15% or hour 18 reduced from 20 to 25%) can be attributed to the presence, in the neighbourhood, of a particularly energy-intensive user that initially suffers little from the effects of a widespread reduction. In this case, an appropriate emergency management plan would allow to reduce consumption on few specific users. On the other hand, the decrease of consumption can be programmed taking into account the user typology, intervening selectively and guaranteeing the service to the users that require greater protection (e.g., hospitals, medical clinics, hospices). DSO could therefore identify users whose closure would lead to lower inconvenience and plan the recovery of the fault or define alternative solutions to meet the peak demand. For this purpose, the greater diffusion of smart meters (which in Italy are mandatorily equipped with a remotely controlled closure valve) will make it possible to identify the most energy-consuming interruptible users to contain the instantaneous gas demand thus limiting the level of disservice to other users and citizens.

CHAPTER 2. ANALYSIS OF POWER TO GAS TECHNOLOGY

2.1 Power to Gas concept

Power to Gas (PtG) is one of the most promising storage technologies to support RESs integration in the energy system [45]. Exploiting the NG transmission and distribution networks, as well as the storage features of the existing NG infrastructure, the synthetic gas (i.e., hydrogen or substitute natural gas) produced from surplus renewable energy can be injected into the NG pipeline system, allowing to store large amounts of energy for long-term periods, thus offering balancing and regulation services to the electricity grid.

PtG concept involves the conversion of renewable electricity into gaseous hydrogen through electrolysis process (Power to Hydrogen – PtH_2), or into substitute natural gas (Power to Substitute Natural Gas – PtSNG) through CO_2 methanation process. The hydrogen produced can be used locally in industrial processes, transported by a grid for mobility applications, converted into methane or again into power by feeding fuel cell systems, or can be stored. Hydrogen can be also injected directly into NG pipeline systems, nevertheless certain limitations peculiar to the physical and chemical properties of H_2 prevent it from being injected in the existing NG infrastructure in larger proportions. Material durability, leakage and safety are some of the concerns that hinder blending of higher percentage of H_2 in existing NG pipeline systems. Moreover, the blending of H_2 also affects the quality of NG in terms of density, heat value and Wobbe Index. Currently, H_2 can be injected into NG pipeline systems within certain percentages varying between 0.1% and 12% vol. depending on national standards [46,47]. Such limitations make the solution of PtSNG an enabling technology toward the energy transition in the short and medium term, particularly in Europe, where the NG infrastructure is extended and capillary. Besides, H_2 reacting with carbon dioxide to form synthetic methane through the Sabatier process gives an opportunity to valorise unavoidable CO_2 emissions. The gas mixture thus produced, so called substitute natural gas or synthetic natural gas, has physical and chemical

properties comparable to NG one, therefore it can be injected into NG transportation and distribution networks without limitations. Moreover, SNG has several advantages over H_2 which deal with volumetric energy content and safety concerns [48,49].

The PtG technology allows to decarbonize the energy production and end-use sectors, to store energy over long periods, to transport and distribute it even over long distances, increasing the resilience and security of the energy system. Indeed, PtG facilitates the penetration of non-programmable RESs allowing the storage of electricity in 100% renewable energy carriers in place of conventional fossil fuel and thus, supporting the decarbonization especially of those sectors difficult to electrify such as part of industry and transport. Another benefit of PtG is the valorisation of the existing NG infrastructure, avoiding electricity grid implementations, through the electricity and gas networks integration.

Nevertheless, technical, economic and regulatory barriers hinder the spread of this technology. PtG technological challenges include electrolyser development in dynamic regimes, heat valorisation for catalytic methanation, integration of the different technologies in an optimized PtG system. The more expensive green hydrogen and SNG costs with respects to fossil gases represent a definite drawback, to be overcame by government incentives, particularly in the assessment and technological development step.

In the literature, several studies have been devoted to the economic analysis of the PtG technology. Most studies agree that the biggest cost factor contributing to capital expenditure is the electrolyser. The investment for the electrolysis unit changes in the range of approximately 800 – 3000 €/kW_{el}, depending on the electrolysis technology adopted [50]. Less information on the capital costs of the methanation unit is available in literature. In [51], it has been reported that the investment costs of a 5MW plant and a 110 MW are equal to 400 €/kW_{SNG} and 130 €/kW_{SNG}, respectively. Lehner et al. [52] identified a range of 300 - 500 €/kW_{SNG}, comparing three different studies. Gassner et al. [53] investigated a 14.8 MW CO methanation, operating at 15 bar, finding that the investment costs for the methanation section are 175 €/kW, which is in agreement with data from [51]. In [54], it has been estimated that the current costs of methanation unit is about 1500 €/kW_{SNG}, but it is expected to decrease up to 1500 €/kW_{SNG} by 2030. In addition to capital costs of electrolysis and methanation units, it is also necessary to take into account the investment cost of H_2 storage that according to Götz et al. [50], it is the second most significant contributor to the investment of a PtG plant. In [55], the authors evaluated the investment costs (i.e., costs of the main plant sections and additional costs) for a 100 MW_{el} PtG plant equal to around 223 m€, 107 m€, and

54 m€ in 2020, 2030, and 2050, respectively. As regards the operational expenditures, they are especially influenced the electricity price and potential CO_2 costs as well as a possible heat and oxygen usage. The electricity costs vary depending on the field of application and likewise, the electricity market is subject to constant change. The costs for CO_2 capture vary widely, from about 5 to 350 €/t depending on the CO_2 source and technology. In general, it can be assumed that the CO_2 required for methanation is approximately 50 €/t. Selling oxygen can reduce the SNG production costs. This is particularly advantageous in the case of oxygen is needed at the site of the PtG plant (e.g., in wastewater treatment plants). The oxygen price is about 50 €/t for large industrial use. Higher costs are incurred for small amounts in bottles (e.g., medical oxygen) of around 5 €/kg on average. For the oxygen produced by an electrolyser, it can assume a price of 50 €/t. The waste heat from electrolysis and methanation processes can also be sold, reducing the operating costs and at same time increasing the PtSNG plant efficiency. However, the integration of waste heat is highly dependent on the existing framework conditions at the plant site and the technology used. Generally, it can suppose that the waste heat can be sold at a price of about 55 €/MWh [55]. Finally, according to the data reported in [50], the SNG production costs vary in the range of 60 – 4 eurocents/$kWh_{SNG,}$ that is not economically sustainable yet, if compared with NG production costs (i.e., 2 – 3 eurocents/kWh).

In the following paragraphs, the current state of the art of core technologies in the PtG process (i.e., electrolysis, methanation) is presented. Additionally, in order to investigate the technical feasibility of the PtG concept to store intermittent RESs, two different case studies have been analysed and discussed. In the former, a PtSNG plant coupled with a RES facility has been designed and investigated by evaluating nominal and annual efficiencies for different sizes of the electrolysis unit. In the latter, a novel thermal management strategy for a PtSNG plant and how it impacts on the annual plant performances have been studied.

2.2 State of the art technologies

2.2.1 Electrolysis process

Water electrolysis consists of circulating a direct current through water to separate its molecules into hydrogen and oxygen. The current flows between two electrodes separated and immersed in an electrolyte to raise the ionic conductivity. The electrolysis process requires the implementation of a diaphragm or separator to avoid

651 the recombination of H_2 and O_2 generated at the electrodes. The electrodes, the
652 diaphragm, and the electrolyte are the elements that configure the electrolytic cell.
653 The global electrolysis reaction taking place is:

$$H_2O \rightarrow H_{2(g)} + \frac{1}{2}O_{2(g)} \qquad \Delta H°=+286\ kJ/mol \qquad (2.1)$$

654 In the electrolysis process, the electrons are taken or released by the ions at the
655 electrodes surface, generating a multiphasic gas-liquid-solid system. The reduction
656 half reaction takes place at the cathode. The electrons flow to this electrode from the
657 outside circuit and polarize it negatively. The oxidation half-reaction occurs at the
658 other electrode, called anode. The electrons leave the anode to the outside circuit,
659 polarizing it positively. Hydrogen is hence generated at the cathode and oxygen at the
660 anode.
661 Currently, three electrolytic processes can be considered for the PtG process chain:
662 i) alkaline electrolysis (AEL), ii) proton exchange membrane electrolysis (PEMEL),
663 and iii) the solid oxide electrolysis (SOEL). The following sub- section describes the
664 three electrolysis technologies considered.

665 2.2.1.1 Alkaline electrolysis

666 The alkaline electrolysis cell consists of two electrodes separated by a microporous
667 membrane. This assembly is immersed in an aqueous alkaline electrolyte, generally
668 composed of 20 – 40% wt. of potassium hydroxide (KOH) or, sometimes, of sodium
669 hydroxide (NaOH) or sodium chloride (NaCl), to maximize its ionic conductivity.
670 The operating principle of an AEL cell is illustrated in Figure 2.1. Hydrogen gas
671 evolves from the cathode, where water is reduced according to (2.2) yielding
672 hydroxide anions that circulate across the diaphragm to the anode within the electric
673 field established by an external power source. The hydroxide anions recombine on the
674 anode surface according to (2.3) to produce oxygen.

Cathode: $$2H_2O + 2e^- \rightarrow H_2 + 2OH^- \qquad (2.2)$$

Anode: $$2OH^- \rightarrow \frac{1}{2}O_2 + 2e^- \qquad (2.3)$$

675 A diaphragm separates the reaction zones from each other and prevents mixing of
676 the produced gases. Hence, the diaphragm is permeable to water ions but impermeable
677 to gases. In conventional electrolysers asbestos is used as diaphragm material.
678 Adjacent to both sides of the diaphragm electrodes are placed. The anode is usually

made of nickel or nickel coated steel, while the cathode is made of steel activated by a coating with different catalysts [56].

Typical operating temperature range is 40 – 90 °C with relatively low current densities of 0.2 and 0.4 A/cm^2 [57]. The operating pressure range is generally between 1 bar and 30 bar [46,58]. Interestingly, the maximum pressure is sufficiently high to avoid one of the compression stages when hydrogen is to be stored as compressed gas. Higher pressures do not offset because the investment costs increase significantly as well as the risks of formation of hazardous gas mixtures [58]. The energy demand of an alkaline electrolyzer is dependent on the characteristics of the electrodes and operational conditions. Atmospheric electrolysers have a specific energy demand of about 4.1 – 4.5 kWh/Nm^3 H_2 and pressurized electrolysers have a demand of about 4.5 – 5 kWh/Nm^3 H_2 [56]. The atmospheric electrolysers have an efficiency up to 85% (HHV) and the high-pressure ones have up to 78% (HHV). The purity levels of hydrogen and oxygen can reach 99.5%, without auxiliary purification equipment [57,59]. On the other hand, the water supplied to the electrolyser has to be adequately pure to protect the electrodes and operate safely.

AEL is the most mature technology and broadly employed for large-scale industrial application since decades [46,57]. AEL systems are reliable and safe, and exhibit lifetimes that can reach up to 15 years [58]. The investment costs are relatively low due to the avoidance of noble metals and mature stack components. However, low current density and operating pressure negatively impact system size and hydrogen production costs [60]. In the last years, the efficiency of the electrolysers has been improved with the aim of reducing operating costs associated with the electricity consumption. The operating current densities have been increased with the aim of decreasing the cell surface area to reduce the investment costs. These costs are almost proportional to the electrolyser's cell surface area [56].

Current issues associated with AEL technology when applied in PtG applications regard their limited minimal part-load capability. According to manufactures, the production rate is in practice limited to 20% – 100% of the nominal range, in order to prevent operating at conditions that could potentially lead to the formation of flammable gas mixtures [46,61]. However, recently progresses have been reported. New AEL designs would allow variable operation ranging from 5% to 100% of the nominal capacity [45,62]. Additionally, dynamic operation is limited negatively affecting system efficiency and gas purity, especially when AEL electrolysers are supplied by intermittent and fluctuating power sources. In fact, the response time is

typically seconds or minutes. They can take 30 – 60 min to restart the system following a shutdown [45,46].

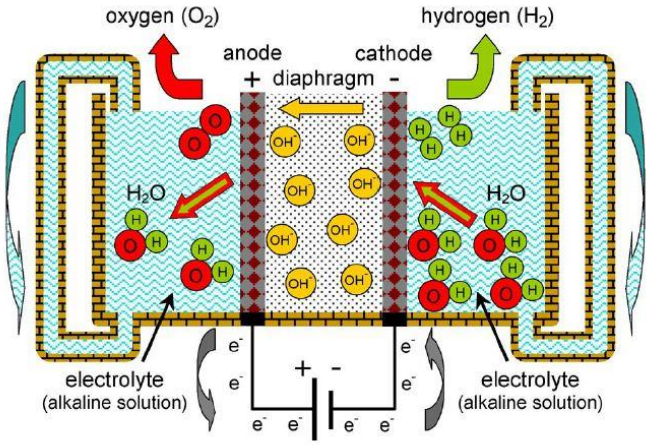

Figure 2.1 – Scheme of the operating principle of an alkaline electrolysis cell [58].

2.2.1.2 Proton exchange membrane electrolysis

In PEM electrolysers, the electrolyte is a gas-tight thin polymeric membrane with a cross-linked structure and strongly acid character due to the presence of functional groups of the sulfonic acid (-SO_3H) type. These groups are responsible for the proton (H^+) conducting ability of the materials through an ion exchange mechanism. The most commonly used membrane for water electrolysis is Nafion [58].

The modules of the proton exchange membrane water electrolysers almost invariably adopt a bipolar configuration in which the electrical connection between cells is carried out by means of bipolar plates that also play an important role in the evacuation of the generated gases. The anode, cathode, and membrane set constitute the so-called membrane electrode assembly (MEA). The electrodes typically consist of noble metals such as platinum or iridium [58].

The operating principle of a PEMEL cell is shown in Figure 2.2. At the anode, water is oxidized according to (2.4) to produce oxygen, electrons, and protons that circulate across the membrane to the cathode where they are reduced according to (2.5) closing the circuit and producing hydrogen.

Anode: $$H_2O \rightarrow \frac{1}{2}O_2 + 2H^+ + 2e^- \quad (2.4)$$

Cathode: $$2H^+ + 2e^- \rightarrow H_2 \quad (2.5)$$

734 PEMEL electrolysers operate at a temperature of around 80 °C and a pressure of up
735 to 15 bar [56]. Some models reach pressures up to 85 bar. This is due to the compact
736 character of the electrolysis modules as well as the structural properties of the MEAs,
737 which can endure big pressure differences between the electrode compartments. These
738 devices can operate at current densities that are quite higher than their alkaline
739 counterparts, achieving values even above 1.6 A/cm^2 [58]. Specific energy demand is
740 typically in the range of 6 – 8 kWh/Nm^3 H_2, but it can also be below 6 kWh/Nm^3 H_2
741 in large-scale systems with a production rate higher than 10 Nm^3 H_2/hr. Their
742 efficiencies are in the range of 67 – 82% [56]. The hydrogen purity, higher than in
743 alkaline electrolysers, is typically above 99.99 vol.%, without the need for any further
744 purification equipment [45]. Moreover, the very low gaseous permeability of the
745 polymeric membranes lowers the risk of formation of flammable mixtures; hence to
746 operate at very low current densities is permissible [58].
747 Compared to AEL, PEMEL technology is a relatively new technology. The first
748 commercial PEMEL electrolyser was available for purchase in 1978 [45,46]. Because
749 of the use of noble materials (i.e., platinum group metals) as catalysts, the cost has
750 been estimated to be at least double (i.e., > 2000 €/kW) that of the AEL technology.
751 Moreover, the lifetime is shorter than that of the AEL systems and falls within the 5 –
752 20 year range [45]. However, PEMEL is considered to be the best choice for PtG plant
753 due to its ability to operate under variable power feeding regimes [62]. This is owing
754 to the fact that the proton transport across the polymeric membrane responds quickly
755 to power fluctuations. On the contrary, the ionic transport in liquid electrolytes in AEL
756 electrolysers shows a greater inertia [56]. Indeed, PEMEL electrolysers can be
757 completely ramped up and down in just a few seconds, additionally, they can work in
758 the 0 – 100% range and a cold start can be completed in just minutes.

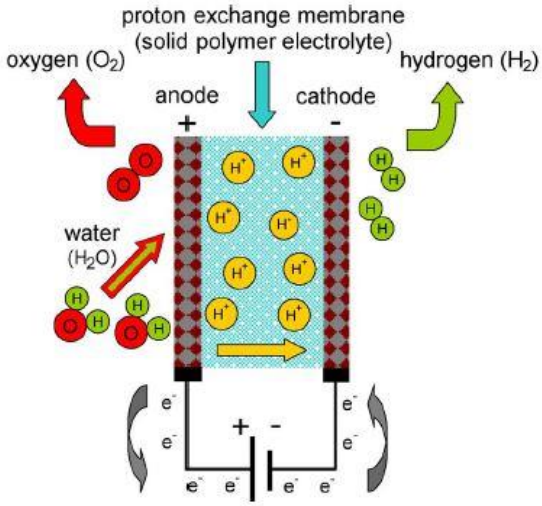

Figure 2.2 – Scheme of the operating principle of a proton exchange membrane electrolysis cell [58].

2.2.1.3 Solid oxide electrolysis

Solid oxide electrolysers constitute an advanced concept of water, or rather steam, electrolysis at high temperature (i.e., up to 1000 °C), which results in higher efficiencies compared to AEL or PEMEL electrolysers [56].

The operating principle of a SOEL cell is illustrated in Figure 2.3. Both steam and recycled hydrogen are fed to the cathode, where water is reduced to produce hydrogen according to (2.6). The oxide anions generated in the cathode pass through the solid electrolyte to the anode, where they recombine according to (2.7) forming oxygen and closing the circuit with the released electrons.

Cathode: $$H_2O + 2e^- \rightarrow H_2 + O^{2-} \quad (2.6)$$

Anode: $$O^{2-} \rightarrow \frac{1}{2}O_2 + 2e^- \quad (2.7)$$

These reactions evolve with the electrodes in contact with a gas or vapor phase, which is in clear contrast with the processes taking place on the electrodes of the AEL or PEMEL electrolysers and makes the issue of maximizing the interfacial area in contact between the electrodes and the gaseous chemical species challenging. This is the reason of the porous character of the SOEL's electrodes. The solid oxide electrolyte is typically made up of a gas-tight thin film of yttria (Y_2O_3) stabilized zirconia (ZrO_2) (YSZ) [46]. This material exhibits good ionic conductivity at the prevailing high operating temperatures through a mechanism that involves the oxygen vacancies

present in the mixed oxide lattice. The cathode is a cermet usually consisting of nickel and YSZ. The anode is commonly a composite of YSZ and perovskites such as lanthanum manganites ($LaMnO_3$), ferrites ($LaFeO_3$) or cobaltites ($LaCoO_3$) partially substituted with strontium in order to promote structural and electronic defects that increase the electrocatalytic activity [58].

Steam electrolysis emerged aiming to reduce the energy demand and so, the operating costs of conventional liquid water electrolysis. Indeed, the electrical energy demand significantly decreases as the temperature increases. This means that the proportion of the required energy that can be supplied in the form of heat increases with electrolysis temperature. Specifically, up to 40% of the energy required to produce hydrogen via steam electrolysis can be supplied as heat at 1000 °C and the electricity demand can be reduced by up to 25% [56]. Therefore, those electrolysers are expected to reach higher efficiency than that of AEL and PEMEL electrolysers [46,62][46,50].

Currently, SOEL electrolysers are at a research and development stage. They are not yet widely commercialised, but systems have been developed and demonstrated on laboratory scale and individual companies are aiming to bring this technology to market [57]. However, the main current obstacle for the commercialization of SOEL technology are the fast material degradation and the limited long-term stability of the electrolysis cells due to high temperature operation. Furthermore, the high temperature level means that the product stream from the electrolyser is a mixture of hydrogen and steam, requiring additional processing; thereby further increasing the capital costs [46,56]. Thus, current research is focussed on stabilising existing component materials, developing new materials, and lowering the operation temperature to 500 – 700 °C to enable the commercialisation of this technology [57].

As regard the SOEL technology application into the PtG process chain, it could lead to a higher overall efficiency of the process if combined with exothermal reactions (e.g., CO_2 methanation). Nevertheless, SOEL systems are not stable against fluctuating and intermittent power sources [46,56].

The construction characteristics and operating parameters of the above-described electrolysis technologies are listed in Table 2.1.

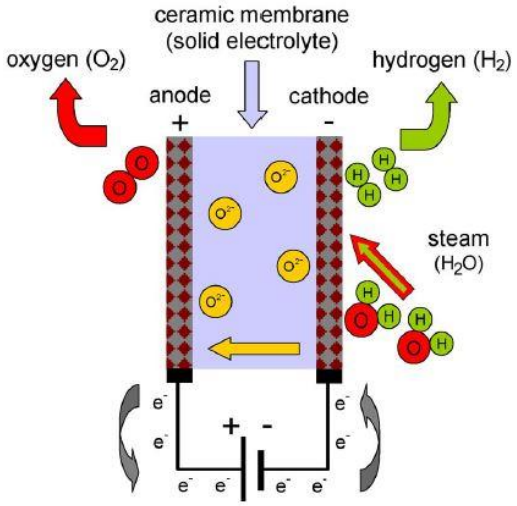

809

810 *Figure 2.3 – Scheme of the operating principle of a solid oxide electrolysis cell [52].*

811 *Table 2.1 – Construction characteristics and operating parameters of electrolysis technologies*
812 *[57,59].*

	AEL	PEMEL	SOEL
State of development	Commercial	Commercial	Laboratory
Electrolyte	20 – 40 %wt. KOH	Nafion	YSZ
Cathode	Ni, Ni-Mo alloys	Pt, Pt-Pd	Ni/YSZ
Anode	Ni, Ni-Co alloys	RuO_2, IrO_2	LSM/YSZ
Charge carrier	OH^-	H_3O^+/H^+	O^{2-}
Cell temperature [°C]	40 – 90	20 – 100	750 – 1000
Cell pressure [bar]	<30	<80	<25
Cell voltage [V]	1.8 – 2.4	1.8 – 2.2	0.91 – 1.3
Current density [A/cm^2]	0.2 – 0.4	0.6 – 3.0	0.3 – 2.0
Production rate [m^3/h_{H2}]	up to 760	up to 450	-
Stack energy consumption [$kWh_{el}/m^3 H_2$]	4.2 – 5.9	4.2 – 5.5	>3.2
System energy consumption [$kWh_{el}/m^3 H_2$]	4.5 – 6.6	4.2 – 6.6	>3.7
Gas purity [%]	>99.5	99.99	99.9
Lower load [%]	10 – 40	0 – 10	>30
System Response	Seconds	Milliseconds	-
Cold-start time [min]	<60	<20	>60
Stack Lifetime [h]	60000–90000	20000–60000	<10000
Replacement stack [year]	8 – 12	-	-
Capital Cost [€/kW_{el}]	1000 – 1200	1860 – 2320	>2000

2.2.2 Methanation process

For the production of SNG, further processing of the H_2 and CO_2 via the Sabatier reaction is required. The chemism of CO_2 methanation reaction is known for more than one century and chemical methanation processes have been state of the art for several decades. They have been and still are applied to produce SNG from synthesis gas derived from coal or biomass. Gas purification in chemical or petrochemical industries is another widely used application of the methanation process. Although methanation is technological mature in these fields of application, specific differences and challenges arise when used as process step within the PtG concept. This paragraph gives an overview of the state of the art of methanation processes and the specifics for the application of this technology as part of PtG.

2.2.2.1 Fundamentals

Methanation of CO_2 is an exothermic process through which H_2 and CO_2 react to form CH_4 and H_2O. The reaction is described by described by the following stoichiometric equation:

$$CO_2 + 4H_2 \rightarrow CH_4 + 2H_2O \qquad \Delta H = -165 \text{ kJ/mol} \qquad (2.8)$$

The most widely accepted mechanism of the CO_2 methanation reaction is the combination of the endothermic Reversed Water Gas Shift (RWGS) reaction as an intermediate reaction (2.9) and the exothermic methanation of the CO (2.10) produced from the RWGS reaction:

$$CO_2 + H_2 \rightarrow CO + H_2O \qquad \Delta H = 41 \text{ kJ/mol} \qquad (2.9)$$

$$CO + 3H_2 \rightarrow CH_4 + H_2O \qquad \Delta H = -206 \text{ kJ/mol} \qquad (2.10)$$

Low temperatures, typically between 200 °C and 550 °C depending on the used catalyst, and high pressures favour thermodynamically the conversion of CO_2 to CH_4. In a simple one-stage process and with an operating pressure of 20 bar and keeping the temperature at 450 °C, the carbon dioxide conversion reaches approximately 93% and an increase of the operating pressure does not significantly improve the methane yield [63].

The product gas leaving the reactor contains steam, CO and unconverted educts beside the product CH_4. The product composition can be influenced by the methanation process concept, the reaction parameters and also by the reactor types

used. Additionally, the applied catalyst influences kinetics, conversion rate and selectivity of the process.

Catalytic active substances for the hydrogenation of CO_2 or CO are group VIII metals, i.e., the Fe-group, the Co-group and the Ni-group. Mainly due to the reasonable cost and satisfactory performance in terms of conversion rates and selectivity, Ni based catalysts are widely utilized for methanation processes today. Usually, silica-based carriers are used, but also zeolites or metal carriers are known. Basically, catalysts are sensitive to poisons, which may result in catalyst deactivation. Typical catalyst poisons are heavy metals, but also sulphur compounds or oxygen [64].

2.2.2.2 Process concepts

Due to the highly exothermic nature of CO_2 methanation reaction, a significant issue in the methanation process is the temperature control as a means to prevent thermodynamic limitation and catalyst sintering. To solve such issue, several steady state reactor concepts have been developed [46].

In Figure 2.4, the classification of reactors employed in the methanation process is depicted. Specifically, all developed chemical methanation reactors involve the use of a solid catalyst and for this reason, they belong to the category of heterogenous catalytic reactors. The latter can be classified into 2-phase reactors and 3-phase ones, which differ from the 2-phase systems in the application of a liquid energy carrier to remove the heat released by the methanation reaction. The 2-phase reactors, in turn, can be categorized into fixed bed reactors (i.e., adiabatic fixed-bed reactors, isothermal fixed-bed reactors) and fluidized bed reactors.

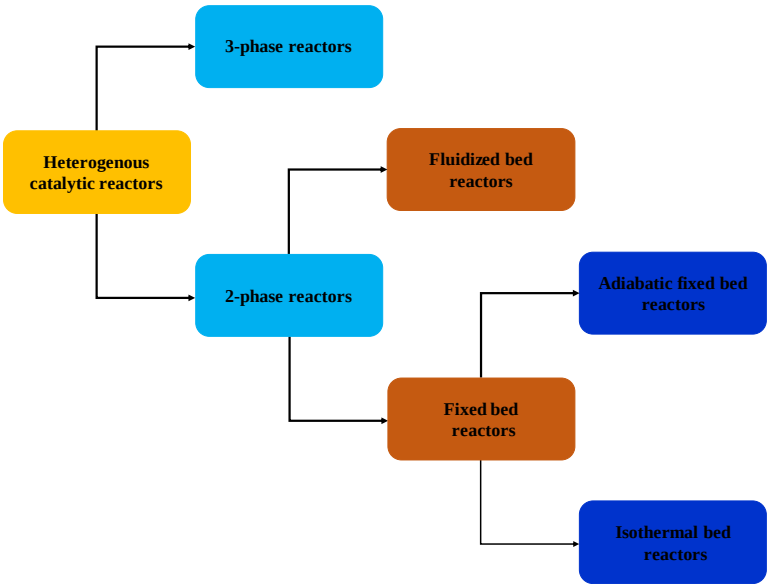

Figure 2.4 – Classification of methanation reactors.

2.2.2.2.1 Adiabatic fixed-bed reactors

Fixed-bed reactors are state of the art for methanation process in the PtG plant [62,65]. Fixed-bed methanation utilizes catalysts, in pellet form, some millimetres in size which are dumped randomly into the reactor forming a preferably homogeneous, static catalyst bed [64]. Thus, the contacting of the catalyst particles by the gas tends to be quite uniform, and long contact times are possible [62]. The fixed-bed reactors can be designed adiabatic or isothermal, as abovementioned.

Adiabatic fixed-bed reactors typically operate between 250 °C and 700 °C [46], and in a pressure range of between 20 and 100 bar [45]. Mass transfer limitations between the gases and the solid catalyst are a disadvantage of the fixed bed types, whilst the mechanical stress to the catalyst is comparably low, and hence one of the main benefits [64]. For adiabatic fixed bed-reactors, the usual approach relies on a series of adiabatic reactors with intermediate cooling steps for a better temperature control inside the reactors and consequently, obtaining high CO_2 conversion [62,63]. The temperature control is sometimes realised through the partial product gas recirculation. Hence, the processes using adiabatic fixed-bed reactors can be distinguished between processes with the partial product gas recycle and processes without the partial product gas recycle.

2.2.2.2.1.1 Process with recycle

TREMP process

The TREMP (Topsøe's Recycle Energy efficient Methanation Process) process was developed by Danish company Haldor Topsøe in 1970, through the experimental activity carried out within the context of EVA I and ADAM I projects [66].

The TREMP technology addresses the essential question of minimum recycle cost and heat recovery most efficiently by recovering the heat as high pressure superheated steam (10 MPa, 540 °C) [67]. The process consisted of three or more adiabatic fixed bed methanation reactors connected in series with intermediate gas cooling and partial product gas recycle (see Figure 2.5). Namely, the exit gas from the first reactor after being cooled enters the subsequent methanation reactors operating at decreasing temperature levels. The number of methanation reactors depend on the operating condition, such as pressure, as well as the SNG product specification. The temperature range of the reactors is from 250 to 700°C and the pressure up to 30 bar [66].

Beside the technology, Haldor Topsøe also provided the catalyst (MCR-2X, MCR4) for the high temperature methanation. The catalyst is based on a ceramic support with a stabilized micropore system that effectively prevents sintering of nickel crystals. The resulting high nickel surface area results in the desired high methanation activity even at relatively low temperature [67].

The experimental parameters obtained from the tests on high-temperature methanation carried out in the bench-scale unit ADAM I are summarized in Table 2.2.

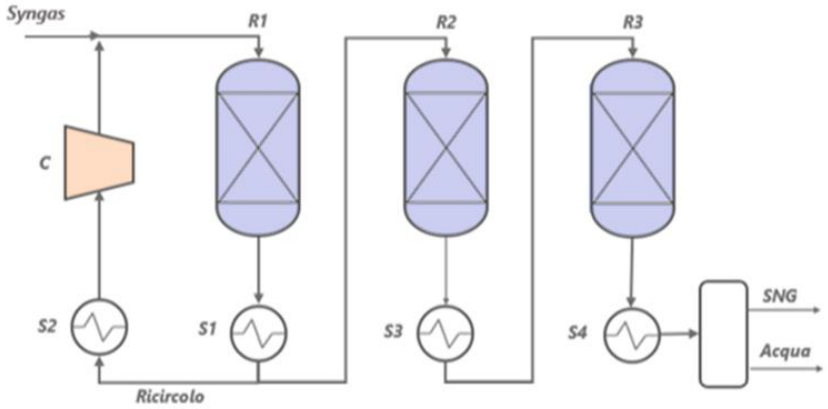

Figure 2.5 – TREMP process scheme [66].

Table 2.2 – Operation parameters and gas composition of TREMP process [66].

	Feed	R1 Inlet	R1 Outlet	R2 Outlet	R3 Outlet	SNG
Temperature [°C]	-	300	604	451	303	23
Pressure [bar]	27.3	27.2	27.1	27.05	27	27
Flow rate [Nm^3/h]	535	1416	1255	348	334	191
Gas composition [vol. %]						
H_2	65.45	36.88	20.96	8.10	1.77	3.11
CO	9.84	4.28	1.17	0.00	0.00	0.00
CO_2	8.96	6.13	4.46	2.07	0.95	1.67
CH_4	11.30	28.12	37.44	44.36	47.28	82.95
H_2O	-	19.19	29.82	38.84	43.06	0.10
N_2	4.40	5.41	6.15	6.64	6.93	12.16

Lurgi process

The Lurgi process, developed in the 1930 in Germany, was the first commercially viable technology applicable for the production of SNG in pipeline quality. The first

pilot plants rely on this technology were erected in the early 1970s. One pilot plant was designed and erected by Lurgi and SASOL in Sasolburg (South Africa) and another pilot plant was erected by Lurgi and EL Paso Natural Gas Corporation in Schwechat (Austria). The methanation unit in these two pilot plants consisted of two adiabatic fixed bed reactors with a product gas recycle from the outlet of the first reactor (see Figure 2.6). The two plants differed in the catalyst used. In the first plant, a commercial catalyst with 20 wt.% Al_2O_3 was used, whereas, in the second one, a special methanation catalyst developed by BASF with a high nickel content (G 1-85). The experiment with the first catalyst showed a fast catalyst deactivation. The second catalyst operated for 4000 hours and reached the adiabatic equilibrium temperature of 450°C after 32% of the catalyst bed [66]. The experimental condition and gas compositions for a typical run of the pilot plant with the second catalyst are summarized in Table 2.3.

In 1984, the first and only commercial SNG from coal plant was commissioned and installed at Great Plains Synfuels in North Dakota (United States). The installed methanation plant consists of three adiabatic fixed bed reactors with a product gas recycle from the outlet of the 2nd stage to the inlet of the first reactor (see Figure 2.7). The major change within the more than thirty years of operation was an additional by-pass of the third methanation reactor. The recycle ratio is equal to 4 and operating pressure is 18 bar. Additionally, a by-pass of the first reactor gives the possibility of staged feed injection as measure for temperature control [68].

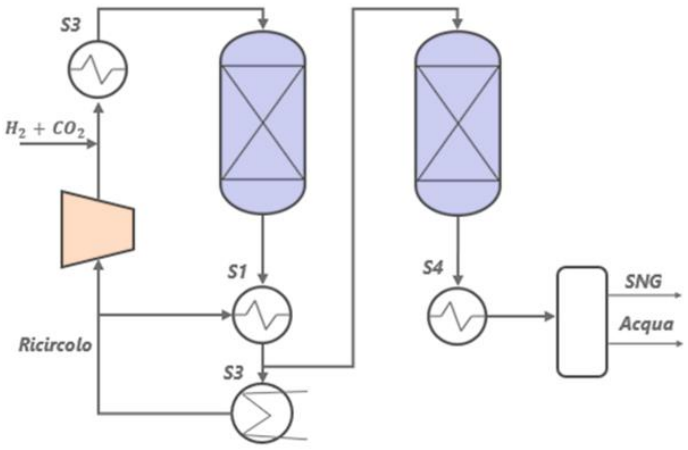

Figure 2.6 – Lurgi process scheme [66].

Table 2.3 – Operation parameters and gas composition at pilot plant of the Lurgi process [66].

	Feed	R1 Inlet	R1 Outlet	R2 Outlet	R2 Outlet

Temperature [°C]	270	300	450	260	315
Flow rate [Nm^3/h]	18.2	96.0	89.6	8.2	7.9
Dry gas composition [vol. %]					
H_2	60.1	21.3	7.7	7.7	0.7
CO	15.5	4.3	0.4	0.4	0.05
CO_2	13.0	19.3	21.5	21.5	21.3
CH_4	10.3	53.3	68.4	68.4	75.9
C_{2+}	0.2	0.1	0.05	0.05	0.05
N_2	0.9	1.7	2.0	2.0	2.0

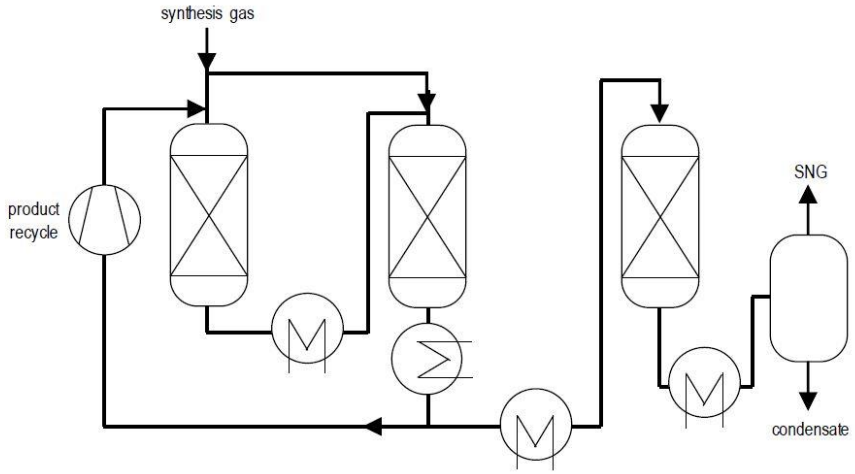

Figure 2.7 – Lurgi process as installed in Great Plains Synfuels Plant [68].

HICOM process

The HICOM (High Combined Shift Methanation) process was developed by Conoco and British Gas Corporation in Scotland in 1972 [66], and is distributed nowadays by Johnson Matthey as DAVY^{TM} technology [68]. The HICOM process differs from the aforementioned ones as it contains no separate water-gas-shift reactor. It rather integrates the shift reaction in the first methanation stage, achieving a thermal efficiency of about 70% [66]. This process aimed at low H_2/CO ratios. In order to increase the hydrogen amount, hot water was mixed in counter-current in a packed-bed with the purified syngas flow for gas heating and water saturation. CO_2 removal downstream of the methanation process lowers the temperature increase in the methanation reactors but also requires a larger reaction volume due to the increased overall gas flux. Similar to other large-scale processes, a product gas recycle and intermediate gas cooling serve for heat control in a series of three adiabatic fixed-bed reactors [68] (see Figure 2.8). A bench-scale reactor was erected for screening of

catalysts and process conditions. The pilot plant consisted of 37 mm diameter reactors in which long term tests under near-commercial conditions were studied. Several tests run of up to 2000 hours duration were carried out with catalyst pellets of 3.2 mm and 5.4 mm [66]. Typical gas compositions and operating conditions of the pilot test are summarised in Table 2.4. A semi-commercial scale plant was built at the Westfield Development Center (Scotland). The plant was operated with an inlet temperature between 230 to 320°C and outlet temperatures in the range from 460 to 640 °C at a syngas flow rate of 5300 m^3/h for a total test time of 15 000 hours [68].

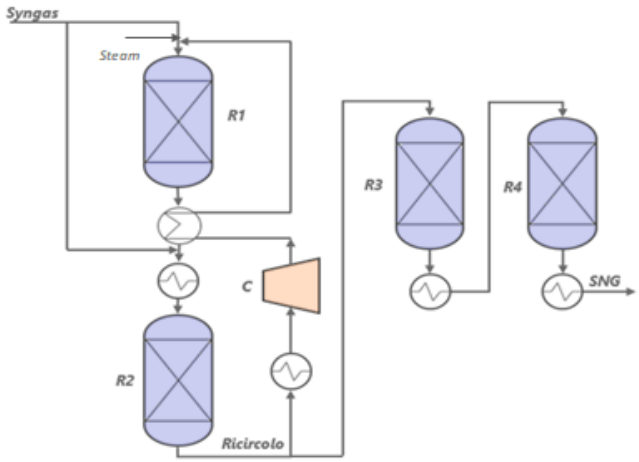

Figure 2.8 – HICOM process scheme [66].

Table 2.4 – Operation parameters and gas composition of the HICOM process [66].

	Feed gas	Product gas
Inlet Temperature [°C]	230 – 320	
Flow rate [Nm^3/h]	25 – 70	
Maximum Temperature [°C]	460 – 640	
Dry gas composition [vol. %]		
H_2	11.7	5.5
CO	12.6	1.1
CO_2	43.0	53.1
CH_4	31.7	39.3
N_2	1.0	1.1

2.2.2.2.1.2 Process without recycle

RMP process

Ralph M. Parsons Company proposed a high temperature methanation concept without gas recycle and no separate shift conversion unit (RMP process). The methanation process consists of 4 to 6 adiabatic fixed bed methanation reactors in series with intermediate gas cooling (see Figure 2.9). Similar to the HICOM process, the RMP process involves the steam addition before the first stage in combination with a staged feed gas injection in the first three reactors in order to control the temperature increase in each single adiabatic methanation reactor. Such configuration is so-called 'Steam Quenching Methane Synthesis' [68].

The system pressure was varied between 4.5 and 77 bar, the inlet temperatures of the reactors were varied between 315 and 538°C, and the H_2/CO ration was varied between 1 and 3 [66].

The following Table 2.5 shows the dry gas composition and the temperatures of an experimental run at 27 bar. 40% of the total cleaned syngas with H_2/CO ratio of one entered the first reactor together with steam with an inlet temperature of 482°C. The product gas was cooled, then mixed with 30% of the syngas, and then fed to the second reactor. The last 30% of the syngas were added in the third reactor together with the product gas from reactor two. The inlet of the fourth, fifth, and sixth reactors were temperature controlled as shown in Table 2.5. In the first reactor, CO was mainly converted to CO_2 by the water gas shift and minor the CH_4. H_2O and CO_2 are removed from the product gas leaving the sixth reactor and fed to final dry methanation stage to reduce the H_2 and CO content below 3 and 0.1 vol%, respectively. After 1977 no more information about this project are available [66].

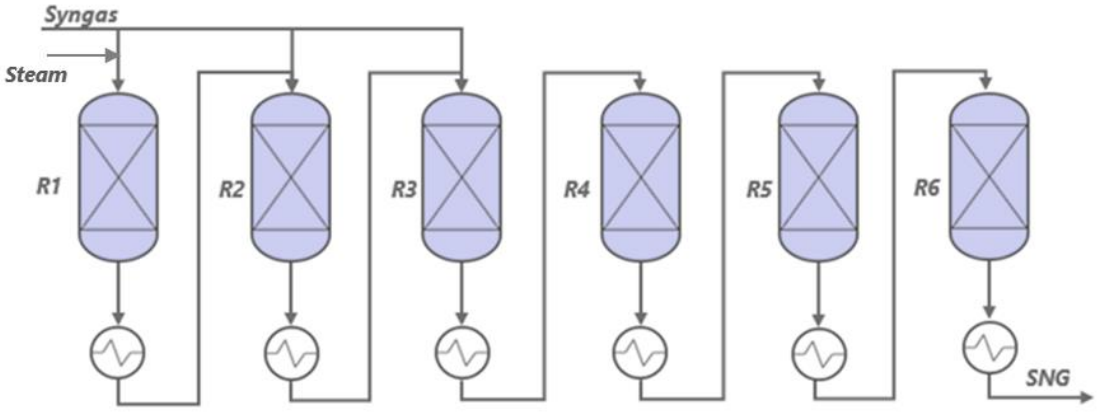

Figure 2.9 – RMP process scheme [66].

Table 2.5 – Operation parameters and gas composition of the RMP process [66].

	R1 Inlet	R1 Outlet	R2 Outlet	R3 Outlet	R4 Outlet	R5 Outlet	R6 Outlet
Inlet Temperature [°C]	-	482	538	538	538	316	260
Outlet Temperature [°C]	482	773	779	773	717	604	471
Pressure [bar]	27.3	26.7	25.6	24.6	23.6	22.6	21.5
Inlet Syngas [vol. %]	40	-	30	30	-	-	-
Steam/gas ratio	1.20	0.88	0.56	0.43	0.50	0.65	0.83
Dry gas composition [vol. %]							
H_2	49.8	53.5	48.1	43.1	36.9	22.9	9.3
CO	49.8	14.0	18.5	20.6	15.3	5.6	0.88
CO_2	0.1	25.8	24.0	23.6	29.2	39.9	46.8
CH_4	0.3	5.7	9.4	12.6	18.6	31.6	43.0

ICI process

Similar to the RMP process, the Imperial Chemical Industries ICI (Great Britain) developed a catalyst and a high temperature once-through methanation process, using a catalyst with a high nickel content (up to 60%). This process consists of three adiabatic fixed bed reactors in series with intermediate gas cooling (see Figure 2.10). The steam added to the second reactor in order to maintain the temperature below 750°C. On the basis of this scheme no large scale plant have been built [66].

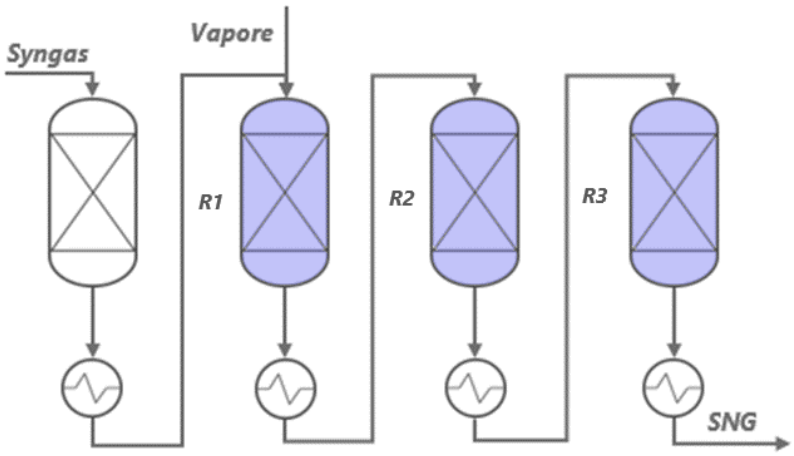

Figure 2.10 – ICI process scheme [66].

Table 2.6 – Operation parameters and gas composition of the ICI process [66].

	R1 Inlet	R1 Outlet	R2 Inlet	R2 Outlet	R3 Inlet	R3 Outlet
Temperature [°C]	398	729	325	590	300	428
Dry gas composition [vol. %]						

H_2	42.9	35.5	35.5	20.3	20.3	5.8
CO	31.1	14.5	14.5	4.3	4.3	0.3
CO_2	24.7	40.2	40.2	53.9	53.9	62.7
CH_4	0.1	8.5	8.5	19.8	19.8	29.1
N_2	1.2	1.4	1.4	1.7	1.7	2

VESTA process

The VESTA process was developed by Amec Foster Wheeler and Clariant, on the basis of the technology from ICI developed in the 1970s [69]. This process comprises a high temperature shift reactor followed by three adiabatic methanation reactors (see Figure 2.11). Temperature control is achieved through steam control in the synthesis gas. Furthermore, CO_2 removal takes place downstream of methanation and, hence, brings additional thermal ballast into the system. These measures keep the adiabatic synthesis temperature below the tolerable catalyst limit (i.e., 550°C or 650°C). A first pilot plant with 100 Nm^3/hr capacity was erected in Nanjing, China, and started-up in July 2014 [68].

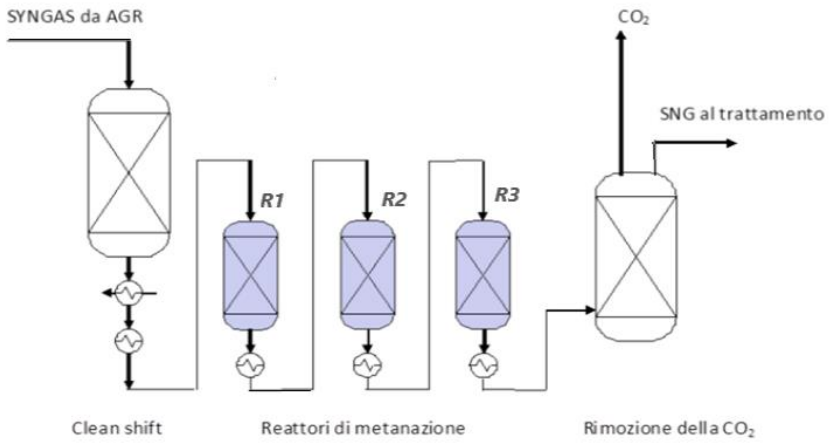

Figure 2.11 – VESTA process scheme.

2.2.2.2.2 Isothermal fixed-bed reactors

The isothermal conditions in fixed-bed methanation reactors can be accomplished: (i) by inserting cooling coils or tubes into the random bed of catalyst particles, (ii) keeping the catalyst inside tubes and the cooling medium on the shell side, or (iii) by coating the catalyst to surfaces which are cooled from the other side. By far the most common type of cooled fixed bed reactors are multi-tubular reactors, where the catalyst is filled into the tubes while the cooling medium is on the shell side [70].

In comparison to adiabatic reactors, the isothermal reactors operate in lower pressure (i.e., 1 – 20 bar) and temperature (i.e., 280 – 300 °C) ranges. Moreover, they are characterized by scalability, large heat transfer areas, good mass exchange process and relatively short transport distances within the bed to the next heat transfer. On the other hand, some of its disadvantages include the construction and maintenance complexity [70,71].

Recently, PtG raised again interest in cooled reactors. Hence, the first commercial PtG plant in Werlte, Germany, comprises a cooled DWE® tube bundle reactor manufactured by MAN engineering, which is in operation since 2013 [68].

Linde process

In the 1970s, Linde AG (Germany) developed an isothermal fixed bed reactor with indirect heat exchange. In this reactor, the cooling tube bundles are embedded in the catalyst bed, as illustrated in Figure 2.12.

The process flow diagram of the Linde process with one isothermal and one adiabatic fixed bed reactor is shown in Figure 2.13. The temperature control of the isothermal reactor is carried out by the production of steam from the heat of the exothermic methanation reaction. A part of the steam should be added to the gaseous mixture outgoing from the isothermal reactor to minimize the risk of carbon deposition on the catalytic bed of the adiabatic reactor. The product gases of both reactors are finally mixed, cooled, and reaction water is condensed [66].

The process has never been commercialized to produce SNG. Today, the Linde isothermal reactors are used in other processes of the chemical industry such as methanol synthesis, hydrogenation, ethylene oxide synthesis etc.

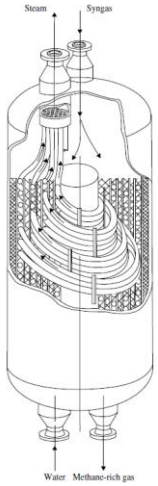

Figure 2.12 – Isothermal reactor scheme [70].

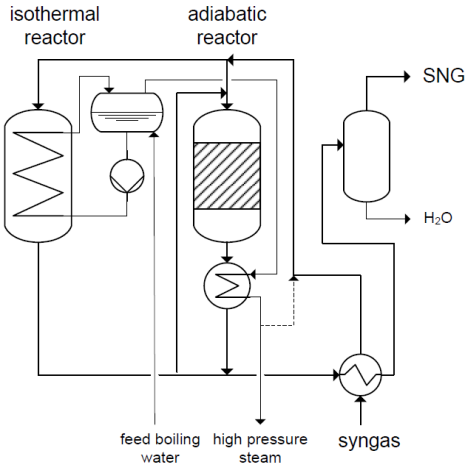

Figure 2.13 – Linde process scheme [66].

2.2.2.2.3 Fluidized-bed reactors

Fluidized-bed reactors are known to be suitable for large-scale operations of heterogeneous catalysed reaction with high exothermicity [66]. The mixing of fluidized solids leads to almost isothermal conditions in the reactor, facilitating the control of the operation [46]. The main advantages of this reactor concept are a good heat release and a high specific surface area of the catalyst combined with reduced mass transfer limitations. Consequently, reactor cascades are avoided, and so a simplified set-up is realized compared with fixed bed systems [64]. Further advantage is the possibility to easy remove, add, and recycle catalyst and or bed material continuously during the process [66]. However, due to high mechanical load resulting from fluidization, attrition processes take place in relation to the catalyst as well as the wall of the reactor. As a consequence, the catalyst is eventually deactivated. A further disadvantage can be the incomplete CO_2 conversion caused by bubbling. In addition, a fluidized-bed reactor is limited by superficial gas velocity within the reactor: it cannot be too low in order to assure minimum fluidization conditions and cannot be too high in order to avoid catalyst elutriation [46].

In 1952, the former Bureau of Mines (US Department of the Interior) developed two multiple feed fluidized-bed methanation reactors (see Figure 2.14) to produce pipeline quality synthetic natural gas from coal via gasification and methanation. Both systems were operated in a temperature and pressure range of 200 to 400 °C and up to 20.7 bar, respectively, and in recycle mode with a ratio of up to four. The H_2/CO ratio

of the feed gas varied between one and three. The results have shown a good temperature control in the multiple-feed fluidized bed and that nickel was superior to iron as a methanation catalyst. The iron catalysts were not active enough to produce SNG in pipeline quality; the conversion of H_2 and CO was less than 80%, and in addition, higher hydrocarbon C_{2+} and C_{3+} were formed. Nickel catalyst was found to be very active and suitable for methanation of syngas, but extremely vulnerable to sulphur poisoning [66].

In 1963, Bituminous Coal Research Inc. (BCR, United States) initiated the Bi-Gas project in which was developed a gas-solid fluidized-bed reactor including a second feed inlet and two in-tube heat exchanger bundles, as depicted in Figure 2.15. The published results of the experiments showed that the conversion of CO was in between 70 and 95%. The relatively low conversion means the product gas needed to be converted in a final fixed bed methanation reactor [66].

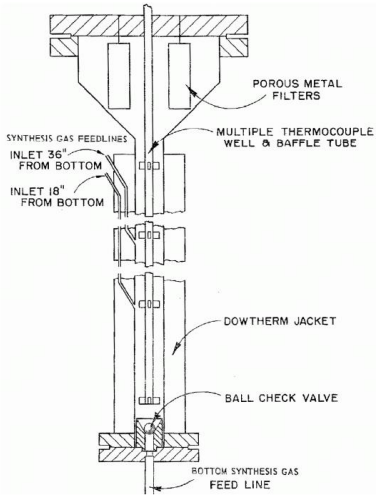

Figure 2.14 – Multiple feed fluidized-bed reactor scheme [66].

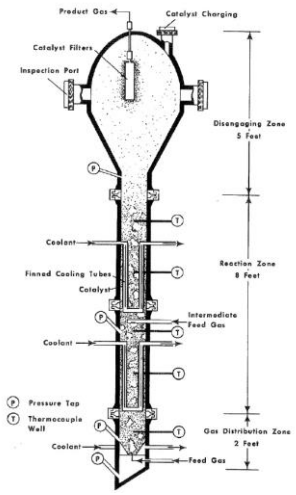

Figure 2.15 – Fluidized bed methanation reactor by Bituminous Coal Research Inc. [66].

Comflux process

The biggest fluidized bed methanation reactors so far have been erected and operated within the Comflux project in Germany, between 1975 and 1986. plant with a diameter of 0.4 m was erected by Didier Engineering GmbH (Germany) and operated for several hundred hours, from 1977 to 1981 [66]. The scheme of the so-called Comflux process and the experimental conditions are illustrated in Figure 2.16 and Table 2.7, respectively.

The Comflux process belongs to the class of isothermal reactors using heat exchangers integrated into the fluidized bed. The single stage, nearly isothermal fluidized-bed omits the need for a separate shift unit since the water gas shift reaction and CO methanation take place simultaneously. The particle movement in the fluidized bed allows for a superior heat distribution in the bed and facilitates mass transfer. The nearly isothermal conditions also favour the reaction control. Methanation of a synthesis gas with a H_2/CO ratio smaller than three requires an additional CO_2 removal downstream [68].

Later 1981, the Comflux process was demonstrated on the industrial scale (2000 $m^3_{SNG} \cdot h^{-1}$; up to 20 MW_{SNG}) in Oberhausen (Germany). The pilot plant consisted of a tube with 1.0 m diameter at a fluidized bed temperature varying from 450 °C to 550 °C. The plant was operated slightly under-stoichiometric with a low recycle-gas volume ratio from 0 to 0.3 [66,68]. In specific pilot scale experiments, it was shown that the isothermal operation allows the methanation of synthesis gas with a H_2/CO ratio of 1.5 by addition of steam, combining the water gas shift reaction and the methanation in one apparatus. In commercial plant, the omission of the shift unit and the product gas recycle compression as well as the possibility to raise all steam at the same high-pressure level should lead to significantly reduced investment and operation costs. With that project, the developers aimed at SNG cost 10% lower than from a fixed bed process. The technology development was discontinued when the price of oil dropped in the mid of the 1980 [66].

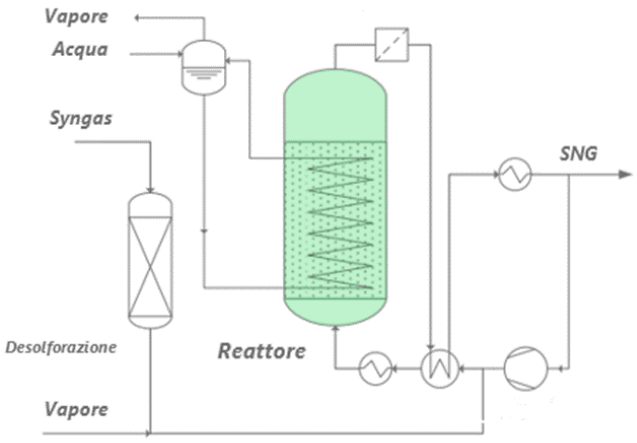

Figure 2.16 – Comflux process scheme [66].

Table 2.7 – Experimental conditions for the Thyssengas pilot plant [66].

Parameter	Value

Temperature [°C]	300 – 500
Pressure [bar]	20 – 60
H_2/CO ratio	up to 4
Recycle/Feed ratio	up to 2
Gas velocity [$m \cdot s^{-1}$]	0.05 – 0.2
Bed diameter [m]	0.4
Bed height [m]	2 – 4
Particle size [µm]	50 – 250
Catalyst mass [kg]	200

2.2.2.2.4 Three-phase reactors

In 1970, a three-phase fluidized-bed methanation reactor was developed by Chem System Inc. (United States) [64,66], as depicted in Figure 2.17. Syngas produced in a coal gasifier was introduced into the catalytic liquid phase methanation reactor along with a circulating process liquid (i.e., mineral oil) that absorbs the heat of reaction. The product gas was separated in a liquid phase separator and in a product gas separator. The process liquid was pumped through a filter to remove any catalyst fines and recirculated back to the methanation reactor. The product gas, mainly methane and carbon dioxide with some unconverted hydrogen and carbon monoxide was analysed and sent to a flare. No recycle gas was needed. Experiments with different nickel catalysts (Harshaw, Engelhard, CCI and Calsicat), process liquids and operational conditions (260-360°C, 20.7-69 bar, H_2/CO ratio 1 – 10, adding water) in three different reactors were carried out, see Table 2.8. The bench-scale unit (BSU) and process development unit (PDU) were operated for several runs of 40 to 80 hours each [66].

By introducing a liquid phase, the heat release of the exothermic reactions is promoted and thus an isothermal temperature profile in the reactor is achieved. The heat carrier fluid for cooling circulates in heat exchangers, which are placed in the liquid phase of the methanation reactor. The high heat storage capacity of the fluid is favourable with respect to load changes and the isothermal conditions make a once-through process without product recycle possible as no thermodynamic limitation exists. The fluidization and mixing of the solid-liquid mixture are accomplished by pumping the fluid or by the gas bubbles when the catalyst particles are small. Furthermore, catalyst abrasion is reduced compared to the fluidized bed. The hydraulic operation of a three-phase bubble column is quite sophisticated. Due to the introduction of the liquid phase, an additional mass transfer resistance between the

gaseous educts and the solid catalyst incurs which may negatively influence the kinetics of the total process. Specifically, the right choice of the fluid is of major importance as a low vapor pressure and high thermal stability are mandatorily since operating temperature is commonly in the range of 260 – 360°C [64,68].

Since 1972, the American company Chem Systems Inc. has been working on commercialization of the concept. In 1977, the company erected a first pilot plant of a liquid-phase methanation system with a total capacity of 36 000 Nm^3/day at a pressure of 34 – 52 bar. The plant was located at the Institute of Gas Technology (IGT) in Chicago, Illinois. The project has been terminated 1981. The approach of Chem. Systems has foreseen the circulation of the liquid phase with an external heat exchanger to temper the reaction medium. However, this approach required a solid-liquid separation step and pumps [68].

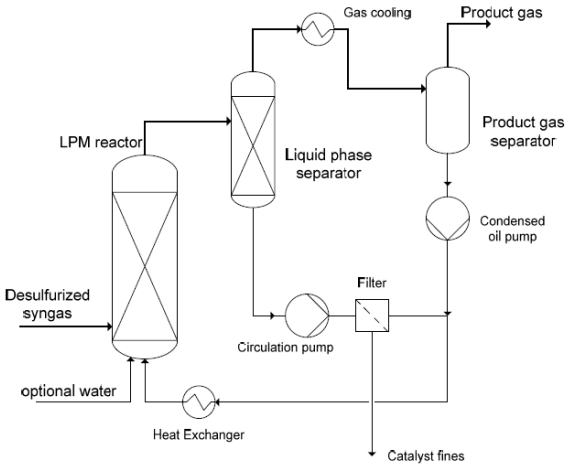

Figure 2.17 – Three-phase methanation concept [66].

Table 2.8 – Three-phase methanation reactors and operational conditions [66].

Parameter	BSU	PDU	Pilot plant
Reactor diameter [cm]	2.0	9.2	61.0
Reactor height [m]	1.2	2.1	4.5
Gas flow [$m^3_N \cdot h^{-1}$]	0.85	42.5	425 – 1534
Catalyst bed height [m]	0.3 – 0.9	0.68 – 1.8	-
Catalyst mass [kg]	-	-	390 – 1000
Pressure [bar]	20.7 – 69		34 – 52
Temperature [°C]	260 – 380		315 – 360
H_2/CO ratio	1 – 10		2.2 – 9.5
Catalyst size [mm]	0.79 – 4.76		

2.3 *Case study #2: SNG generation via Power to Gas technology: plant design and annual performance assessment*

2.3.1 Material and methods

2.3.1.1 PtSNG Plant description

Figure 2.18 shows the layout of the proposed PtSNG plant. The plant consists of four sections: (i) the hydrogen generation unit based on the proton exchange membrane (PEM) electrolysis, (ii) the CO_2 methanation unit based on the fixed-bed technology, (iii) the hydrogen storage unit based on the pressure vessels technology, and iv) the SNG upgrading unit based on the membrane technology.

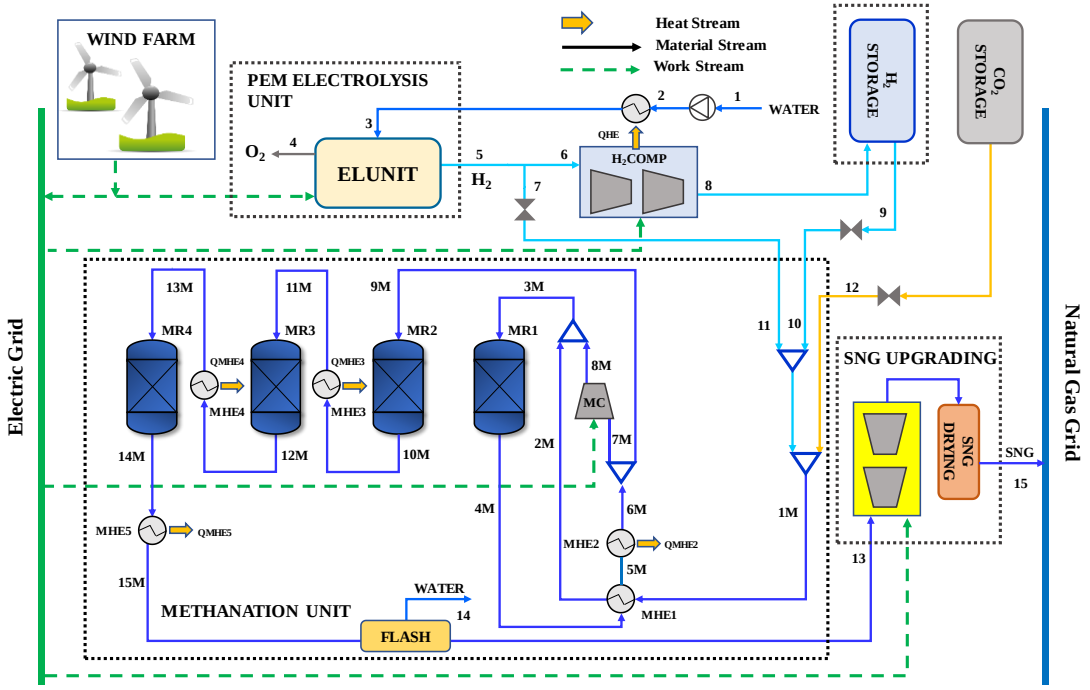

Figure 2.18 – PtSNG plant layout.

The demineralized water (1) is pumped (2) and heated (3) to the operating pressure and temperature of the PEM electrolysis unit (20 bar and 55 °C) where oxygen (4) and hydrogen (5) are generated. According to the control strategy of the storage unit, the product hydrogen (5) can be partially or totally sent to the methanation unit (7) and/or to the intercooled compressor H2COMP (6) for increasing the pressure up to the

maximum storage value (45 bar). In the methanation unit working at 20 bar and consisting of four intercooled fixed bed reactors, the carbon dioxide and the hydrogen are converted to SNG.

At the exit of the reactor MR4, the CO_2 conversion achieves the 99.2% but the methane content is only about 32.1% due to the large amount of the water produced during the methanation process. The raw SNG (14M) is, therefore, cooled down to 45 °C in the heat exchanger MHE5 and sent to the flash unit where most of the water is removed. Nevertheless, in order to comply with the water dew point requirements of the pipelines, the SNG have to be further dehydrated. The technology used for the SNG drying is based on the membrane technology (a commercial Pebax®-based membrane [72]), so that a compression step is required for bringing the feed gas to the operating pressure of the dehydration membrane. The quality of the dry SNG exiting the upgrading section satisfies the pipelines specifications and can be directly injected to the low-medium pressure NG transmission grid.

It is assumed that the CO_2 is always available for the PtSNG plant (supplied by sequestration from other power plant as a by-product or industrial processes) at storage pressure of 200 bar.

The PtSNG is operated in input-oriented mode [73]. This means that the SNG production depends on the availability of electrical energy and reactants (H_2 and CO_2).

Finally, all the high-temperature equipment is thermally insulated in order to minimize heat dissipation, and it could be maintained in hot standby conditions using electrical trace heating to compensate the estimated heat losses [74,75].

2.3.1.2 Wind power source

The power source data (a collection of one-year hourly measurement data) used in this study refer to a 12 MW (overall capacity) real wind farm installed in Central Italy close to the NG transmission network. In Figure 2.19, the power duration curve and the cumulative curve of the electric energy generated during a year of operation are reported.

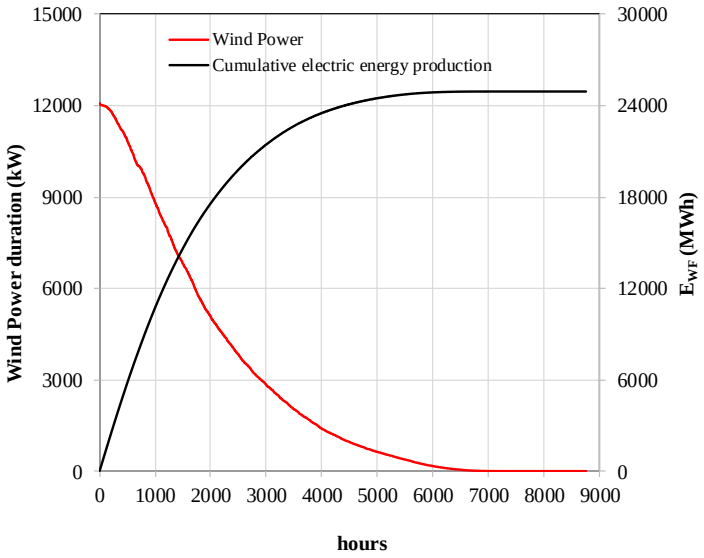

Figure 2.19 – Power duration and cumulative electric energy production.

The total electric energy generated is equal to 24,930 MWh and is mainly produced in about 6000 h.

Figure 2.20 shows the distribution of the electric energy production and the duration time for different power ranges.

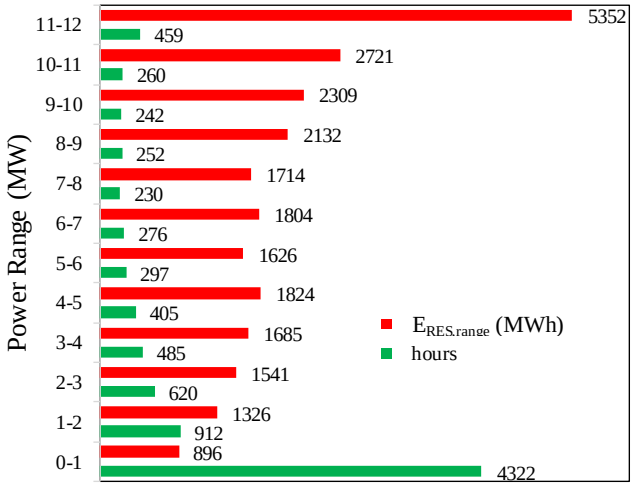

Figure 2.20 – Distribution of the electric energy production and the duration time for different power ranges.

It is worth noting that the wind farm works mainly in the 0 – 1MWpower range (4322 h) producing only the 3.4% of the electric energy generated in the year, whereas the highest production percentage (21.4%) is reached in the range 11 – 12 MW with a

duration time of 459 h. This means that, in order to optimize the PtSNG plant from an energetic and economic point of views, the size of the electrolysis unit has to be a compromise between the operating time and the installed power.

A size parameter for the PtSNG plant is the stored energy factor, defined as the annual electric energy supplied to the electrolysis unit of the PtSNG plant, $E_{PtSNG,EU}$, and the annual energy generated by the wind farm E_{Wind}:

$$f_{SE} = \frac{E_{PtSNG,EU}}{E_{Wind}} \tag{2.11}$$

In this parameter, the electric energy requirements of the other plant sections (hydrogen compressor or SNG compressor) are not accounted.

Using the wind farm energy data reported in Figure 2.20, the electric energy consumption (MWh_{AC}/year) and the stored energy factor for different sizes of the electrolysis unit have been calculated and reported in Figure 2.21 .

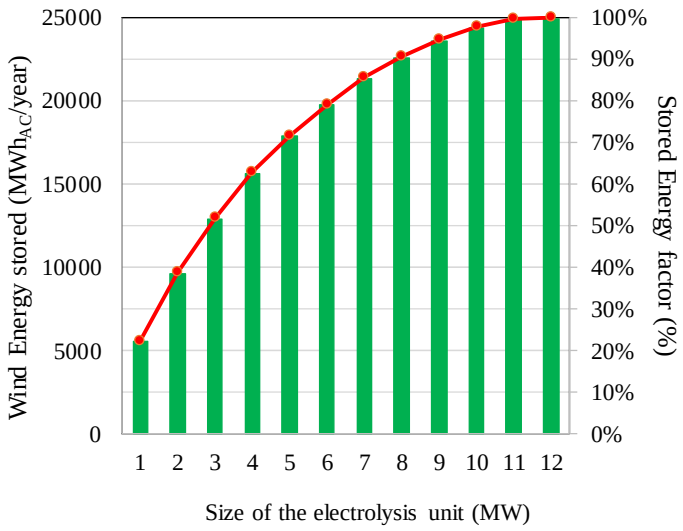

Figure 2.21 – Electric energy consumption (MWh_{AC}/year) and stored energy factor.

The stored energy factor shows an exponential trend as the capacity of the electrolysis unit increases, so that 79% of the wind energy production can already be stored using a 6 MW electrolyser.

Thus, in order to evaluate the energy storage potential and the technical feasibility of the PtSNG concept to store intermittent renewable sources, the PEM electrolysis units considered as power input sizes for the annual performance assessment of the plant are 1, 3, and 6 MW_{DC}, corresponding to a stored energy factor (in AC) of 22%,

52%, and 79%. This means that the methanation unit and the hydrogen storage unit as well as the other plant equipment will be sized accordingly and will differ one from other only by a scale factor.

2.3.1.3 Plant modelling

The energy model of the PtSNG plant has been built using the Aspen Plus software package, a commercial flowsheet simulator that allows simulating complex energy systems such as gas processing plants. Aspen Plus uses mathematical algorithms, based on thermodynamic models, physical relationships, and properties methods, to define mass and energy balances.

Figure 2.22 shows the flowsheet of the plant model. Each subsystem is simulated by means of Hierarchy blocks (ELUNIT, METUNIT, STORAGE, and SNGUP) interconnected through mass, energy, or information flows.

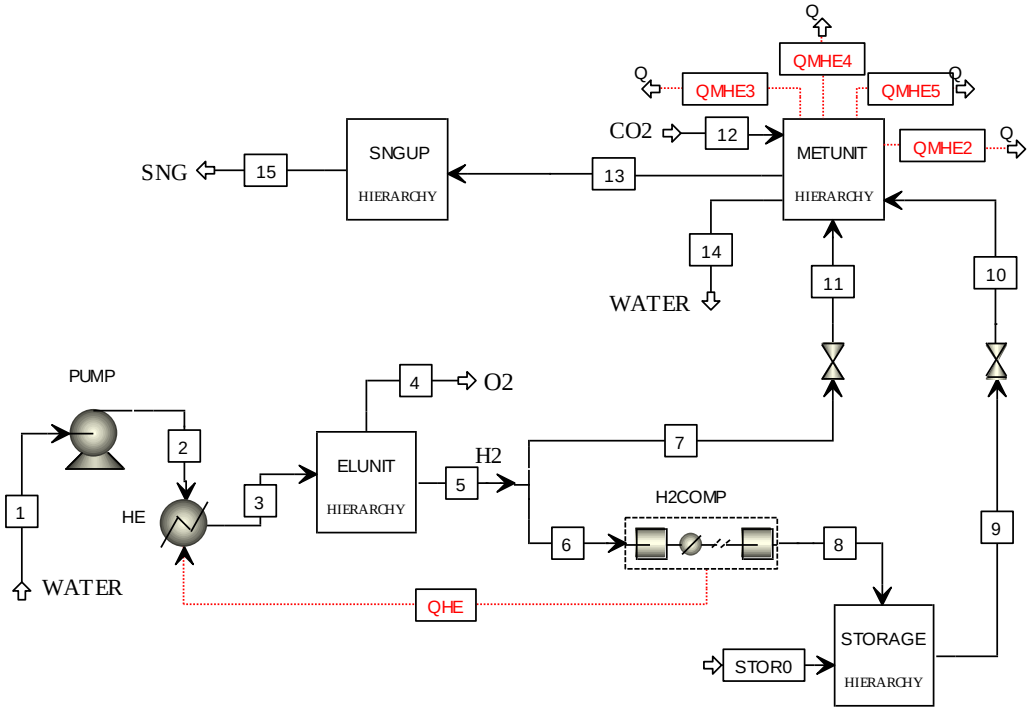

Figure 2.22 – The flowsheet of PtSNG plant integrated model.

The input mass streams are the water (1) entering the electrolysis unit (ELUNIT) and the CO_2 (12) feeding the methanation unit (METUNIT), whereas the output mass streams are the SNG leaving the SNG upgrading unit (SNGUP), the oxygen (4) produced by the ELUNIT, and the water (14) from the methanation unit. Each hierarchy block represents a specific section of the plant (i.e., the methanation unit,

METUNIT, or the electrolysis unit, ELUNIT) and is modelled in a sub-flowsheet by combining operation blocks and calculator blocks for components and processes simulation. The operation blocks are defined in the software library, therefore, once the specific block is selected, the solving equations are defined. The calculator blocks are developed by the user by implementing the model equations in Fortran language. The Peng-Robinson cubic equation of state, which can accurately describe both the liquid and vapor phase for systems containing hydrocarbons and related compounds and for high H_2 content systems in a wide range of pressure and temperature, has been used for evaluating properties and characteristics of each material stream.

2.3.1.3.1 Electrolysis Unit (ELUNIT Hierarchy)

The PEM electrolysis unit is built with a modular architecture. The module is formed by stacks each of which consists of cells. Therefore, the element of the system is the single cell. In Figure 2.23, the flowsheet of the single cell of the PEM electrolysis unit is depicted. It is modelled by means of a RStoich operation block, where the water decomposition takes place, and a separator operation block. Mixers and splitters are also used for accounting of the water utilization factor in the anode side.

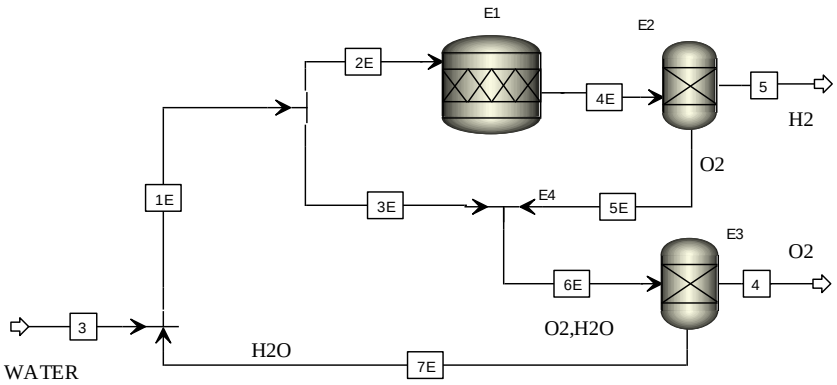

Figure 2.23 – Flowsheet of PEM electrolysis unit model.

The electrochemical behaviour of the electrolysis module is simulated by means of a Fortran calculator block in which the average cell polarization curve of each stack is calculated through the following equation that takes into account the polarization losses (i.e., activation overpotential, ohmic overpotential, and concentration overpotential):

$$V_{cell} = V_0 + b \cdot ln(J_{cell}) + R \cdot J_{cell} + m \cdot exp\,(-n \cdot J_{cell}) \qquad (2.12)$$

In the above equation, V_0 (V), b (V/dec), R (W·cm^2), m (V), and n (cm/A) are the fitting parameters calculated by applying a regression technique on the experimental data of the 3-cells stack reported in [76] and operating at 20 bar and 54, whereas J_{cell} is the current density (A/cm^2).

By considering the cells stack number (n_{cells}) and the cell area (A_{cell}, cm^2), the electric DC stack power (kW) required at different current is:

$$P_{el,\text{Stack}} = \frac{n_{cells} \cdot V_{cell} \cdot J_{cell} \cdot A_{cell}}{1000} \tag{2.13}$$

The stack hydrogen production (mol/s) is calculated by applying the Fick's law:

$$n_{H2,\text{Stack}} = \frac{n_{cell} \cdot J_{cell} \cdot A_{cell}}{2F} \tag{2.14}$$

where F is the Faraday's constant.

The electric power consumption of the electrolysis unit is:

$$P_{el,EU} = N_{Modules} \cdot N_{\text{Stack}} \cdot P_{el,\text{Stack}} + P_{aux} \tag{2.15}$$

where $N_{Modules}$ is the modules number, N_{Stack} is the stack number per module, and P_{aux} (kW) is the power adsorbed by the auxiliaries calculated as percentage of the nominal power consumption.

The specific electric consumption (kWh/kg) for hydrogen generation, that is a usual performance index of an electrolyser, is calculated as:

$$E_{SC} = \frac{P_{el,EU}}{\dot{m}_{H2,EU} \cdot 3600} \tag{2.16}$$

where $\dot{m}_{H2,EU}$ is the hydrogen mass flow generated, expressed in kilogram per second.

2.3.1.3.2 Methanation Unit (METUNIT Hierarchy)

The parameters that control the CO_2 methanation are the temperature, the pressure, and the feed gases ratio. As previously discussed, the methanation is favoured at temperatures in the range of 200 – 550 °C and at high pressure. In order to obtain a gas mixture with a high methane content, the ratio of the feed gases H_2/CO_2 must be equal to the stoichiometric value according to the reaction R1. Moreover, experimental data available in scientific literature [63,77] show how full chemical equilibrium is obtained when operating the CO_2 methanation reaction above the stoichiometric ratio of 4. As catalyst, nickel is considered to be the optimum choice due to its relatively

high activity, good CH_4 selectivity, and low raw material price [46], but require a high purity of the feeding gas.

The flowsheet of the developed model of the methanation unit, similar to the TREMP process, is shown in Figure 2.24.

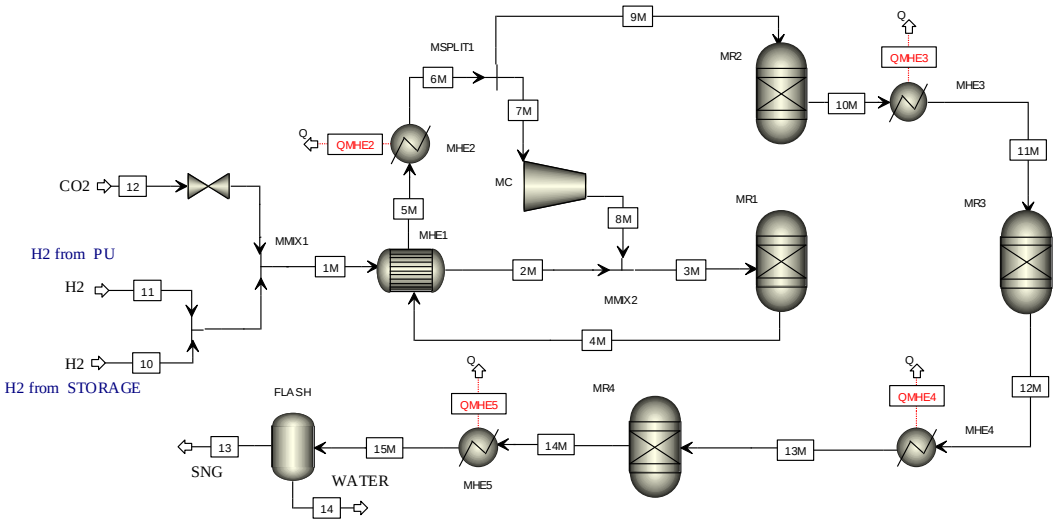

Figure 2.24 – Flowsheet of the methanation unit model.

The methanation is modelled by assuming the chemical equilibrium and the adiabatic conditions in each chemical reactor. Thus, according to the plant layout reported in Figure 2.18, the methanation unit mainly consists of four adiabatic reactors (MR1, MR2, MR3, and MR4) connected in series with intermediate gas cooling (the temperature of the streams exiting the heat exchangers MHE2, MHE3 and MHE4 is set to 250 °C), a heat exchanger (MHE1) (for preheating the feed gases up to the MR1 inlet temperature of 250 °C), and a flash drum for water removal from the wet SNG. Moreover, in order to control the temperature in the MR1, the product gas is partially recirculated to it by means of a splitter operation block (the recirculation factor is 0.70). The wet SNG leaving the MR4 reactor is cooled down to 229 °C (MHE5) before the flash drum operation block where the 99.7% of the product water is removed.

The chemical reactors are simulated using the RGibbs operation block, where the chemical equilibrium of a given set of species is solved through the minimization of the Gibbs free energy. This nonstoichiometric approach allows to find the equilibrium composition when the reactions system is unknown or very complex. Moreover, the hypothesis is that by reaching the chemical equilibrium the gas system can be formed by H_2, CO, CO_2, H2O, CH_4, and $C_{(s)}$.

Thermal power (QMHE2, QMHE3, QMHE4, and QMHE5) is also available by recovering the cooling heat from the heat exchangers MHE2, MHE3, MHE4, and MHE5.

The proposed model has been validated by means of the experimental data reported in [66]. In this case, the feeding gas is a syngas coming from a biomass gasification unit and only three methanation reactors are considered. The results of the model validation of the methanation unit are reported in Appendix A.

2.3.1.3.3 Storage Unit (STORAGE Hierarchy)

The storage unit is modelled by means of mixer, splitter, and calculator block to simulate the storage conditions in steady state. The stream STOR0 (see Figure 2.22) is a virtual stream needed to close the mass balance that is equal to the hydrogen stored in the tank. In a calculator block, the mass balance of the storage tank is implemented.

2.3.1.3.4 SNG Upgrading Unit (SNGUP Hierarchy)

Figure 2.25 shows the flowsheet of the SNG upgrading model. The dehydration membrane is modelled by means of a separator operation block with an assigned separation efficiency. The SNG compressor is a two-stage intercooled compressor.

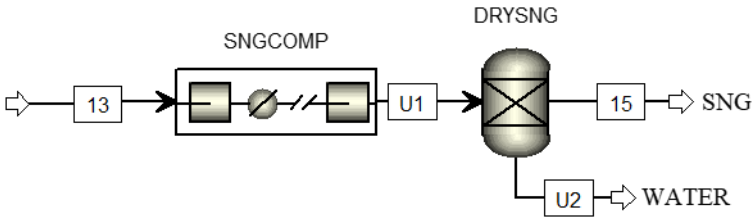

Figure 2.25 – Flowsheet of SNG upgrading unit model.

2.3.1.4 Storage control strategy

The storage unit allows to decouple the dynamics of the PEM electrolysis unit from that of the methanation unit. The parameter that controls the start and the operation modes of the methanation unit is the hydrogen storage pressure. As management strategy, three operation modes are allowed: (i) full load in which the hydrogen flow rate is equal to the nominal value, (ii) partial load in which the hydrogen flow rate varies linearly from 40% to 100% of the nominal value according to the specified minimum and maximum storage pressures, and (iii) hot standby mode in which no

hydrogen feeds the unit; in this operation mode, the heat losses of all the items of equipment have to be compensated by electrical heat tracing system [75,78].

Thus, it is assumed that at the beginning of the operation, the storage tank is empty. According to the wind energy supply, the product hydrogen is sent to the storage unit until the pressure in the tank reaches the maximum value (maximum storage pressure, $p_{storage,max}$) and the tank is completely full. In this condition, the methanation unit starts at full load and the corresponding hydrogen flow rate is directly delivered from the electrolysis unit or from the storage unit or from both, depending on the electrical supply (i.e., if the product hydrogen is less than the required flow rate, the remaining is delivered from the storage). When the pressure in the storage tank decreases, the hydrogen flow rate sent to the methanation unit decreases too, and the operation mode is switched to partial load. This operation mode goes on until the storage pressure reaches a threshold value (shutdown pressure, $p_{storage,SD}$) beyond which the methanation unit is kept in hot standby.

When the methanation unit is in hot standby, the hydrogen generated from the electrolysis is sent to the storage unit until the pressure rises a threshold value (restart pressure, $p_{storage,RS}$) beyond which the methanation unit restarts under partial load conditions. During the shutdown and restarting phases, the reactors are flushed with hydrogen (1/12 of the nominal flow rate for 1 h, as reported in ref. [74]).

The pressure in the storage tank is calculated by applying the EoS for ideal gases:

$$p_{storage}^{t} = p_{storage}^{t-1} + \frac{(m_{H2,EU}^{t} - m_{H2,MU}^{t}) \cdot R_{H_2} \cdot T_{storage}}{V_{storage}} \tag{2.17}$$

where $p_{storage}^{t}$ (Pa) and $p_{storage}^{t-1}$ (Pa) are the storage pressure at the time t (h) and t-1 (h), $m_{H2,EU}^{t}$ (kg) is the hydrogen mass produced in one hour at the time t, $m_{H2,MU}^{t}$ (kg) is the hydrogen mass sent to the methanation unit in one hour at the time t, R_{H_2} is the hydrogen gas constant (J/kg·K), $T_{storage}$ (K) and $V_{storage}$ (m^3) are the storage temperature and tank volume, respectively.

The input parameters of the model are the storage capacity, expressed in kg of stored hydrogen, the storage temperature, the maximum and minimum storage pressures, the shutdown and restart pressure, and the hydrogen flow rate feeding the methanation unit at full load. In this study the storage capacity is chosen for assuring 6.5 hours of full load operation of the methanation unit.

The control strategy proposed has been implemented by using the MATLAB package software. In the Appendix A, the flow chart of the storage model is reported.

2.3.2 Results and discussion

2.3.2.1 Performance parameters

The nominal efficiencies of the electrolysis unit and the methanation unit as well as the overall nominal efficiency of the PtSNG plant are defined as the ratio between the useful output powers (i.e., the chemical power of the hydrogen or the SNG) and the input powers (i.e., the wind electric power or the chemical power of hydrogen). Therefore, the nominal efficiency of the PEM electrolysis unit is:

$$\eta_{EU} = \frac{\Phi_{H_2,EU}}{P_{el,EU}} \tag{2.18}$$

where $\Phi_{H_2,EU}$ is the chemical power of the produced hydrogen at nominal conditions calculated on LHV basis, and $P_{el,EU}$ is the electric power consumed by the electrolysis unit in DC. It is equal to the input renewable power multiplied by the rectifier efficiency.

The nominal efficiency of the methanation unit is:

$$\eta_{MU} = \frac{\Phi_{SNG,MU}}{\Phi_{H_2,MU} + P_{el,MU}} \tag{2.19}$$

where $\Phi_{SNG,MU}$ and $\Phi_{H_2,MU}$ are the chemical powers of the hydrogen feeding and the SNG exiting the methanation unit at nominal conditions and $P_{el,MU}$ is the electric power consumption of recirculation blower.

The thermal power available from the heat exchangers is not accounted in this calculation.

The nominal overall efficiency of the PtSNG plant results:

$$\eta_{PtSNG} = \frac{\Phi_{SNG}}{P_{el,RES} + P_{el,H_2} + P_{el,MU} + P_{el,SNG} - \Phi_{H_2,storage}} \tag{2.20}$$

In the above equation, Φ_{SNG} is the SNG chemical power generated, $P_{el,RES}$ is the wind power supply to the electrolysis unit in AC, P_{el,H_2} is the power consumption of the hydrogen compressor, $P_{el,SNG}$ is the power consumption of the SNG compressor, and $\Phi_{H_2,storage}$ is the hydrogen chemical power sent to the storage unit.

Because of the fluctuating behaviour of the input energy source, the nominal efficiencies are not sufficient to evaluate the effectiveness of the plant, but it is necessary to evaluate the annual performance [79]. This is defined as the ratio of usable system energy output to overall system energy input (electricity and possibly heat)

[79,80]. Therefore, the annual efficiencies of the energy conversion units and the annual overall efficiency are calculated as the nominal efficiencies, by replacing the power with the energy (electric or chemical) consumed or generated in one year of operation. However, the thermal energy required to maintain the plant equipment in hot stand-by during the no production hours should be added as energy input:

$$\varepsilon_{EU} = \frac{E_{H_2,EU}}{E_{el,EU} + E_{th,EU,HS}} \tag{2.21}$$

$$\varepsilon_{MU} = \frac{E_{SNG,MU}}{E_{H_2,MU} + E_{el,MU} + E_{th,MU,HS}} \tag{2.22}$$

$$\varepsilon_{PtSNG} = \frac{E_{SNG}}{E_{el,RES} + E_{el,H_2} + E_{el,MU} + E_{el,SNG} - E_{H_2,storage} + E_{th,MU,HS} + E_{th,EU,HS}} \tag{2.23}$$

where $E_{th,EU,HS}$ and $E_{th,MU,HS}$ are the thermal energy required to maintain system in hot standby during the no production hours, and $E_{H_2,storage}$ is the chemical energy of the remaining hydrogen in the storage tank.

A useful performance parameter for evaluating the correct sizing of the plant is the plant load factor. It compares the annual chemical energy production of the produced SNG with the maximum production in one year:

$$PLF_{PtSNG} = \frac{E_{SNG}}{8760 \cdot \Phi_{SNG}} \tag{2.24}$$

where $\Phi_{SNG}$is the plant production at rated power.

2.3.2.2 Plants sizing and performance assessment at nominal conditions

The integrated model described in the previous section has been applied for evaluating the mass and energy balance of the PtSNG plants at nominal conditions (full load mode). Because of the same operating conditions, the plants differ only for the input and output mass and energy fluxes.

Table 2.9 summarizes the common operating data and parameters.

The PEM electrolysis unit consists of modules of 1 MWDC that is the base module for all plant sizes considered. The chosen nominal operating conditions, in terms of current density and average cell voltage for each stack, are 2.99 A/cm^2 and 2.17 V, respectively, and are derived from the polarization curve calculated by means of Eq. (2.12). By fixing the cell area (1000 cm^2) and the number of stacks per module (3), the

number of cells per stack results equal to 55. The power consumption of the module auxiliaries is set to 2.8% of the rated power. At nominal conditions, the hydrogen generated by the module results equal to 16.8 kg/h with a specific energy consumption of 59.6 kWh/kg of the produced hydrogen.

The operating pressure of the methanation unit is set to 20 bar since higher methanation pressures do not have a significant impact on the methane content in the product gas mixture, as discussed in the paragraph 2.3.1.3.2. In order to contain the hydrogen storage tank capacity, the methanation unit is sized for processing the maximum hydrogen flow produced by the electrolysis unit. This choice makes the decoupling between the dynamics of the electrolysis unit and that of the methanation unit less effective but reduces the plant capital costs (based on the storage pressure of 50 bar, the cost is estimated 375 €/kg [74]).

Table 2.9 – Common operating data of PtSNG plants.

Plant Sections and Components	
PEM electrolysis module	
AC/DC rectifier efficiency [%]	95
Stacks number x module	3
Cells number x stack	50
Active cell area [cm^2]	1000
Cell Temperature [°C]	55
Water utilization factor, UF	0.45
Average cell voltage at nominal power [V]	2.17
Current density at nominal power [A/cm^2]	2.99
Auxiliaries [% of rated power]	2.8
Inverter AC/DC efficiency [%]	95
Methanation Unit	
Pressure [bar]	20
H_2/CO_2 [mol/mol]	4
Recycle ratio to the reactor MR1	0.70
MR1 exit temperature [°C]	561
MR2 exit temperature [°C]	412
MR3 exit temperature [°C]	301
MR4 exit temperature [°C]	260
Recycle compressor efficiency [%]	80
Hydrogen Compressor	

Pressure ratio	2.25
Isentropic efficiency [%]	70
Storage Unit	
Maximum Storage pressure [bar]	45
Minimum Storage pressure [bar]	22
Storage temperature [°C]	30
SNG Upgrading unit	
Dehydration membrane efficiency [%]	90
SNG compressor pressure ratio	1.75
Isentropic efficiency [%]	75

Moreover, the hydrogen storage unit is designed for assuring the full load operation of the methanation unit for about 6.5 h. The maximum storage pressure and the storage temperature are assumed equal to 45 bar and 30 °C, while the minimum pressure in the storage tank is set to 22 bar in order to allow the feeding of the methanation unit without a compression system.

In Table 2.10, the mass and energy balances of the considered PtSNG plant sizes are reported. The electrolysis unit consists of 1, 3, and 6 modules and generates 16.8, 50.5, and 101.0 kg/s of hydrogen, respectively. The composition of the produced SNG is 95.9% mol CH_4, 3.3% mol H_2, 0.8% mol CO_2, and traces of H_2O, and its low heating value (LHV) is 49.2 MJ/kg, whereas the calculated Wobbe Index is 49.7 MJ/Nm^3. These values fill with the quality foreseen by the ongoing work on European standardization of PtH_2 applications, for which most of the European natural gas infrastructure can withstand a volume concentration 10% of hydrogen. Depending on the electrolysis unit capacity (1, 3, or 6 MW), the SNG production is equal to 34.1, 102.4, and 204.9 kg/s, respectively, while the maximum amount of the stored hydrogen is 110, 325, and 650 kg, respectively. By considering the storage conditions (45 bar and 30 °C), the tank capacities are 30, 90, and 180 m^3, respectively.

Table 2.10 – Mass and energy balances under nominal conditions.

PtSNG plant capacity (electrical power input DC)	1 MW	3 MW	6 MW
Wind Energy supply [kW_{AC}]	1051	3155	6309
Plant Sections and Components			
PEM Electrolysis Unit (ELUNIT)			
Number of power modules	1	3	6
Water consumption [kg/h]	150.3	451.0	902.0

Hydrogen production [kg/h]	16.8	50.5	101.0
Thermal power consumption [kW]	5.8	17.4	34.8
Electric power consumption [kW_{DC}]	998.9	2996.8	5993.6
Methanation Unit (METUNIT)			
Carbon dioxide mass flow [kg/h]	91.9	275.7	551.3
Hydrogen mass flow [kg/h]	16.8	50.5	101.0
Thermal power from MHE2 [kW]	63.6	190.1	381.7
Thermal power from MHE3 [kW]	12.3	36.7	73.6
Thermal power from MHE4 [kW]	3.8	11.3	22.6
Thermal power from MHE5 [kW]	2.2	6.6	13.3
Recycle blower consumption [kW]	0.5	1.4	2.8
Raw SNG composition [mol %]	95.5 CH_4, 3.2 H_2, 0.8 CO_2, 0.5 H_2O		
Storage Unit (STORAGE)			
Storage capacity [kg of H_2]	110	325	650
Storage volume at 30 °C [m^3]	30	90	180
SNG upgrading (SNGUP)			
Electric power consumption [kW]	1.1	3.4	6.8
SNG production [kg/h]	34.1	102.4	204.9
Plant Performances			
SNG composition [mol %]	95.9 CH_4, 3.3 H_2, 0.8 CO_2, traces H_2O		
SNG LHV/HHV [MJ/kg]	49.2/54.7		
Wobbe index [MJ/Nm^3]	49.7		

2.3.2.3 Dynamic operation and annual mass and energy balance

The time-domain simulation of the PtSNG system has been performed using MATLAB computing software. The annual energy balance of the PtSNG plant has been carried out by assuming that each electrolysis module can operate between the 20% (200 kWh_{DC}) and 100% of its nominal load [78], while, as previously discussed, the minimum load of the methanation unit for assuring the quality of the produced SNG is 40%. The isentropic efficiencies of the BoP components and devices such as the hydrogen compressor and the SNG compressor have been assumed constant because of their very small impact on the total electric consumptions (about 0.1% of the electric consumption of the electrolysis unit).

The efficiency of the electrolysis unit varies with the power supplied as well as the hydrogen production. Using the specific energy consumption defined in Eq. (2.16) and

reported in Figure 2.26, the hydrogen production (kg) as function of the supplied wind energy (kWh) is obtained by the following equation:

$$M_{H_2} = \frac{E_{Wind,supplied} \cdot \eta_{AC/DC}}{E_{SC}} \quad (2.25)$$

where $E_{Wind,supplied}$ (kWhAC) is the hourly electricity supplied to the electrolysis unit (it depends on the stored energy factor) and $\eta_{AC/DC}$ is the rectifier efficiency.

Therefore, by starting from the hourly electric energy generated by the wind farm and by applying the integrated PtSNG model, the hourly hydrogen production as well as the hourly mass and energy balances are calculated for each plant size. In Table 2.11, the annual operation time of the electrolysis and methanation units are reported for the three plant sizes.

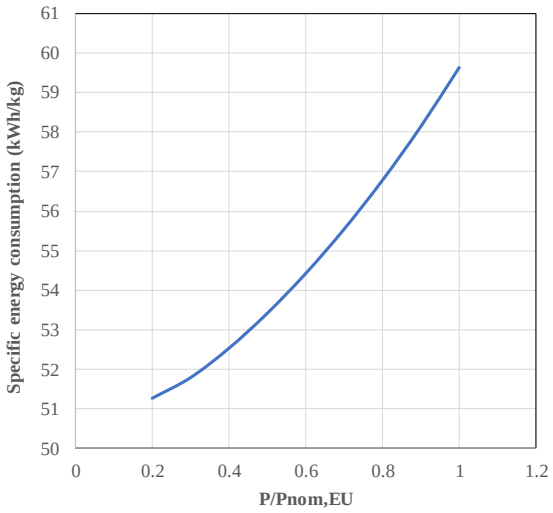

Figure 2.26 – Specific energy consumption of the electrolysis module in the load range.

Table 2.11 – Annual operation time.

	1 MW		3 MW		6 MW	
Stored Energy Factor [%]	22%		52%		79%	
Plant section	EU	MU	EU	MU	EU	MU
Operation time [h]	5868	6047	5868	5004	5868	4170
Full load [h]	4372	2500	2813	1256	1646	486
Partial load [h]	1496	3547	3055	3748	4222	3684
Hot standby [h]	2892	2713	2892	3756	2892	4590
Shutdown	477	212	477	225	477	233
ON/OFF cycle	117	0	117	0	117	0

The annual operation time of the EU unit results equal to 5868 h with 477 shutdown and 117 ON/OFF cycles. While the annual operation time of the EU unit only depends on the wind energy availability, the full load and partial load hours strictly depends on the chosen size of the EU. Therefore, as expected (see Figure 2.19), the full load time decreases from 4372 to 2813 h (-35.7%) and 1646 h (-63.2%). With respect to the annual operation time of the methanation unit, the greatest value (6047 h) is obtained for the PtSNG plant sized for 1 MW of energy input, whereas in the cases of 3 and 6 MW, it results smaller than the annual operation time of the electrolysis unit. In order to increase the annual operation time of the methanation unit, a smaller hydrogen flow rate at full load mode (i.e., the nominal hydrogen flow rate) has to be chosen, involving, however, the need of higher capacities for the storage. The calculated shutdowns are more than halved (212, 225, and 233), and the ON/OFF cycles are suppressed.

The flushed hydrogen flows are 641, 2142, and 4520 kg/year for 1, 3, and 6 MW, respectively.

Table 2.12 summarizes the annual mass and energy balance and the annual efficiencies of the PtSNG plants.

The annual overall efficiencies are decreasing with the plant size (from 43.7% to 41.6%), due to the growing impact of the energy required to balance the heat losses in the hot standby mode (the standby period increases from 2713 to 4590 h). This may suggest that, in the case in which the standby period is significant (this estimation should be made in terms of forecasting), it could be better to keep the system in cold standby, even if the start-up procedure use more energy depending on the duration of the plant downtime.

Finally, the plant load factor shows the greatest value (60.0%) in the case of 1 MW plant capacity and the smallest (35.4%) for the 6 MW plant capacity.

Table 2.12 – Annual mass and energy balance.

PtSNG plant capacity (electrical power input DC)	1 MW	3 MW	6 MW
Volumetric flow rates [10^3 Nm3/year]			
Annual H_2O consumption	0.79	1.85	2.83
Annual H_2 production	1000	2338	3573
Annual CO_2 consumption	248	585	894
Annual H_2 consumption	999	2334	3567
Annual SNG production	179	417	635
Energy [MWh/year]			

Annual electric energy consumption of the electrolysis unit (AC/DC)	5483/5209	12849/12207	19661/18768
Annual electric energy consumption for compressors and auxiliaries	15	37	62
Annual electric energy consumption for hot-standby*	106	458	1143
Annual SNG chemical energy (LHV basis)	2448	5705	8683
Chemical energy of the remaining hydrogen** (LHV basis)	4	10	17
Plant Performances			
Stored energy factor [%]	22.0	51.5	78.8
Electrolysis unit annual efficiency (LHV basis)	56.6	56.6	56.6
Methanation unit annual efficiency (LHV basis)	80.0	77.4	74.2
SNG Plant annual efficiency (LHV basis) [%]	43.7	42.8	41.6
Plant load factor [%]	60.0	46.5	35.4

*The thermal energy required to maintain the equipment in hot standby is calculated by using the data reported in ,[75] that considers electrical trace heating.

**The remaining hydrogen in the storage tank is the difference between the annual hydrogen production and the annual hydrogen consumption

2.4 *Case study #3: Heat recovery from a PtSNG plant coupled with wind energy*

2.4.1 Material and methods

2.4.1.1 PtSNG Plant description

The PtSNG plant, shown in Figure 2.27, is directly coupled with a 12 MW wind farm and is sized for 1 MW of electric power input. It consists of four sections: i) the hydrogen generation unit based on the proton exchange membrane (PEM) electrolyser, ii) the methanation unit based on the fixed-bed reactors technology, iii) the H_2 storage unit, in which gaseous hydrogen is stored into pressurised vessels and iv) the SNG upgrading unit based on the membrane technologies.

The demineralised water (1) is pumped and heated to the operative pressure and temperature of the PEM electrolysis unit where O_2 and H_2 are produced. On the basis of a specific control strategy, H_2 generated via electrolysis (5) can be partially or totally sent to the methanation unit (6) and/or to the intercooled compressor C1 (8) to increase the pressure up to the maximum storage pressure. The compressed H_2 (9) is stored in high-pressure tanks. The H_2 streams from electrolysis unit and/or storage unit are mixed with the CO_2 stream (13) from the CO_2 storage unit. The CO_2 is assumed to be always available for the PtSNG plant (i.e., supplied by sequestration from other power plants or industrial processes) at the storage pressure of 200 bar.

The methanation unit consists of four adiabatic fixed-bed reactors (MR1, MR2, MR3, MR4) connected in series with intermediate gas cooling (heat exchangers MHE1, MHE2, MHE3) for assuring the fixed inlet reactors temperatures. The H_2 and the CO2 entering the methanation unit are mixed with the hydrogen (19) from the SNG upgrading unit and then preheated up to the inlet temperature of the methanation reactor MR1 (300 °C). This preheating is performed by mixing the reactant flow (14) with hot streams from the MR1 and MHE1 defined by specified recirculation ratios (stream 3M at the splitter SPT1 and stream 8M at the splitter SPT2). Thus, the syngas (9M) sent to the MR2 reactor is a fraction of the product gases leaving the first methanation reactor. In the following reactors (MR3 and MR4) the CO_2 hydrogenation is led at decreasing temperature levels, reaching the conversion of 94% at the exit of the last methanation reactor. During the methanation process a large amount of water is produced, so the raw SNG (14M) is cooled in the heat exchanger MHE4 and sent to the FLASH unit for water removal. In order to meet the required grid specifications [81] the SNG (15) is further upgraded by means of a dehydration membrane (a commercial Pebax®-based membrane [72]) to eliminate the residual moisture to comply with the H_2O dew point requirements of the pipelines and of a H_2 separation membrane (polysolfone-based membrane).

The quality of the SNG exiting from the upgrading section (20) satisfies the current pipelines specifications effective in various European countries, as reported in [81] and therefore, can be directly injected into the low-medium pressure NG transmission network. If the country specific pipeline requirements are more stringent, additional CO_2 or H_2 removal systems should be considered. The hydrogen from the upgrading unit is recycled to the first methanation reactor, as mentioned above.

Finally, the waste heat available from the methanation unit and the flash unit can be usefully recovered in the waste heat recovery system according to concepts that will be described below.

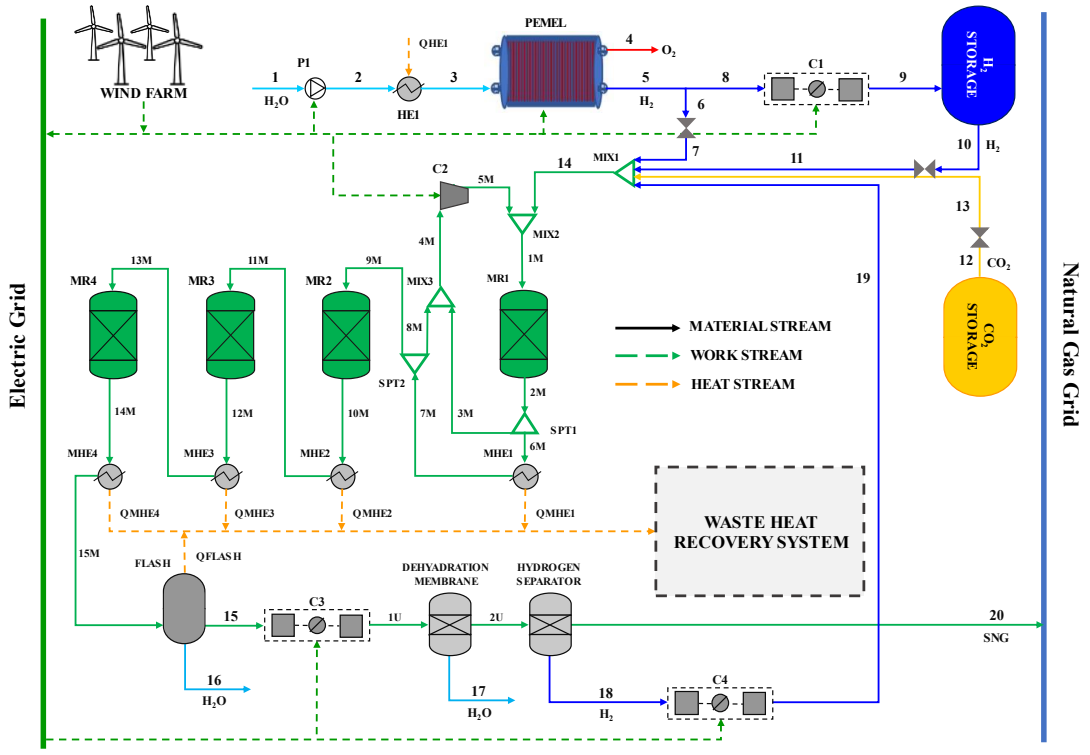

Figure 2.27 – PtSNG plant layout.

The PtSNG plant is operated in input-oriented mode. In order to maximise the operating hours of the plant, a hydrogen storage unit is employed to decouple the H2 generation and the SNG production.

As management strategy, four operation modes are allowed for the methanation unit: i) full load, in which the hydrogen flow rate entering the methanation unit from the storage and/or the electrolyser is equal to the nominal value; ii) partial load, in which the hydrogen flow rate sent to methanation reactors varies from 40% to 100% of the nominal value, according to the specified minimum and maximum hydrogen storage pressures; iii) hot-standby mode, in which the reactors are kept at the minimum operating temperature of the catalysts to allow a quick restart; iv) cold-standby mode, in which no carbon dioxide and hydrogen feed the methanation unit. Even if the restart from cold-standby requires more energy than that required to maintain the hot-standby, this operation mode can be convenient when the number of hours from the shut-down to the restart is high. The parameter that controls the start of the plant and the operation modes of the methanation unit is the hydrogen storage pressure that follows the control strategy widely described in [82].

The mass and energy balances of the PtSNG plant in steady state conditions as well as the annual performance of the plant are performed by applying the thermochemical

and electrochemical model (in Aspen Plus environment) and the dynamic model (in MATLAB environment) developed and described in [82].

The thermochemical and electrochemical model consists of sub-models for each plant section; in this study the sub-model of the methanation unit, modified by considering the kinetics of the process, is described in Appendix B.

The dynamic model based on the annual hourly energy input (the wind energy supplied to the plant) and on the storage control strategy allows forecasting the annual operation time (full and partial load hours, standby hours) and the annual performances (SNG production, energy consumption, efficiency) of the PtSNG plant.

2.4.1.2 Heat recovery management

The heat recovery management is based on the valorisation of the waste heat, generated during the plant operation in the methanation unit, to self-sustain, from an energetic point of view, the standby conditions. To this end, two heat recovery configurations based on different heat recovery concepts are proposed and investigated. In both configurations, the recovery of the waste heat coming from the methanation unit is performed by means of a heat transfer fluid (i.e., diathermic oil) stored in insulated tanks for thermal energy storage.

Figure 2.28 shows the conceptual schemes of the two heat recovery systems.

In the first one (Thermal storage configuration, Figure 2.28.a), the stored thermal energy is used to satisfy the thermal energy demand of the reactors during the standby periods by means of a thermal carrier.

In the second one (Electrical storage configuration, Figure 2.28.b), the stored thermal energy is used to produce electricity by means of an organic Rankine cycle (ORC). This electrical energy is stored in batteries, and it is used to meet the energy requirements of the electrical trace heating system of the methanation unit during the standby periods. In this case the stored electric energy is also used to satisfy the ancillary equipment electricity demand.

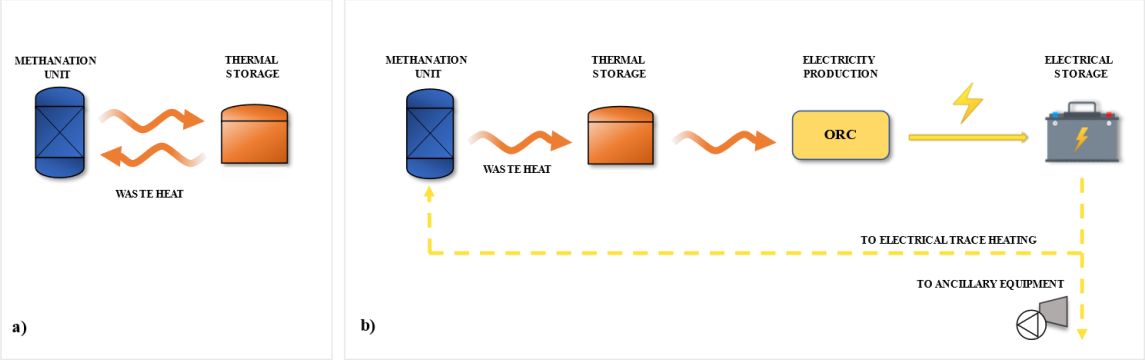

Figure 2.28 – Conceptual schemes and energy flows of the two proposed waste heat recovery systems: a) Thermal storage; b) Electrical storage.

In the first one (thermal storage configuration, Figure 2.28.a, the stored thermal energy is used to satisfy the thermal energy demand of the reactors during the standby periods by means of a thermal carrier.

In the second one (electrical storage configuration, Figure 2.28.b, the stored thermal energy is used to produce electricity by means of an Organic Rankine Cycle (ORC). This electrical energy is stored in batteries, and it is used to meet the energy requirements of the electrical trace heating system of the methanation unit during the standby periods. In this case, the stored electric energy is also used to satisfy the ancillary equipment electricity demand.

2.4.1.2.1 Thermal storage

In the thermal storage system, the waste heat is recovered and stored by means of a two-tanks diathermic oil circuit; the stored thermal energy is supplied, when required, to the methanation reactors by means of a thermal carrier. Hydrogen is used as thermal carrier because it removes the residual carbon dioxide preventing catalyst deactivation. Figure 2.29 shows the layout of the thermal storage configuration.

During the plant operation, the diathermic oil (1HR) from the cold oil tank is pushed (2HR) by the pump P2 and sent to the methanation unit for heat recovering (heat exchangers MHE1, MHE2, MHE3, MHE4 and the FLASH unit) in such a way to minimise the temperature gradients and to optimise the heat transfer efficiencies; at the exit of the MHE1 the hot diathermic oil (7HR) is stored into the hot oil tank.

When the reactors need to be heated, the diathermic oil from the hot oil tank is sent to the heat exchanger HRHE1 for heating the hydrogen used as thermal carrier. The diathermic oil leaving the HRHE1 is cooled down in the HRHE2 to the storage

temperature of the cold oil tank. This cooling heat can be further recovered for external or internal use.

The thermal power transferred by the hot hydrogen allows to compensate for the thermal losses in all the reactors and to keep the temperature of the catalysts within the activation range. The cold H_2 (15HR) is recovered downstream the last reactor MR4 to be recirculated again.

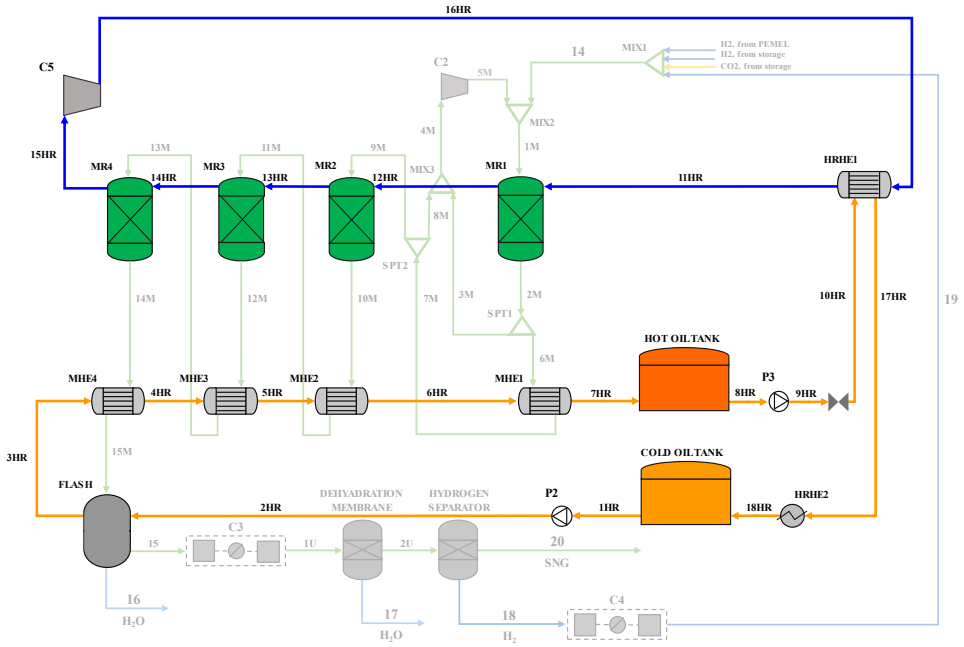

Figure 2.29 – Schematic diagram of thermal storage system.

2.4.1.2.2 Electrical storage

In the electrical storage system, the waste heat is recovered by means of a two-tanks diathermic oil circuit (they are conceived as buffer tanks) and the stored thermal energy is used to generate electricity via an Organic Rankine Cycle (ORC). The oil tanks allow to ensure continuous and stable operation of the ORC by decoupling the heat storage (which depends on the methanation unit operation) from the electricity production. The produced electricity, stored in batteries, is supplied, when required, to the electrical trace heating system of the methanation unit and used for ancillary equipment.

Figure 2.30 depicts the electrical storage configuration.

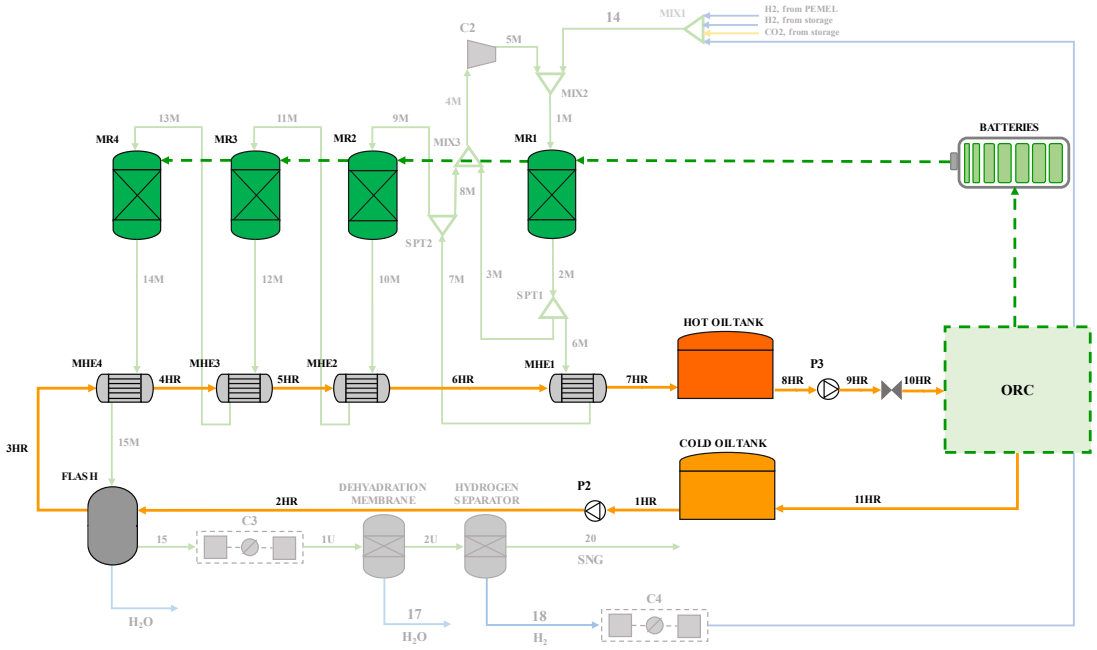

Figure 2.30 – Schematic diagram of electrical storage system.

The diathermic oil circuit works as described in the thermal storage configuration. When the hot oil tank is full, the diathermic oil (8HR) is sent to the ORC unit for supplying the thermal power required by the ORC cycle. The returning cold oil (11HR) is then stored in the cold oil tank.

With referring to the ORC power unit, by taking into account the heat sources temperatures as well as additional features (low toxicity, low global warming potential and ozone depletion potential, good compatibility and chemical stability in operation with other materials, etc.), the iso-butane (R600a) is selected as working fluid. In Figure 2.31, the functional scheme of the ORC power unit is shown.

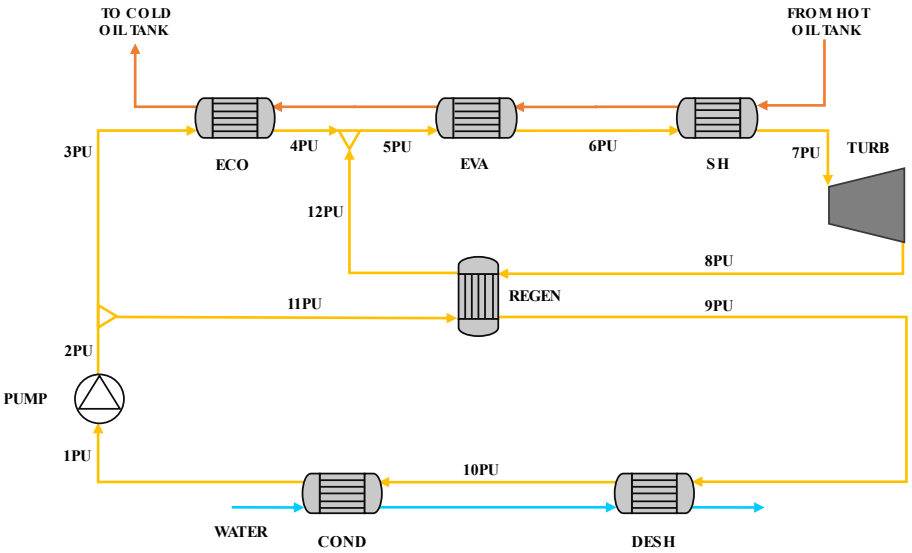

Figure 2.31 – Functional scheme of the ORC.

The organic fluid (1PU) leaving the condenser (COND) is pressurised up to the maximum pressure of the cycle (2PU). In order to optimise the use of the heat from the thermal storage and the heat internally available, it is split in two streams 3PU and 11PU. The first one (3PU) is sent to the economiser (ECO) where it is pre-heated up to the saturation condition (4PU) by the diathermic oil, while the second one is pre-heated (12PU) in the regenerator (REGEN) by the stream 8PU that exits the scroll expander, that is still in superheated condition (the iso-butane is a dry fluid). The streams 4PU and 12PU are mixed and the resulting is vaporised and superheated up to the turbine inlet temperature by the diathermic oil. The superheated vapour (7PU) expands in the scroll expander down to the condenser pressure. The desuperheating of the iso-butane (9PU) is completed in the heat exchanger DESH where it is cooled down to its dew-point temperature (10PU) and finally condensed in the condenser (COND).

2.4.1.3 Heat recovery system sizing criteria

Both proposed heat recovery configurations are sized for assuring the thermal energy needed to maintain the hot-standby conditions of the methanation unit and the thermal energy needed for the cold restart.

The sizing procedure of the heat recovery systems is performed through the evaluation of (i) the thermal energy that can be recovered from the methanation unit (QMHE1, QMHE2, QMHE3, QMHE4) and the flash unit (QMHE5) and the temperatures at which they are available; (ii) the thermal energy required by the methanation unit in the hot-standby status and that required for the restart after a cold-

standby; (iii) the optimal combination between the number of hot-standby hours and that of cold-standby.

The thermal energy recoverable from the methanation unit and the flash unit as well as the temperatures at which it is available is assessed by the mass and energy balance of the plant.

The thermal energy needed to maintain the hot-standby status (i.e., to maintain the reactors at the catalysts activation temperature) as well as that needed to warmup the reactors after a cold-standby (the thermal energy consumption to warm-up the reactors from ambient temperature to the catalysts activation temperature) has been calculated by considering convective and conductive heat transfer mechanisms.

The standby hours are calculated by applying the dynamic model. The number of hours of hot-standby and, as a consequence, that of cold-standby, is evaluated by assuming the minimum capacity of the storage devices (the diathermic oil tanks for the thermal energy storage and the batteries for the electric energy storage) able to satisfy the energy requirements and, at the same time, to make the plant economically feasible. Thus, in order to identify the optimum combination between hot and cold-standby hours, statistical analysis of the plant's standby hours distribution is carried out in terms of the average duration and frequency. It is worth noting that this analysis is site-specific and closely linked to the typical annual wind energy profile of the considered plant, therefore tailor-made considerations would be required for other plants.

2.4.1.4 Performance parameters

The PtSNG plant nominal efficiency is defined as the ratio between the useful output powers (i.e., the chemical power of the SNG) and the input powers. The input powers for the PtSNG plant are represented by the electric power consumption for the electrolyser and the ancillary equipment, namely the hydrogen compressor for hydrogen storage, the blowers for the methanation unit and the raw SNG compressor and the hydrogen compressor for the upgrading unit. The efficiencies are calculated taking into account both the lower heating value (LHV) and the higher heating value (HHV) for the calculation of the chemical powers.

The nominal overall efficiency of the PtSNG plant results in the following equation:

$$\eta_{PtSNG} = \frac{\Phi_{SNG}}{P_{el,RES} + P_{el,H2} + P_{el,MU} + P_{el,UU}} \tag{2.26}$$

In the above equation, Φ_{SNG} is the chemical power of the generated SNG, $P_{el,RES}$ is the wind power supply to the electrolysis unit in AC, $P_{el,H2}$ is the power consumption of the hydrogen compressor for the H2 storage, $P_{el,MU}$ is the electric power consumption of recirculation blower in the methanation unit, $P_{el,UU}$ is the power consumption of the upgrading unit, that includes the power consumption of the SNG compressor and that of the hydrogen compressor downstream the hydrogen membrane separation. The thermal power available from the methanation unit heat exchangers is not accounted in this calculation.

Because of the fluctuating behaviour of the input energy source, the nominal efficiencies are not sufficient to evaluate the effectiveness of the plant, but it is necessary to evaluate the annual performance [78]. This is defined as the ratio of the usable system energy output to the overall system energy input (electricity and possibly heat) [75,78]. Therefore, the overall annual efficiency of the PtSNG plant is calculated as the nominal efficiency, by replacing the power with the energy (electric or chemical) consumed or generated in one year of operation. However, in this case, the thermal energy required to maintain the plant equipment in hot-standby during the no production hours, as well as that required to restart the reactors after a cold-standby, should be added as energy input:

$$\varepsilon_{PtSNG} = \frac{E_{SNG} + E_{H2,storage}}{E_{el,RES} + E_{el,H2} + E_{el,MU} + E_{el,UU} + E_{th,MU,HS} + E_{th,MU,CS}} \qquad (2.27)$$

where $E_{th,MU,HS}$ is the thermal energy required to maintain the methanation reactors in hot-standby during the no production hours, $E_{th,MU,CS}$ is the thermal energy required to warm up the reactors after a cold standby and $E_{H2,storage}$ is the chemical energy of the remaining hydrogen in the storage tank. For the purposes of calculating the efficiencies for the proposed configurations, having carried out the heat recovery necessary to make the plant self-sufficient from the point of view of the energy demands of the standby periods, the terms relating to the standby thermal requirements ($E_{th,MU,HS}$ and $E_{th,MU,CS}$) are considered null. Indeed, these energy requirements are satisfied by re-using internal energy.

2.4.2 Results and discussion

2.4.2.1 Plant mass and energy balance results

Table 2.13 summarises the main operating parameters of the PtSNG plant. The 1 MWDC PEM electrolysis unit consists of three stacks with nominal operating conditions, in terms of current density and average cell voltage for each stack, equal to 2.99 A/cm^2 and 2.17 V, respectively. The power consumption of the unit auxiliaries is set to 2.8% of the rated power. At nominal conditions, the hydrogen generated is equal to 16.8 kg/h with a specific energy consumption of 59.6 kWh/kg of the produced hydrogen. To contain the hydrogen storage tank capacity, the methanation unit is sized for processing the maximum hydrogen flow generated by the electrolysis unit. With this assumption, the decoupling between the dynamics of the electrolysis unit and that of the methanation unit is less effective, but the plant capital costs (based on the storage pressure of 50 bar, the cost is estimated at 375 €/kg [82]) are reduced. Furthermore, the hydrogen storage unit is sized to ensure the full-load operation of the methanation unit for about 6.5 h.

Table 2.13 – Operational data of PtSNG plant.

Plant Sections and Components	
PEM Electrolysis Unit	
Nominal power [MW]	1
AC/DC rectifier efficiency [%]	95
Stacks number/Cells number per stack	3/50
Active cell area [cm^2]	1000
Cell pressure/temperature [bar/°C]	20/55
Water utilization factor, UF	0.45
Current density [A/cm^2] @Average cell voltage [V] at rated power	2.17
Auxiliaries [% of rated power]	2.8
H_2 Compressor (C1)	
Pressure ratio	2.25
Isentropic efficiency [%]	70
H_2 Storage Unit	
Maximum Storage pressure [bar]	45
Minimum Storage pressure [bar]	22
Storage temperature [°C]	30
Methanation Unit	
Pressure [bar]	10
H_2/CO_2 [mol/mol]	4
Recycle ratio to MR1	0.70

Recycle ratio from SPT1 to MIX3	0.30
Recycle ratio from SPT2 to MIX3	0.57
MR1 in/out temperature [°C]	300/585
MR2 in/out temperature [°C]	300/468
MR3 in/out temperature [°C]	350/409
MR4 in/out temperature [°C]	350/365
Recycle blower (C2) isentropic efficiency [%]	85
SNG Upgrading Unit	
Dehydration membrane efficiency [%]	90
H_2 separation membrane efficiency [%]	90
SNG compressor (C3) pressure ratio	1.75
H_2 recycle compressor (C4) pressure ratio	10
Isentropic efficiency [%]	85

In Table 2.14, the mass and energy balances under nominal conditions are reported**.** The composition of the produced SNG is 92.5% mol CH_4, 2.2% mol H_2, 5.3% mol CO_2 and traces of H_2O, and its lower heating value (LHV) is 43.4 MJ/kg, whereas the calculated Wobbe Index is 43.9 MJ/Nm^3. This value fits with the quality foreseen by the ongoing work on European standardisation of PtH_2 applications, for which most of the European natural gas infrastructure can withstand a volume concentration 10% of hydrogen. The SNG production is equal to 38.52 kg/h while the maximum amount of the stored hydrogen is 110 kg. By considering the storage conditions (45 bar and 30 °C), the tank capacity is 30 m^3. The PtSNG plant efficiency on an LHV basis is 43.9%.

Table 2.14 – Mass and energy balances under nominal conditions.

PtSNG Plant Capacity (Electrical Power Input) [MW_{DC}]	**1 MW**
Wind Energy supply [kW_{AC}]	1051
Plant Sections and Components	
Water Pump (P1)	
Water pump power consumption [kW]	0.11
PEM Electrolysis Unit	
Number of power modules	1
H_2O consumption [kg/h]	150.3
H_2 production [kg/h]	16.8
Thermal power consumption [kW]	5.96
Electric power consumption [kW_{DC}]	998.9
H_2 Compressor (C1)	

Compressor power consumption [kW]	7.74
H_2 Storage Unit	
Storage capacity [kg of H_2]	110
Storage volume [m^3] at 30 °C	30
Methanation Unit	
Carbon dioxide mass flow [kg/h]	96.8
H_2 mass flow [kg/h]	17.74
H_2 recycle mass flow [kg/h]	0.912
Recycle blower (C2) power consumption [kW]	0.34
Raw SNG composition [mol %]	76.7 CH_4, 18.5 H_2, 4.4 CO_2, 0.3 H_2O
SNG upgrading	
SNG compressor (C3) power consumption [kW]	3.05
H_2 recycle compressor (C4) power consumption [kW]	1.08
Plant Performances	
SNG production [kg/h]	38.52
SNG composition [mol %]	92.5 CH_4, 2.2 H_2, 5.3 CO_2, traces H_2O
SNG LHV/HHV basis [MJ/kg]	43.4/48.2
SNG LHV/HHV [MJ/Nm^3]	30.5/33.9
SNG Plant nominal efficiency, LHV/HHV basis [%]	43.9/48.8

Table 2.15 reports the thermal powers recoverable from the methanation unit and the flash unit as well as the range of temperature at which they are available. It is worth nothing that, due to the water condensation, a large amount of heat is available in the flash unit, albeit at a low temperature. In heat exchanger MHE4, the thermal energy is available at relatively low temperature levels compared to the other ones (the temperature level increases towards MHE1).

Table 2.15 – Thermal powers available from the methanation unit and SNG inlet and outlet temperatures in the heat exchangers.

	MHE1	**MHE2**	**MHE3**	**MHE4**	**FLASH**
Q (kW)	58.1	9.9	4.8	15.8	59.1
T_{in} (°C)	585	468	409	365	158
T_{out} (°C)	300	350	350	158	25

Thus, considering these temperature levels, the commercial Therminol-VP1, a diathermic oil capable of operating at high temperatures (up to 400 °C), has been chosen as heat transfer fluid for both the proposed heat recovery systems. The oil is

maintained at a pressure of 10 bar to allow its operation at high temperatures while preventing the formation of vapours.

Finally, the plant operation time is listed in Table 2.16.

Table 2.16 – Annual operation time of 1MW PtSNG plant.

Operation time [h]	6047
Full load [h]	2500
Partial load [h]	3547
Standby [h]	2255
Transient [h]	458

2.4.2.2 Thermal energy requirement

The reactors are multitube type and are insulated by means of a microporous material with reinforcing filaments in pyrogenic silica (Steelflex-1100®) with a thermal conductivity at 300 °C of about 0.035 W/m·K and a thickness of 2 cm.

Table 2.17 reports the thermal energy requirement (kWh/h) during the hot-standby and the thermal energy (kWh) required to restart the reactors after the cold-standby. The thermal energy required during the hot-standby has been calculated by assuming a minimum working temperature of 250 °C for each reactor (the minimum temperature for catalysts activation), while the thermal energy required to warm up the reactors after cold-standby, up to the catalysts' activation temperature, has been calculated by assuming 20 °C as the reference ambient temperature.

Table 2.17 – Thermal energy requirements of the methanation unit.

	MHE1	**MHE2**	**MHE3**	**MHE4**	**Total**
Hot-standby [kWh/h]	1.01	0.74	0.74	0.56	3.06
Cold-standby [kWh]	7.78	4.60	3.18	1.94	17.79

By comparing the total energy requirement of the two standby options due to reactors' characteristics, it can be noted that if no heat recovery system is coupled to the plant, hot-standby is cheaper than cold-standby if its duration is less than six consecutive hours. In this case, the energy consumption would be covered by energy coming from outside the plant, representing a cost. Furthermore, hot-standby is preferable to avoid thermal stress and for reasons of flexibility, i.e., for restarting SNG production as soon as conditions return favourable [83]. Moreover, it is clear that the amount of energy that has to be stored in the storage devices (the oil tanks in the case of the thermal storage configuration and the batteries in the case of electrical storage

configuration) depends on the number of hot-standby hours, with the thermal energy (17.79 kWh) required to restart the methanation unit from cold-standby being fixed.

Thus, in order to identify the optimum combination between hot- and cold-standby hours when the plant is coupled with energy recovery systems, statistical analysis on the plant standby hours distribution is carried out in terms of the average duration and frequency. It is worth noting that this analysis is site-specific and closely linked to the typical annual wind energy profile of the considered RES facility, therefore tailor-made considerations would be required for other plants. Figure 2.32 shows the distribution of the standby periods in terms of the duration and frequency in the year.

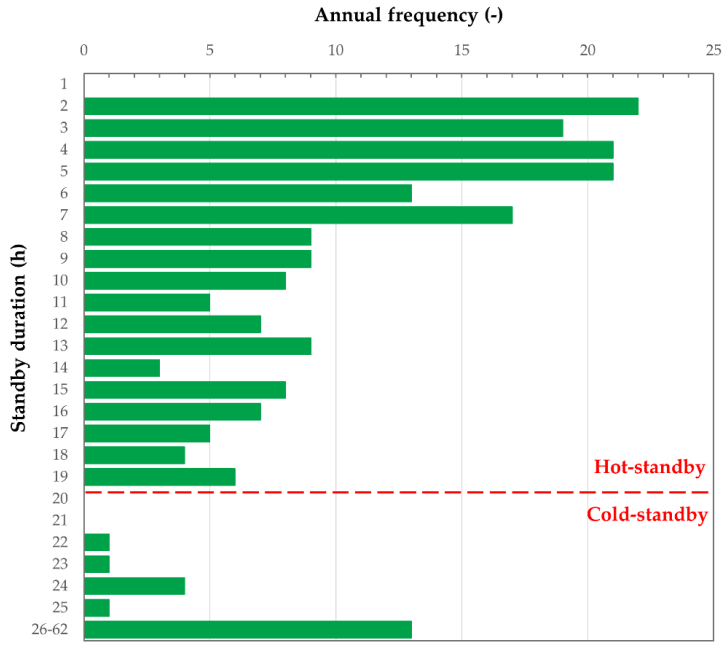

Figure 2.32 – Results of the statistical analysis and distribution of the standby periods.

It can be noted that most of the standby periods have a duration less than 20 h and few occurrences have longer standby durations (the maximum is 62 h). By designing the energy storage in an appropriate way, it is possible to extend the hot-standby duration without requiring any additional external energy. Although extending the hot standby for a greater number of hours results in higher energy consumption, in this case, the latter is covered with recovered waste energy, therefore it does not represent an operational cost. Thus, the duration of the standby periods and their frequency allow one to identify a threshold value for the maximum desirable duration of the hot-standby also useful for storage sizing. Beyond this threshold value, the control strategy switches the operation mode of the methanation unit to cold-standby. In this case,

when the plant is coupled with heat recovery systems, the selected threshold value is 19 h, as reported in Table 6 that summarises the results of the statistical analysis.

Finally, according to the data reported in Table 2.18, the total energy that has to be stored in the storage devices is equal to 75.9 kWh (58.1 kWh to cover the energy consumption of the 19 h hot-standby and 17.8 kWh to cover the energy consumption related to the restart from the cold-standby).

Table 2.18 – Results of the statistical analysis and distribution of the standby periods.

Total number of methanation unit standby hours (h)	2255
Longest standby (h)	62
Total number of standby periods	213
Average annual standby duration (h)	10.6
Threshold value (h)	19
Number of hot-standby	193
Total hours of hot-standby (h)	1521
Number of cold-standby	20
Total hours of cold-standby (h)	734

2.4.2.2.1 Thermal storage results

Results of the thermal storage model show that the hydrogen flow rate needed to maintain the temperature of the methanation reactors at least at the minimum catalysts activation temperature (250 °C) is equal to 6.5 kg/h and its temperature at the inlet of the first reactor (MR1) is equal to 367 °C. The temperature of the hydrogen exiting the last reactor (MR4) is 250 °C (stream 15HR in Figure 2.29). Then, in order to ensure the cyclic operation, the hydrogen is re-heated by the diathermic oil from the hot oil tank (in the heat exchanger HRHE1) up to 367 °C.

With reference to the two-tank oil circuit, the hot oil flow (8HR) is equal to 31.5 kg/h and it is stored at 387 °C. Because the diathermic oil leaves the HRHE1 heat exchanger at 281 °C, it has to be cooled down to the storage temperature of the cold oil tank (30 °C). This cooling heat (from the HRHE2) can be further recovered for external or internal use.

The mass of diathermic oil necessary to store the required thermal energy (75.9 kWh) is equal to 1067.3 kg (the specific heat is 2.416 kJ/kg·K) and the hot oil tank volume results in 1.50 m^3 (the density at 387 °C is 713.2 kg/m^3).

2.4.2.2.2 Electrical storage results

The ORC operating parameters have been chosen in order to maximise the waste heat recovery and the ORC efficiency. These constraints are conflicting. In fact, to maximise the waste heat recovery, a high flow rate of diathermic oil is required due to a large amount of heat available from the flash unit, while a high turbine inlet temperature, necessary for a high ORC efficiency, cannot be reached due to the temperature of the hot oil, which decreases as its flow rate increases.

Therefore, a compromise has been found by assuming an oil flow rate equal to 827 kg/h. The temperature of the hot oil exiting the last heat exchanger is about 300 °C.

Figure 2.33 shows the energy balance of the oil circuit. The total amount of waste heat recovered and supplied to the ORC is therefore equal to 145.2 kW, out of a total of 148 kW that was recoverable from the methanation unit.

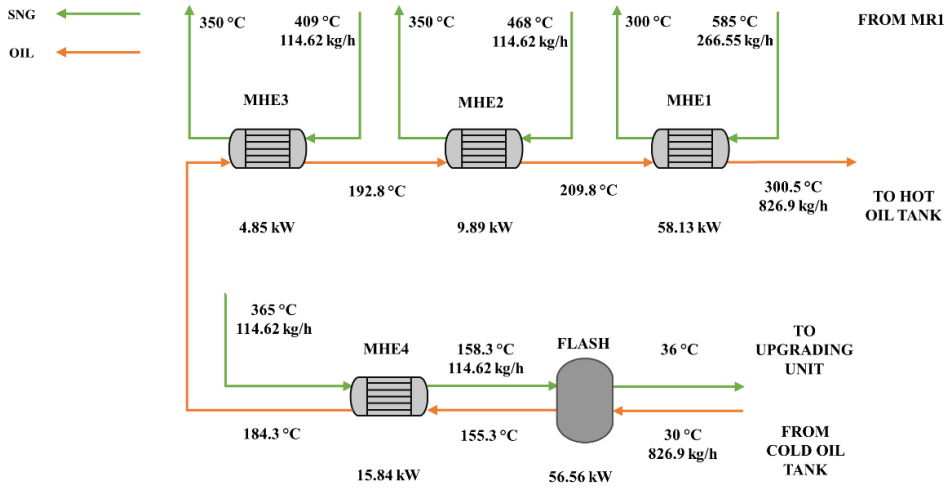

Figure 2.33 – Diathermic oil circuit for waste heat recovery from the methanation unit, sized for coupling with ORC power unit.

With respect to the operating parameters of the ORC cycle, the minimum and maximum pressures and the inlet turbine temperature are set to 3 bar, 30 bar and 183 °C, respectively.

Table 2.19 summarises the main operating conditions and performance of the ORC unit. Detailed results concerning streams' temperatures, pressures and flow rates are also given in Figure 2.34.

Table 2.19 – Operating conditions and performance of ORC unit.

ORC Operating Parameter	
Isobutane flow rate [kg/h]	1200

Condenser pressure [bar]	3
Pressure ratio	10
Turbine inlet temperature [°C]	183
Split to ECO [kg/h]	499.6
Pump efficiency	0.70
Scroll expander efficiency	0.65
ORC Performance	
Compression power [kW]	2.47
Expansion power [kW]	26.57
Net mechanical power [kW]	24.1
Provided heat power [kW]	145.2
Overall ORC efficiency [%]	16.6

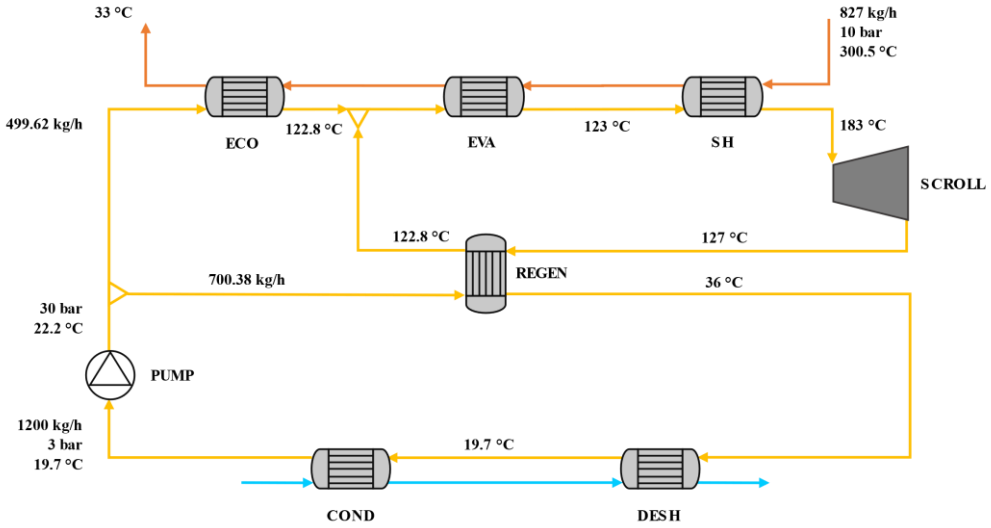

Figure 2.34 – Results for the ORC power unit

Regarding the size of the oil tanks necessary to decouple the heat recovery from the electricity generation allowing more continuous operation of the ORC, the thermal energy stored is 435.6 kWh (3 h of operation in full load). Therefore, 2481 kg of diathermic oil is stored at 300 °C. Since the diathermic oil density at 300 °C is 817 kg/m^3, the volume of the hot oil tank results equal approximately 3 m^3.

Referring to the battery sizing, by assuming an electrical efficiency equal to 0.95, the battery is designed for a capacity of 80 kWh. When the methanation unit is in operation and the ORC produces electrical energy, part of this is used for plant auxiliaries (12.3 kWh at full load operation for 1 h) so that the electrical energy useful

to charge the batteries is equal to 11.8 kWh, resulting in a battery charge time of 6.8 h.

2.4.2.3 Annual performance results

Table 2.20 reports the annual energy balance as well as the annual performances of the PtSNG plant. The annual water, hydrogen and carbon dioxide consumptions are equal to 790 Nm^3, 999,000 Nm^3 and 261,286 Nm^3, respectively. The SNG production is equal to 265,287 Nm^3.

Table 2.20 – Annual mass and energy balance and annual performances.

PtSNG Plant Capacity (Electrical Power Input DC)	1 MW	
Energy [MWh/year]		
Annual electric energy consumption of the electrolysis unit (AC/DC)	5483/5209	
Annual electric energy consumption for compressors and auxiliaries	29.8	
Annual energy consumption for hot-standby	4.7	
Annual energy consumption for cold-standby	0.36	
Annual SNG chemical energy (LHV basis)	2424	
Chemical energy of the remaining hydrogen * (LHV basis)	3.6	
Plant Performances		
Waste Heat recovery configuration	***Thermal storage***	***Electrical storage***
PtSNG Plant annual efficiency, LHV basis [%]	44.0	44.3
PtSNG Plant annual efficiency, HHV basis [%]	48.9	49.2

*The remaining hydrogen in the storage tank is the difference between the annual hydrogen production and the annual hydrogen consumption.

From the data in Table 2.20, it can be noted that the energy consumption for hot and cold standby states (5.06 MWh/year in total) is only a small percentage (0.09%) of the total energy required to operate the plant (electric energy in AC for the electrolyser and that for ancillary equipment).

As regards the annual efficiencies, the PtSNG plant in the base case, without any heat recovery systems, shows efficiencies of 43.9% on an LHV basis and 48.8% on an HHV basis. The results for the thermal storage and electrical storage configurations show that the energy recovery intended to satisfy internal consumption only is beneficial for a PtSNG plant, albeit slightly. Compared to the base case (in which no energy recovery is carried out), the increase in the annual efficiency was proportional to the annual energy savings achieved by the two proposed systems, equal to 5.06 MWh/year and 34.86 MWh/year for the thermal storage and the electrical storage,

respectively. In the base case, it would be reasonable to expect a decrease in the annual efficiency with respect to the nominal efficiency, due to shutdowns and the fluctuating plant behaviour. However, the annual efficiency remains close to the nominal efficiency values in the case in which waste energy is recovered for internal uses. Moreover, the electrical storage configuration shows a slightly higher annual efficiency with respect to the thermal storage configuration because in the first case, the ancillary equipment power consumption is also satisfied by the waste energy recovered. If the surplus electricity produced by the ORC was also valued or sold externally, slightly higher annual efficiencies could be achieved.

A rough discussion on costs is also given. In principle, the proposed energy recovery systems should have very low operating expenditures, linked mainly to their maintenance as they are operated with waste energy, while the capital costs should be carefully evaluated. This will be the subject of future investigation in greater detail. Capital expenditures are expected to be low in the case of thermal storage (purchase of diathermic oil tanks and heat transfer fluid), and higher in the case of electrical storage (higher volumes of diathermic oil, ORC and batteries). However, electrical storage could lead to greater annual savings, avoiding the expense of electricity supplied to ancillary equipment, and providing a faster return on investment. In reality, considering the heat recovery only to satisfy the internal demands of the plant is probably not convenient, but it can become interesting if one considers the possibility of being able to sell all the recoverable waste energy, whether it is heat (for example for district heating) or electricity that can be sold to the grid. Meeting the internal energy demand of the plant with recovered waste energy could also lead to environmental benefits, where previously the additional external energy was provided by the electric grid (affected by the energy mix) or by natural gas.

Finally, it is emphasised that in this work, the heat recovery systems have been designed only to ensure the self-sustenance of the plant regarding the standby periods and ancillary equipment energy requirements. However, the plant internal energy consumption is significantly lower than the waste energy available from the methanation process. A remarkable further improvement of the PtSNG plant performance can be reached if this surplus is employed for external thermal or electrical utilities.

CHAPTER 3. ANALYSIS OF IMPACT OF HYDROGEN INJECTION NATURAL GAS NETWORKS

3.1 Challenges to injecting hydrogen into natural gas networks

In 2020, the European Commission (EC) published the European Union (EU) hydrogen strategy on the roadmap to develop an integrated energy system based on the large-scale hydrogen supply chain [84]. The EU hydrogen strategy has the twofold objective of expanding hydrogen use to replace fossil fuels and to decarbonize its production. In detail, the path set by the EC is divided into three phases. The first phase entails the installation of at least 6 GW of renewable hydrogen electrolysers in the EU by 2024 and producing up to one million tonnes of renewable hydrogen. The second one relies on the installation of at least another 40 GW of renewable hydrogen electrolysers by 2030 and the production of up to 10 million tons of renewable hydrogen in the EU. The third and last phase aims to deploy large scale renewable hydrogen technologies to reach all hard-to-decarbonise sectors by 2050.

To achieve such goals, it will be effective to consider the reuse of the existing natural gas (NG) infrastructure. The latter will play a crucial role in the development of a decarbonized energy system based on a large usage of hydrogen as energy carrier due to its widespread presence and its capacity to provide a cost-effective option for transporting and storing large amounts of energy for long-term periods, exploiting the NG transportation and distribution networks, as well as the storage complexes of the existing NG infrastructure.

On the other hand, as discussed in the previous chapter, the increasing weight of the non-programmable RESs is currently leading to relevant issues on the management of the electricity grid, owing to their intermittent and random nature. The storage capacities required to guarantee the stability and flexibility of the electrical energy

system can be ensured by the application of PtG technologies [2]. In fact, the hydrogen produced from non-programmable RESs during overgeneration periods can be injected into NG pipelines, thus overcoming balancing and regulation issues related to the electricity grid management, as well as decarbonizing end-use sectors (e.g., residential, urban and public transport, industrial). Thus, the blending of hydrogen produced from RESs into NG mixtures nowadays represents an effective tool for developing a climate neutral integrated energy system.

Nevertheless, several factors must be considered to assess the possibility of using mixtures of hydrogen and natural gas (H2NG) into existing network components (e.g., pipelines, valves, compressor, measuring systems). Indeed, increasing content of H_2 lead to significant changes in physical and thermal properties of the flowing gaseous mixture. Methane has greater density, viscosity, calorific value by volume and solubility in water compared to hydrogen; on the contrary, hydrogen has a higher heat capacity, diffusivity, calorific value by mass, maximum flame temperature, autoignition temperature and wider explosive and fire danger. Moreover, hydrogen has a lower density and viscosity than methane and air at normal temperature and pressure [85].

The changes in thermodynamic properties, in turn, result in changes in combustion and calorific properties. Therefore, the addition of hydrogen could originate minor or major issues depending on the volumetric percentage of hydrogen added. Some of the key issues related to blending hydrogen into natural gas pipeline are the: i) durability of the natural gas network components and the integrity of pipelines, ii) impact on the energy capacity of the gas supply system and gaseous leaks, iii) implication on safety of the transmission, distribution and use of the gaseous mixture, iv) impact on end-use appliance and v) effect on measuring systems. In general, only minor criticalities occur with blends of less than 5% – 15% hydrogen by volume, depending on site specific conditions and particular natural gas mixture compositions. Therefore, it is agreed that extensive studies and tests of pipelines, compressor, valves, measuring devices and appliances are needed [86].

In the following paragraphs, an overview on the effect of hydrogen injection in natural gas measurements is presented. After the literature review on analysis of the effects of hydrogen injection on natural gas networks measurement, the effect of hydrogen injection on gas measurements, both from a theoretical and an experimental point of view is analysed as case study. In detail, a comprehensive analysis of the changes of thermo-physical properties when gases with different H_2 content are used has been carried out, as well as of the theoretical effects on the accuracy of volume

conversion at standard conditions. The impact of the hydrogen injection on the accuracy of static ultrasonic domestic gas meters has also been experimentally investigated and the related results have been presented and discussed.

3.2 Literature review on analysis of the effects of injection on natural networks

Several studies have been devoted to the analysis of the effects of H2NG mixtures on the reliability of existing measurement systems. In [87] the changes in the properties of different gas types of the "H" group of EN 437:2019 were investigated, demonstrating all gases remained in group "H" when hydrogen is injected into natural gas with a content ranging from 2% to 23%. In particular, the thermo-physical properties of the mixtures vary as follows: i) the speed of sound increases in the range 1 – 13.5%; ii) the density (relative density) decreases in the range 1.7 – 20.5%; iii) the higher calorific value decreases in the range 1.4 – 16%; iv) the Wobbe index decreases in the range 0.49 – 5.7%. In conclusion, it is affirmed that the injection of more than 10% hydrogen to natural gas allows to manage existing gas transportation and gas consumption systems without the need for reconstructions, modifications, changes in the algorithms for calculating physical parameters of the gas mixture and volumetric flow (volume); on the other hand, further studies and the development of new algorithms are needed for higher hydrogen contents. In [88] no problems were recorded relating to the materials used in the construction of ultrasonic, membrane and turbine gas meters for hydrogen up to 30%. In particular, diaphragm, turbine and ultrasonic gas meters should be insensitive to this effect. However, they encourage field tests to determine the measurement accuracy of gas meters with H2NG mixtures, as well as long-term metrological stability. Iskov [89] analyse the medium-term effects (about one year) of 100% hydrogen on the metrological properties of traditional turbine, rotary piston and diaphragm gas meters at a pressure of 20 mbar, finding that hydrogen had no effect on the metrological characteristics of the gas meters tested, despite some issues with the turbine meter seal. Dehaeseleer [90] demonstrated that there are no operational issues with traditional gas meters (turbine, rotary piston and diaphragm) up to 10% of the hydrogen content in natural gas, however, above this value a new calibration could be necessary, together with the evaluation of changes to the design of the meters. Jaworski [91] experimentally evaluated the durability of diaphragm gas meters with hydrogen, demonstrating they are not significantly affected by injection of hydrogen up to 15%. The long-term drift has also been related to the

wear of the internal parts of the meter, rather than to the hydrogen content in the gas mixture. In addition, no damage was found that could represent a threat to operational safety as all gas meters tested maintained unaltered tightness during and after the test. Jaworski and Dudek [92] found capillary thermal mass gas meters comply with accuracy limits and only occasional values exceed the maximum permissible errors (MPE) for H2NG with 2, 4 and 5% of hydrogen; on the other hand, with hydrogen content of 10 and 15% they significantly exceeded the MPEs with error curves systematically shifted towards negative errors(e.g., up to – 3.4% and – 8.4% of the Weighted Mean Error (WME), at 10% and 15% of H_2, respectively).

No experimental evidences are available in the literature against the injection of H_2 up to 10% for ultrasonic meters, whereas for higher levels further experimental research is required [47]. Finally, as regards the effects on the volume conversion, Łach [93] investigates the effects of H2NG on the calculation of the compressibility factor. To this end, tests were carried out in the laboratory of the Polish National Research Oil and Gas Institute to compare SGERG-88 and AGA8-DC92 methods to determine the compressibility coefficient of gas with an increasing hydrogen content. In fact, both methods have application limitations in terms of hydrogen content in natural gas up to 10% (mol/mol). Research has shown that the AGA8-DC92 method provides satisfactory results when the hydrogen content is less than 40% (mol/mol).

3.3 *Case study #4: Impact of hydrogen injection on natural gas networks measurement*

3.3.1 Theory and methods

3.3.1.1 Thermodynamic properties

The density of the real gaseous mixture at metering reference conditions is obtained using the ISO 6976:2017 [94] formula:

$$D(p,t) = \frac{D^0}{Z(p,t)} \tag{3.1}$$

where : i) $Z(p,t)$ is the compressibility factor of the gaseous mixture calculated conforming to the ISO 6976:2017 standard [94]; ii) D^0 is the density of the ideal gaseous mixture at the metering reference conditions evaluated through the following equation:

$$D^0(p,t) = \frac{M}{V^0} \tag{3.2}$$

where: i) V^0 is the ideal molar volume of the gaseous mixture evaluated according to the ideal gas law; ii) M is the molar mass of the gas mixture calculated from:

$$M = \sum_{j=1}^{N} x_j M_j \tag{3.3}$$

where: i) x_j is the mole fraction of the j-th component in the gas mixture; ii) M_j is the molar mass of the j-th component.

The relative density is defined as the ratio of the density of the gaseous mixture to the density of dry air of reference composition at the same specified conditions of pressure and temperature. It has been calculated in accordance with the ISO 6976:2017 [94] formula for the real gaseous mixture:

$$G(p,t) = \frac{G^0 \cdot Z_{air}(p,t)}{Z(p,t)} \tag{3.4}$$

where: i) $Z_{air}(p,t)$ is the compressibility factor of dry air of reference composition; ii) $Z(p,t)$ is the compressibility factor of the gaseous mixture calculated in accordance with the ISO 6976:2017 [94]; iii) G^0 is the relative density of the ideal gas, which is evaluated through the formula below:

$$G^0 = \sum_{j=1}^{N} x_j \frac{M_j}{M_{air}} \tag{3.5}$$

where: i) x_j is the mole fraction of the j-th component in the gas mixture; ii) M_j is the molar mass of the j-th component; iii) M_{air} is the molar mass of dry air of reference composition.

The specific heat capacity has been estimated employing the correlations depending on the temperature and gaseous mixture composition available in literature. Namely, the specific heat capacity at constant pressure has been evaluated as the weighted average of the specific heat capacities at constant pressure of the components constituting the gaseous mixture:

$$c_p(t_1) = \sum_{j=1}^{N} x_j \cdot c_{p,j} \tag{3.6}$$

where: i) x_j is the mass fraction of the j-th component in the gas mixture; ii) $c_{p,j}$ is the specific heat capacity at constant pressure of the j-th component calculated according to the equation in [95]:

$$c_{p,j}(T) = A_j + B_j\,T + C_j\,T^2 + D_j\,T^3 + E_j\,T^4 \tag{3.7}$$

where i) T is the absolute temperature; ii) A_j, B_j, C_j, D_j, E_j are the regression coefficients for the j-th component of the gaseous mixture, reported in Table 3.1.

Table 3.1 – Regression coefficients for chemical compound [96].

Component, j	Temperature range [K]	A	B	C	D	E
Methane, CH_4	50-1500	34,942	-3,9957E-02	1,9184E-04	-1,5303E-07	3,9321E-11
Ethane, C_2H_6	100-1500	28,146	4,3447E-02	1,8946E-04	-1,9082E-07	5,3349E-11
Propane, C_3H_8	200-1000	31,986	4,27E-02	5,00E-04	-6,56E-07	2,56E-10
n-Butane, n-C_4H_{10}	200-1500	20,056	2,8153E-01	-1,3143E-05	-9,4571E-08	3,4149E-11
iso-Butane, iso-C_4H_{10}	200-1500	6,772	3,1447E-01	-1,0271E-04	-3,6849E-08	2,0429E-11
n-Pentane, n-C_5H_{12}	200-1500	26,671	3,2324E-01	4,2820E-05	-1,6639E-07	5,6036E-11
iso-Pentane, iso-C_5H_{12}	200-1000	16,288	3,1754E-01	2,0237E-04	-4,3027E-07	1,8001E-10
n-Hexane, C_6H_{14}	200-1500	25,924	4,1927E-01	-1,2491E-05	-1,5592E-07	5,8784E-11
Nitrogen, N_2	50-1500	29,342	-3,5395E-03	1,0076E-05	-4,3116E-09	2,5935E-13
Carbon dioxide, CO_2	50-5000	27,437	4,2315E-02	-1,9555E-05	3,9968E-09	-2,9872E-13
Hydrogen, H_2	250-1500	25,399	2,0178E-02	-3,8549E-05	3,1880E-08	-8,7585E-12

The calculation of the higher calorific values $(Hv)_G^0$ on volume basis, at a temperature t, has been carried out basing on the ISO 6976:2017 standard [94] through the following equations:

$$(Hv)_G^0(p,t) = \frac{(Hc)_G^0(t)}{V^0} \tag{3.8}$$

where: i) $(Hc)_G^0(t)$ is the ideal higher molar-basis calorific value; ii) V^0 is the ideal molar volume of the mixture calculated according to the ideal gas law.

The Wobbe Index is defined as the ratio of the higher calorific value, at specified reference condition, to the square root of the relative density. Conforming to the ISO 6976:2017 [94], it has been calculated from the following formula:

$$W_G^0(t,p) = \frac{(Hv)_G^0(t,p)}{\sqrt{G^0}} \tag{3.9}$$

where: i) $(Hv)_G^0$ is the higher calorific value on volume basis of the ideal mixture; ii) G^0 is the relative density the ideal mixture.

The speed of sound in a gaseous flow can be estimated using the AGA 10 formula [97]:

$$u = 18.591 \left(\frac{T \cdot Z \cdot k}{\rho_s} \right)^{0.5} \tag{3.10}$$

where: i) T is the absolute temperature; ii) Z is the compressibility factor of the gaseous mixture calculated employing the ISO 6976:2017 standard [94]; iii) k is the adiabatic coefficient of the gaseous mixture (e.g. the ratio between heat capacities at constant pressure and volume, respectively); iv) ρ_s is the density of the gas mixture at reference conditions.

3.3.1.2 Volume conversion factor

The accurate knowledge of NG volumetric flow rate is crucial in commercial transactions and balancing issues of the NG infrastructures. To this aim, the NG mixture volume measured at operative conditions is commonly converted to the standard reference conditions (i.e., p_S=101.325 kPa, T_S=15 °C). Such volume conversion is obtained through the following equation:

$$V_S = V \cdot KTvo \tag{3.11}$$

where: i) V_S and V are the NG mixture volume at reference and metering conditions, respectively; ii) $KTvo$ is the volumetric correction factor calculated using the formula below:

$$KTvo = \frac{p}{p_S} \cdot \frac{T_S}{T} \cdot \frac{Z_S}{Z} \tag{3.12}$$

where: i) p_S and p are the absolute pressure at reference and metering conditions, respectively; ii) T_S and T are the temperature at reference and metering conditions, respectively; iii) Z_S and Z are the compressibility factor calculated at reference and metering conditions, respectively.

The compressibility factor at reference conditions, Z_S, has been calculated according to the ISO 6976:2017 [94] equation:

$$Z_S = 1 - \left(\frac{p}{p_0} \right) \cdot \left[\sum_{j=1}^{n} x_j \cdot s_j(t,p) \right]^2 \tag{3.13}$$

where: i) $p_0 = 101325$ kPa is the reference pressure and p_2 is the pressure at metering conditions; ii) x_j is the mole fraction of the j-th component in the gas mixture; iii) s_j is the summation factor of the j-th component in the gas mixture, whose values are reported in ISO 6976:2017 [94] at the metering reference temperatures.

The compressibility factor at metering conditions, Z, has been calculated in accordance with the ISO 12213–2:2010 standard [98]. The standard employs the AGA8-DC92 detailed characterization equation, developed by Starling e Savidge in 1992 [99]. This is an extended virial-type formulation, only capable to calculate the properties in the gaseous phase. The input data required to use the AGA8-DC92 equation are the absolute pressure, absolute temperature and the detailed molar composition of gaseous mixture, in which all constituents present in amounts exceeding a mole fraction of 0.00005 should be represented. It may be written as:

$$Z = 1 + B\rho_m - \rho_r \sum_{n=13}^{18} C_n^* + \sum_{n=13}^{58} C_n^* \left(b_n - c_n k_n \rho_r^{k_n}\right) \rho_r^{k_n} \, exp\left(-c_n \rho_r^{k_n}\right) \tag{3.14}$$

where: i) B is the second virial coefficient; ii) ρ_m is the molar density; iii) ρ_r is the reduced density; iv) b_n, c_n, k_n are constants; v) C_n^* are the coefficient which depend on the temperature and NG mixture composition. The reduced density ρ_r is correlated to the molar density ρ_m through the below relation:

$$\rho_r = K^3 \rho_m \tag{3.15}$$

where: i) K is a mixture size coefficient; ii) ρ_m is the molar density calculated using the following equation:

$$\rho_m = \frac{p}{ZRT} \tag{3.16}$$

where: i) p is the absolute pressure; ii) $R$is the universal gas constant; iii) T is the absolute temperature.

Observing the equation (12), it can be pointed out the NG volume at base condition is highly influenced by the compressibility factor. Therefore, the calculation method of compressibility factor is critical in NG industries especially for large flow metering plants [100]. In order to assess its reliability, the calculation of the compressibility factor has been carried out also using the ISO 12213-3, AGA NX 19 and AGA NX 19 Mod. standards, which are still used in NG industries.

3.3.1.3 Ultrasonic static gas meter measuring principles

The ultrasonic gas meters for domestic use determine the volume of the gas flowing through the gas meter measuring the transit times (e.g., Time of flight, TOF) of the ultrasonic waves generated by a pair of piezoelectric transducers operating as transmitter/receiver (see Figure 3.1). The measurement of the transit times (e.g., t_1 and t_2) and the knowledge of geometric characteristics of the measurement tube (e.g., diameter, *D*, propagation angle, φ and distance between the two transducers, *L*) allow to calculate the average velocity ($\overline{w}$) of the gas flow and therefore, the volumetric flow rate (*V*), employing the following equation:

$$\overline{w} = \frac{L}{2\,cos\varphi}\left(\frac{1}{t_1} - \frac{1}{t_2}\right) = \frac{L^2}{2\,D}\cdot\frac{\Delta t}{t_1\,t_2} = \frac{L^2}{2\,D}\cdot\Delta f \tag{3.17}$$

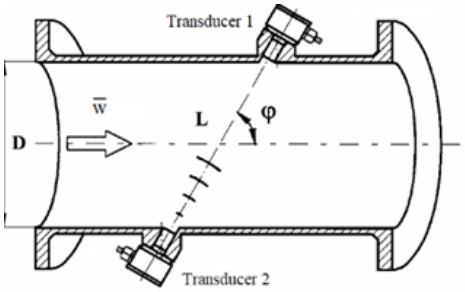

Figure 3.1 – Measurement principle of the ultrasonic gas meters.

Since the sound of speed in the gas flow (c_0) is unknown, depending on the thermodynamic state (e.g., pressure and temperature) and composition of the fluid, the measurement of $\overline{w}$ is performed thorough the measurement of transit times of two different ultrasonic signals. The transit time (t_1) of an ultrasonic signal traveling cocurrent with the gas flow from Transducer 1 to Transducer 2 is measured. After the measurement is completed, the transit time (t_2) of an ultrasonic signal traveling counter current the gas flow from Transducer 2 to Transducer 1 is measured. Specifically, the transit time of the signal cocurrent with the gas flow will be lower than that of the signal counter current with the gas flow owing to the velocity of the gas within the meter. This involves different frequencies of the two train waves.

From the analysis of equation (3.17), it can be deduced that the average velocity ($\overline{w}$), and consequently the volumetric flow rate (*V*), is not theoretically influenced by the thermodynamic conditions and composition of the gas flow. However, if the speed of sound is analysed it can be observed that it is significantly influenced by the H_2 content in the NG mixture.

The effects of gas mixtures of variable compositions (mixtures of natural gas, natural gas with hydrogen additives, and mixtures of synthetic biogas) on the accuracy

of domestic gas meters (e.g., ultrasonic, thermal-mass and turbine) have been investigated at laboratories of the Oil and Gas Institute – National Research Institute. To this aim, a test bench capable of testing the metrological performance of gas meters with natural gas mixtures with different H2 content was designed and built, enabling measurement in the range of 0.016 to 25 m^3/h at low gas pressure (approx. 20 mbar). A wet drum gas meter (for flow-rate range up to 0.4 m^3/h) and a rotary gas meter (in the range from 0.3 to 25 m^3/h) were used as reference gas meters. The measurement uncertainty on the test bench is within 0.3% in the range from 0.6 to 6 m^3/h and within 0.45% below 0.6 m^3/h. The research is underway and will be completed at the end of 2021. Therefore, a detailed description of the measurement stand, test methodology and the obtained test results with discussion will be presented in a separate publication. Only a general outline of the tests and example results for ultrasonic gas meters are presented below. The research program included testing the errors of indications with the use of gas mixtures presented in *Table* 3.2.

Table 3.2 – Characteristics of the gas mixtures used for the metrological tests.

Sample	Gas mixture
Air	Atmospheric air
2E/H0	2E natural gas mixture, without hydrogen
2E/H5	2E natural gas mixture, with 5% hydrogen content (V/V)
2E/H10	2E natural gas mixture, with 10% hydrogen content (V/V)

Domestic G4 thermal and ultrasonic gas meters have been tested at flow rates Q_{min}, $3 \cdot Q_{min}$, $0.1 \cdot Q_{max}$, $0.2 \cdot Q_{max}$, $0.4 \cdot Q_{max}$, $0.7 \cdot Q_{max}$ and Q_{max} (three repetitions), whereas an industrial turbine gas meter was tested at flow rates of 5, 8, 10, 16, 20, 25 m^3/h (three repetitions).

3.3.2 Results and discussion

3.3.2.1 Impact of H_2 injection on the thermodynamic properties

In order to analyse the impacts of hydrogen injection in NG mixtures on the above mentioned thermodynamic properties, the 5 NG mixtures (i.e., the ones without presence of H_2) used as example calculations in Annex C of ISO 12213–2:2010 standard [98], as described in Table 3.3, have been investigated.

2189 *Table 3.3 – Molar composition of the investigated gas mixtures [98].*

Component, j	GAS 1	GAS 2	GAS 3	GAS 5	GAS 6
Methane, CH_4	96.50	90.70	85.90	81.20	82.60
Ethane, C_2H_6	1.80	4.50	8.50	4.30	3.50
Propane, C_3H_8	0.45	0.84	2.30	0.90	0.75
n-Butane, n-C_4H_{10}	0.10	0.15	0.35	0.15	0.12
iso-Butane, iso-C_4H_{10}	0.10	0.10	0.35	0.15	0.12
n-Pentane, n-C_5H_{12}	0.03	0.04	0.05	0.00	0.04
iso-Pentane, iso-C_5H_{12}	0.05	0.03	0.05	0.00	0.04
n-Hexane, C_6H_{14}	0.07	0.04	0.00	0.00	0.02
Nitrogen, N_2	0.30	3.10	1.00	5.70	11.70
Carbon dioxide, CO_2	0.60	0.50	1.50	7.60	1.10

2190 The obtained results have been graphically represented in Figure 3.2. The dashed
2191 lines, where present, show the allowable limit in accordance with the main current
2192 applicable standards and national regulations (e.g., relative density and higher heating
2193 value [15], Wobbe Index [16]).

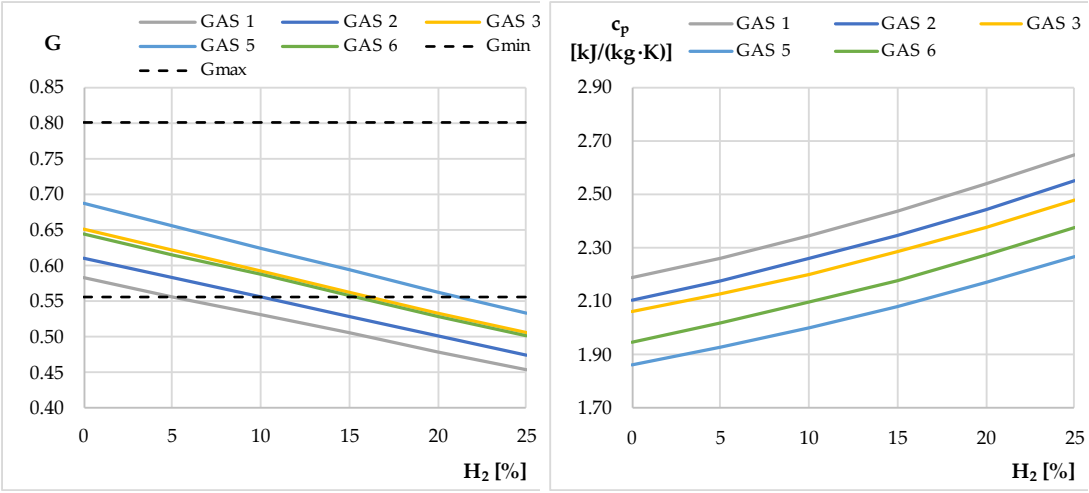

a) **b)**

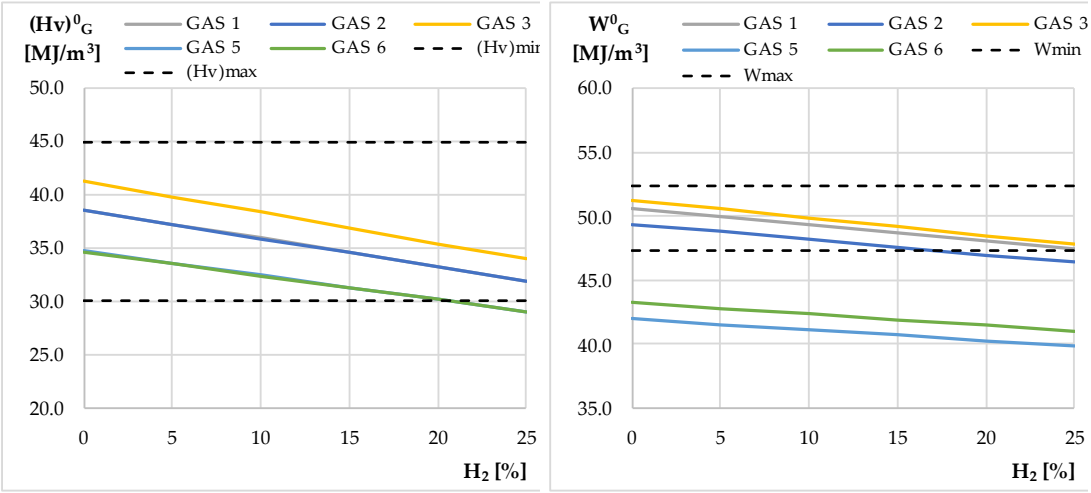

c) **d)**

Figure 3.2 – Trend of the thermophysical properties as a function of the H_2 content in NG mixtures: a) relative density, b) specific heat capacity, c) higher calorific value, d) Wobbe Index.

In Figure 3.3, the trend of the sound speed as a function of the H2 content for the 5 NG mixture reported in Table 1 has been depicted.

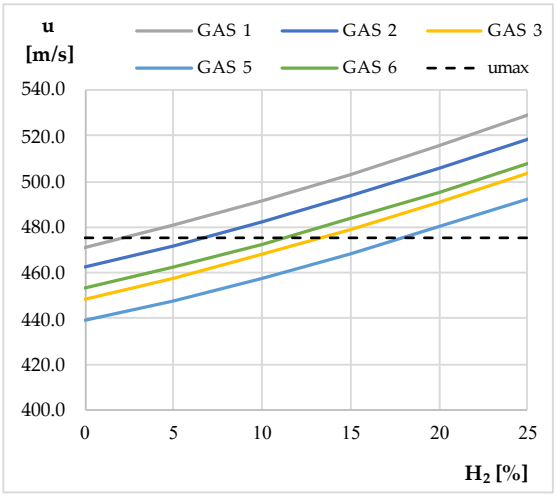

Figure 3.3 – Trend of the sound speed as a function of the H_2 content in NG mixtures.

From Figure 3.3 it can be pointed out the speed of sound increases as H_2 concentration in the NG mixture increases and it becomes tendentially higher than the allowable limit of 475 $m \cdot s^{-1}$ (dashed line) of ISO 14236:2010 [101] for household ultrasonic gas meters even at low H_2 contents.

Hence, even though the measurement of the gas flow velocity is not theoretically influenced by the speed of sound, since this is intrinsically compensated by the sing-

around technique and mediated in the cross section (no effect in the transition of the flow from laminar to turbulent), the change of transit times measured in favor and against flow can lead to unpredictable deviations and a drift in the accuracy of the gas meters.

From the analysis of the obtained results, it can be highlighted that:

iv. the relative density decreases as the H_2 content increases in the NG mixture leading to values below the corresponding limit of ISO 12213–2 standard [98] at about 10% of H_2;

v. the specific heat capacity at constant pressure significantly increases as the H_2 content increases (e.g., up to + 21.8% at about 25% of H_2 for Gas 6);

vi. the higher calorific value on volume basis notably decreases as the H_2 content increases (e.g., up to – 17.8% for Gas 3 at x_{H2}=25%) and for investigated Gas 5 and 6, it reduces to below the corresponding limit indicated by the ISO 12213–2 standard [98] at about 25% of H_2;

vii. the Wobbe Index slightly decreases as the H_2 content increases (e.g., up to – 6.6% at x_{H2}=25% for Gas 2);

viii. the speed of sound increases as the H_2 content increases.

3.3.2.2 Impact of H_2 injection on the volume conversion factor

In order to evaluate the effects of injection of H_2 in NG mixtures on the accuracy of the volume conversion at standard conditions, a typical NG mixture distributed in Italy has been investigated (see Table 3.4).

Table 3.4 – Molar composition of the investigated gas mixture.

Component, j	MIX 1
Methane, CH_4	95.99
Ethane, C_2H_6	2.292
Propane, C_3H_8	0.639
n-Butane, n-C_4H_{10}	0.097
iso-Butane, iso-C_4H_{10}	0.102
n-Pentane, n-C_5H_{12}	0.012
iso-Pentane, iso-C_5H_{12}	0.018
n-Hexane, C_6H_{14}	0.012
Nitrogen, N_2	0.650
Carbon dioxide, CO_2	0.188

Figure 3.4 depicts the effects of the increase of H_2 content up to 25% in the investigated NG mixture on the compressibility factor calculated employing the aforementioned standards. Moreover, to investigate the influence of the metering pressure, the compressibility factor calculation has been performed at different gas pressures fixing a constant value of the gas temperature (i.e., T=15 °C).

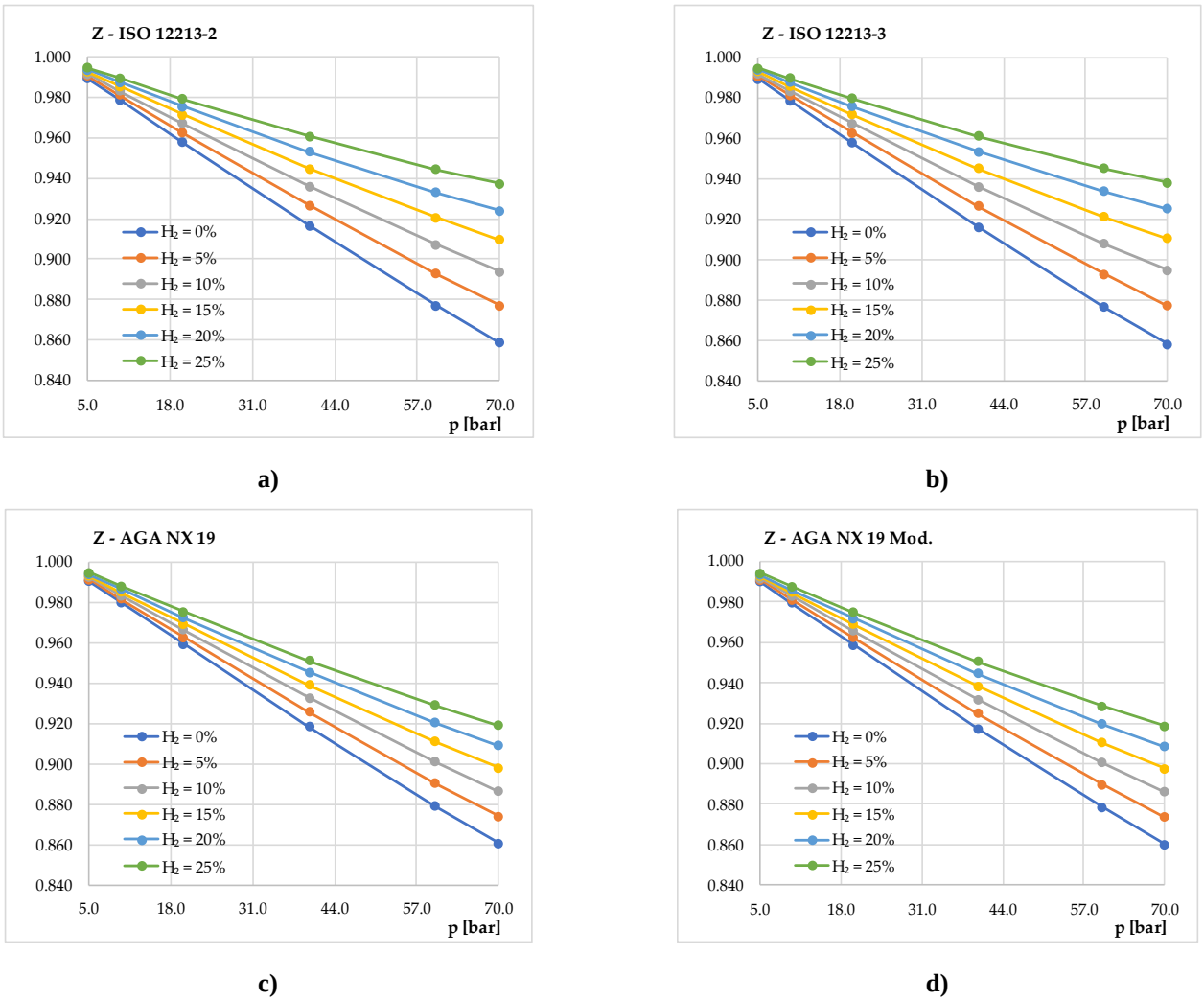

Figure 3.4 – Trend of the compressibility factor as a function of the H_2 content in NG mixtures: a) ISO 12213–2, b) ISO 12213–3, c) AGA NX 19 and d) AGA NX 19 Mod.

From the obtained results, it can be observed that the compressibility factor increases as the H_2 content increases. The compressibility factor is more influenced by the H_2 concentration at high pressures than at low pressures: for instance, using the ISO 12213–2 standard [98] an increasing in the range 0.10 – 0.44% at 5 bar and 2.1 – 9.1% at 70 bar has been found. Moreover, the results show that pressure more significantly affects the compressibility factor at low H_2 concentrations. Finally, as

expected, the compressibility factor decreases as pressure increases. As for example, a decrease of Z has been found in the range 0.25 – 14% at x_{H2} =0%, whereas a lower decrease in the range 0.05 – 0.2% at x_{H2}=25% occurs.

In Table 3.5, the compressibility factor values and the corresponding deviations between the ISO 12213–2 standard and the other standards on varying the H_2 concentration and pressure have been reported. From data in Table 5 it can be observed that ISO 12213–2 and ISO 12213–3 methods lead to deviations within 0.09%, whereas the use of AGA NX 19 and AGA NX 19 Mod. methods can lead to deviations up to about 2% at high pressure and high H_2 content.

Table 3.5 – Compressibility factor values evaluated employing the ISO 12213-2, ISO 12213-3, AGA NX 19 and AGA NX 19 Mod.

p [bar]	H_2 [%]	$Z_{ISO12213-2}$	$Z_{ISO12213-3}$	$Z_{AGANX19}$	$Z_{AGANX19Mod}$	$\Delta Z_{ISO2-ISO3}$	$\Delta Z_{ISO2-AGA19}$	$\Delta Z_{ISO2-AGA19Mod.}$
5.00	0.00	0.98940	0.99026	0.99026	0.98997	0.09%	0.09%	0.06%
	0.50	0.99056	0.99118	0.99118	0.99090	0.06%	0.06%	0.03%
	10.00	0.99167	0.99206	0.99206	0.99179	0.04%	0.04%	0.01%
	15.00	0.99273	0.99290	0.99290	0.99262	0.02%	0.02%	0.01%
	20.00	0.99374	0.99369	0.99369	0.99342	0.00%	0.00%	0.03%
	25.00	0.99469	0.99445	0.99445	0.99417	0.02%	0.02%	0.05%
10.00	0.00	0.97881	0.97868	0.97974	0.97943	0.01%	0.09%	0.06%
	0.50	0.98117	0.98108	0.98154	0.98124	0.01%	0.04%	0.01%
	10.00	0.98341	0.98337	0.98326	0.98296	0.00%	0.02%	0.05%
	15.00	0.98555	0.98553	0.98489	0.98460	0.00%	0.07%	0.10%
	20.00	0.98757	0.98756	0.98643	0.98614	0.00%	0.12%	0.14%
	25.00	0.98949	0.98948	0.98789	0.98760	0.00%	0.16%	0.19%
20.00	0.00	0.95774	0.95748	0.95906	0.95871	0.03%	0.14%	0.10%
	0.50	0.96256	0.96243	0.96266	0.96232	0.01%	0.01%	0.03%
	10.00	0.96713	0.96709	0.96607	0.96574	0.00%	0.11%	0.14%
	15.00	0.97146	0.97147	0.96930	0.96897	0.00%	0.22%	0.26%
	20.00	0.97555	0.97558	0.97234	0.97202	0.00%	0.33%	0.36%
	25.00	0.97941	0.97944	0.97522	0.97491	0.00%	0.43%	0.46%
40.00	0.00	0.91635	0.91588	0.91803	0.91734	0.05%	0.18%	0.11%
	0.50	0.92642	0.92629	0.92545	0.92480	0.01%	0.11%	0.17%
	10.00	0.93586	0.93595	0.93242	0.93182	0.01%	0.37%	0.43%
	15.00	0.94471	0.94492	0.93898	0.93841	0.02%	0.61%	0.67%
	20.00	0.95300	0.95324	0.94515	0.94461	0.02%	0.82%	0.88%

	25.00	0.96076	0.96094	0.95094	0.95044	0.02%	1.02%	1.07%
60.00	0.00	0.87694	0.87628	0.87880	0.87825	0.07%	0.21%	0.15%
	0.50	0.89254	0.89255	0.89020	0.88968	0.00%	0.26%	0.32%
	10.00	0.90700	0.90741	0.90085	0.90036	0.04%	0.68%	0.73%
	15.00	0.92043	0.92101	0.91080	0.91033	0.06%	1.05%	1.10%
	20.00	0.93290	0.93349	0.92011	0.91966	0.06%	1.37%	1.42%
	25.00	0.94448	0.94493	0.92881	0.92839	0.05%	1.66%	1.70%
70.00	0.00	0.85843	0.85769	0.86052	0.85992	0.09%	0.24%	0.17%
	0.50	0.87682	0.87695	0.87387	0.87331	0.02%	0.34%	0.40%
	10.00	0.89378	0.89441	0.88631	0.88578	0.07%	0.84%	0.89%
	15.00	0.90945	0.91028	0.89791	0.89742	0.09%	1.27%	1.32%
	20.00	0.92394	0.92475	0.90874	0.90827	0.09%	1.65%	1.70%
	25.00	0.93736	0.93797	0.91883	0.91839	0.07%	1.98%	2.02%

Finally, the author investigated the effects of H_2 injection on the volumetric correction factor, $KTvo$. From Figure 5, it can be observed that the volumetric correction factor decreases as the H_2 content increases, regardless the calculation algorithm used. Similarly to the compressibility factor, the H_2 content affects $KTvo$ more at high pressures than at low pressures. As for example, the $KTvo$ calculated with the ISO 12213–2 standard decreases as H_2 increase in the range 0.10 – 0.43% at 5 bar, whereas it increases in the range 2.1 – 8.3% at 70 bar.

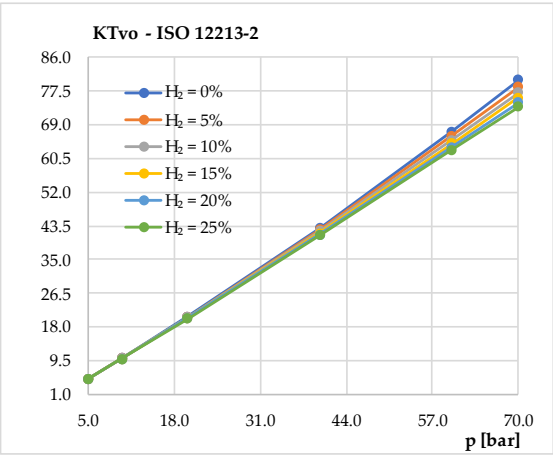

a)

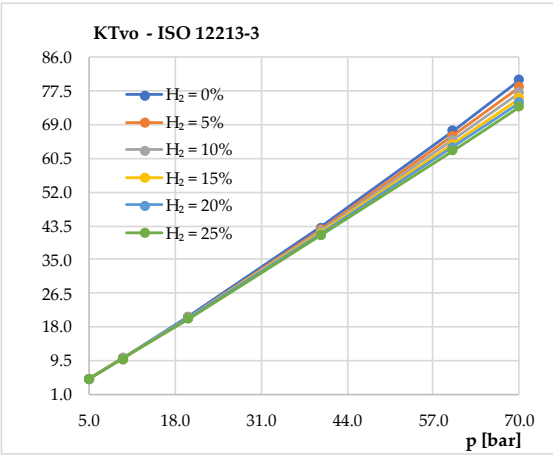

b)

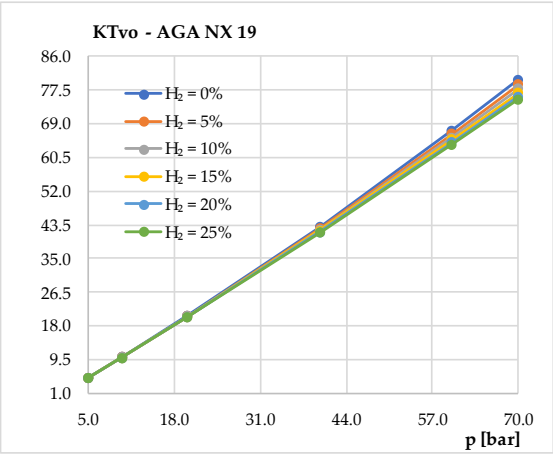

c)

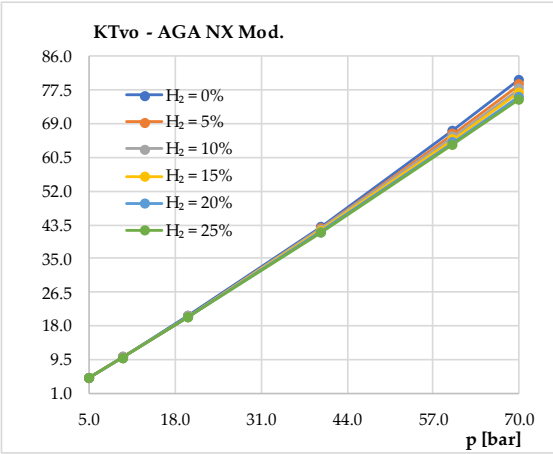

d)

Figure 3.5 – Trend of the volumetric correction factor as a function of the H2 content in NG mixtures: a) ISO 12213–2, b) ISO 12213–3, c) AGA NX 19 and d) AGA NX 19 Mod.

3.3.2.3 Impact of H_2 injection on the ultrasonic domestic gas meters

Domestic ultrasonic gas meters manufactured in 2021, with a measuring range of 0.04 to 6 m^3/h, were subjected to metrological tests with the use of various gas mixtures. Metrological tests were carried out according to par. 5.3.2 of EN 14236:2018, at selected flow rates (Q_{min}, $3 \cdot Q_{min}$, $0.1 \cdot Q_{max}$, $0.2 \cdot Q_{max}$, $0.4 \cdot Q_{max}$, $0.7 \cdot Q_{max}$, Q_{max}), each repeated three times. The gas mixtures listed in Table 2 have been used. Experimental test results are presented in Table 3.6 and Figure 3.6.

The average errors of indication of ultrasonic gas meters, the differences between the errors of indication obtained for reference natural gas and individual gas mixtures, and the metrological analysis of the obtained test results are presented below. For the metrological assessment, average error values were used, while, when analysing the maximum and minimum error values, the values obtained for each gas meter were used individually. In order to define the metrological criterion necessary to assess the impact of H_2 injection on the gas meter errors of indications (metrologically significant or metrologically insignificant), the measurement uncertainty at single flow rates was estimated. As the assessment covers the difference in the average errors of indications for individual mixtures in relation to the errors of indications obtained for the reference mixture of natural gas without hydrogen addition (e.g., between 2E/H0 and 2E/H5), the measurement uncertainty is the total uncertainty in determining the errors in gas meter readings for the gas reference 2E/H0 and the tested mixture with the addition of

hydrogen or biogas (e.g., 2E/H5, 2E/H10). The uncertainty of the average errors of indications, $U(E_m)$, includes the type B uncertainty of the measuring equipment and the type A uncertainty (i.e., the standard deviation of the results of the three tested gas meters). The maximum allowable difference in errors $U(E_{mH\text{-}m2E})$ is obtained by the square sum $U(E_m)$ of the two mixtures; thus, the metrological assessment means "insignificant" if the difference in average errors is below the permitted errors difference.

In addition, the weighted mean errors (WME) was also evaluated according to par. 3.2.5 OIML R 137 1 & 2:2012 [102], according to which the WME for class 1.5 gas meters should be within ±0.6%. Table 3.6 shows the average errors of indications (E_{mAIR}, $E_{m2E/H0}$, $E_{m2E/H5}$, $E_{m2E/H10}$) obtained for individual gas mixtures, average differences ($\Delta E_{2E/H5}$, $\Delta E_{2E/H10}$) between the errors obtained for natural gas ($E_{m2E/H0}$) and individual gas mixtures ($E_{m2E/H5}$, $E_{m2E/H10}$), and weighted mean errors WMEs together with WMEs drift for G4 ultrasonic gas meters.

Table 3.6 – Average errors and average errors of indication drifts as well as WMEs and WMEs drifts of G4 ultrasonic gas meters tested with different gas mixtures.

	Flow Rate							
	Q_{min}	$3{\cdot}Q_{min}$	$0.1{\cdot}Q_{max}$	$0.2{\cdot}Q_{max}$	$0.4{\cdot}Q_{max}$	$0.7{\cdot}Q_{max}$	Q_{max}	
	Average error E_m [%]							*WME* [%]
E_{mAir}	−0.63	−0.99	−0.66	−0.44	−0.40	−0.11	−0.33	−0.30
$E_{m2E/H0}$	−0.81	−1.14	−0.32	−0.25	0.08	0.32	−0.06	0.07
$E_{m2E/H5}$	−0.10	−0.25	0.03	−0.26	−0.13	0.03	−0.49	−0.15
$E_{m2E/H10}$	−0.47	−0.65	0.14	−0.25	−0.28	−0.11	−0.53	−0.25
	Average error drift ΔE_m [%]							*WME* drift [%]
$\Delta E_{m2E/H5}$	0.71	0.88	0.35	−0.01	−0.21	−0.29	−0.43	−0.22
$\Delta E_{m2E/H10}$	0.34	0.48	0.46	0.00	−0.36	−0.43	−0.47	−0.31

Figure 3.6 shows the average errors of indications of G4 ultrasonic gas meters obtained for the gas mixtures 2E/H0, 2E/H5, 2E/H10.

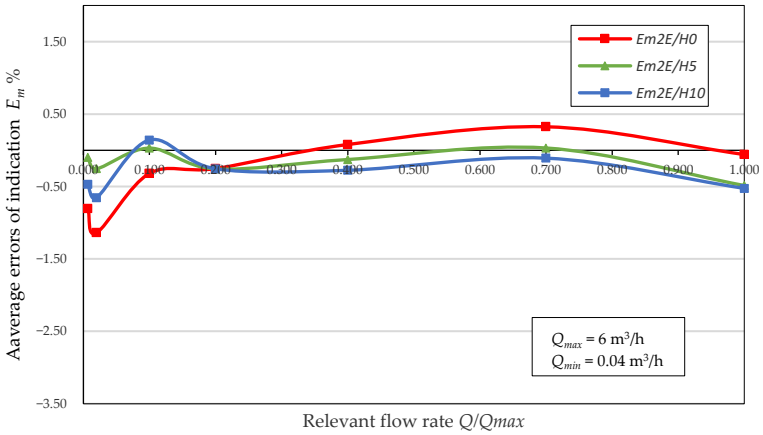

Figure 3.6 – Average errors of indications of G4 ultrasonic gas meters tested with different gas mixtures as a function of relative flow rates Q/Qmax.

The error of indication of the investigated ultrasonic gas meters with 2E/H0 natural gas mixture (i.e., without hydrogen) ranges −0.58% to 0.41% above 0.1·Q_{max} and −0.65% to −0.19% below 0.1 Q_{max}. On the other hand, error of indication with 2E/H5 mixture ranges −0.68% to 0.26% above 0.1·Q_{max}, and 0.07% to 0.70% below 0.1·Q_{max}. The errors of indications of all gas meters with both the 2E/H0 and 2E/H5 mixtures, were within the permissible limits (i.e., ±2% in the range from 0.1·Q_{max} to Q_{max} and ±3.5% in the range below 0.1·Q_{max}) of EN 14236:2018 [23] for ultrasonic gas meters with temperature conversion. The maximum WME of the investigated gas meters was found: (i) ranging 0.01 % to 0.12 % for 2E/H0, (ii) ranging −0.22% to 0.00% for 2E/H5, and (iii) ranging −0.38 % to −0.10 % for 2E/H10 mixture. Table 3.7 shows the average error of indication drifts ($\Delta E_{2E\text{-}2E/H5}$) between 2E/H5 and 2E/H0 mixtures, together with the related metrological assessment.

Table 3.7 – Metrological assessment of average error of indication drift of ultrasonic G4 gas meters with 2E/H5 and 2E/H0.

Flow Rate	Average Errors Drift [%]	Uncertainty in Average Errors [%]		Permitted Errors Difference [%]	Metrological Assessment
	$\Delta E_{m(2E\text{-}2E/H5)}$	$U(E_m)$		$U(\Delta E_{2E\text{-}2E/H5})$	
		2E/H5	2E		
Q_{max}	−0.43	0.17	0.16	±0.46	Insignificant
0.7·Q_{max}	−0.29	0.15	0.15	±0.42	Insignificant
0.4·Q_{max}	−0.21	0.17	0.22	±0.55	Insignificant
0.2·Q_{max}	−0.01	0.24	0.27	±0.72	Insignificant
0.1·Q_{max}	0.35	0.21	0.14	±0.50	Insignificant

$3 \cdot Q_{min}$	0.88	0.20	0.18	±0.53	Significant
Q_{min}	0.71	0.28	0.24	±0.72	Insignificant

In this case, the metrological assessment was found significant only at 3 Q_{min} flow rate, meaning that there is a slight influence on the gas meter accuracy when a 5% H2NG mixture is used. On the other hand, when analysing the errors of indications, it should be noted that hydrogen injection up to 10%vol does not significantly affect the accuracy of gas meters.

3.3.3 Quality measurements of NH2NG mixtures

At present, typical process chromatographs dedicated to natural gas analyses do not allow the in-line determination of the hydrogen content. This is due to the fact that currently used process chromatographs (PGCs) use helium as a carrier gas, so they are not capable to detect and determine hydrogen due to the similar thermal conductivity of both these gases (151 and 180 $Wm^{-1}K^{-1}$ for helium and hydrogen, respectively). Therefore, solutions that can be used to analyse natural gas-hydrogen mixtures should be sought in devices dedicated to other types of gaseous fuels or constructed on the basis of customer guidelines. Aiming at analysing the composition of natural gas-hydrogen mixtures (hydrogen content up to 37% mol/mol), inter alia, a four-channel chromatograph equipped with four TCD detectors, can be used [103–105]. This device uses two carrier gases (argon and helium) and the declared duration of the analytical cycle for a configuration that allows determination of all required components is 3 to 5 min. A frequent calibration of this chromatograph is recommended ranging from daily to every 3 months.

On the other hand, in the refinery sector, a first solution relies on three-channel analysers that enable the determination of components in the gas such as hydrogen, helium, nitrogen, oxygen, carbon monoxide (II), carbon monoxide (IV) and hydrocarbons from the C1–C5 range, including unsaturated hydrocarbons broken down into isomers, and the total content of C6+ hydrocarbons [106,107]. These analysers are equipped with thermal conductivity detectors (TCD) and a flame ionization detector (FID), which is the third measurement channel enabling the determination of the content of hydrogen and other basic components of natural gas-hydrogen mixtures up to 100%. The typical time of analysis with their use is 15 min; however, it requires additional technical gases supplying the FID detector to the chromatograph, i.e., hydrogen and synthetic air as well as helium and nitrogen, which are reference gases in TCD detectors, which increases the cost of operating the device.

Additionally, it is possible to reduce the analysis time to 7.5 min, if hydrogen is used as the carrier gas, then the hydrogen content in the sample is determined by using a TCD detector with nitrogen as the reference gas. However, due to the explosive properties of hydrogen, its use as a carrier gas in gas chromatography is often rejected by laboratories. Single (double) channel chromatograph with a single (double) thermal conductivity detector (TCD) are also available [108,109], enabling in the scope of such components as pseudo-component C6+, hydrogen, helium, oxygen, carbon monoxide (IV), methane, ethane, propane, butanes, pentanes (with the double-channel configuration even nitrogen can be detected). Optionally the chromatograph can be equipped with an additional third channel with a flame ionization detector (FID), allowing individual determination of C6–C16 hydrocarbons. A further chromatograph dedicated to natural gas analyses enables the determination of the content of C1–C9 hydrocarbons, oxygen, nitrogen, carbon monoxide (IV), helium and hydrogen sulphide in the gas [110]. However, no detailed information on the range of the analysed concentrations and the duration of the analysis is available. An important feature of gas chromatographs dedicated to refinery gas analysis is that they allow the determination of hydrogen content in the entire concentration range by using two TCD detectors and an FID detector [111]. Depending on the model, the analysis time ranges from less than 9 min to 17 min.

Chromatographs for both H2NG mixtures and for refinery gas analyses are also available in the market [112,113]. Although chromatographs dedicated to refinery gas analyses are characterized by a sufficiently wide analytical range for hydrogen determination; however, due to the possibility of methane analysis only up to 80% mol/mol, they cannot be used in the case of analyses of certain mixtures of natural gas with hydrogen and natural gas from the H group. On the other hand, chromatographs dedicated to natural gas analyses allow for analysis in the scope of determination of at least: He, O_2, N_2, CH_4, CO, CO_2, C2–C5 hydrocarbons, H_2S and of course H_2 up to 10%. The analysis time depends on the model and ranges from 10 to 40 min. These chromatographs are equipped with two TCD detectors or two TCD detectors and a FID detector.

CHAPTER 4. ANALYSIS OF RELIABILITY OF THERMODYNAMIC EQUILIBRIUM GASIFICATION MODELS

4.1 Biomass gasification process overview

Biomass gasification as a conversion technology is becoming increasingly important on account of renewability and environmental benefits, as well as sociopolitical benefits [114]. Biomass gasification is expected to play a crucial role in supplying the energy demand in many countries and being one of the economically attractive technology for the production of clean energy.

Gasification is a thermochemical conversion process of carbonaceous combustible through the controlled delivery of an oxidizing agent (e.g., air, vapor, oxygen, or carbon dioxide). This process occurs under sub-stoichiometric conditions of the oxidant, in a high temperature and low oxygen content environment. The oxygen amount supplied is limited to avoid complete combustion so that the energy is not converted all into heat, but also into chemical energy in form of a gaseous fuel known as syngas or producer gas. The latter is mainly composed of CO, H_2, CO_2, N_2, methane CH_4, tar and ash [115]. The physical and chemical properties of the syngas, such as its chemical composition, heating value and temperature, vary as a function of the biomass properties, the gasification agent (e.g., type, flow rate, temperature, etc.), the operating conditions (e.g., temperature and pressure), the heating rate and the type of gasifier used [116]. A conventional gasification process follows several successive steps: i) drying, ii) pyrolysis, iii) partial combustion of gases, vapours and char, and iv) reduction of the combustion products. The drying zone constitutes the region where the raw biomass is dried vaporizing its moisture content that contributes to lower quality syngas. In that zone, the temperature typically reaches around 100 °C and no thermal decomposition has still started at this stage [115,117,118]. In the pyrolysis zone, the thermal composition of biomass feedstock takes place in absence of oxygen or air within a temperature range of 125 °C to 500 °C. At this stage, the feedstock is

decomposed into charcoal, liquid tars and a mixture of gases containing carbon monoxide, hydrogen, carbon dioxide and hydrocarbons. The oxidation zone concerns the region where the volatile materials generate mainly CO, CO_2 and H_2O through a series of exothermic reactions, under temperatures that may vary from 1000 °C to 1500 °C. At the last stage, the reduction of the tar particles occurs at temperatures around 1000 °C, while endothermic reactions take place generating combustible products such as CO, H_2, and CH_4. Such stage is crucial for syngas quality since the presence of tar particles reduce the biomass conversion efficiency, in addition to being a severe potential of clogging fuel lines, filters and engine.

The major advantage of the gasification process is that it lets convert waste biomass and other similar biodegradable wastes, which would otherwise have been discarded and unused, into valuable fuel. The synthesis gas produced through biomass gasification is suitable for multiple applications as it can be i) burned at higher temperatures, (ii) employed in fuel cells, (iii) employed to produce methanol and hydrogen and (iv) converted via the Fischer-Tropsch process into a range of synthesis liquid fuels suitable for use gasoline engines or diesel engines [119]. The by-products (e.g., biochar, tar) derived from the gasification process can also be used in multiple ways. Such as biochar can be employed as fertilizer in agriculture, filter absorber in industry or energy carrier [120] and recently, some researchers have investigated the feasibility of using biochar as carbon sequestering additive in cement mortar [121]. Furthermore, the gasification process allows to use as feedstocks a variety of biomass resources, including wood material, pulp and paper industry residues, agricultural residues, organic municipal material, sewage, manure and food processing by-products. A great number of agricultural cultivation residues such as straws, nutshells, fruit shells, fruit seeds, plant stalks and stover, green leaves and molasses are globally produced each year [122]. For example, 89.5 million tonnes of rapeseed have been cultivated worldwide in 2017 [123]. Rapeseed plantations entail the production of a large quantity of straw that needs to be disposed of and since the disposal by open field burning causes air pollution, the use of a gasification technology can have a scarce environmental impact and smaller consequences on the environment than landfill operations or combustion of the waste. For these reasons, in the last decades, gasification has been reputed a valuable solution also for disposal of refuse-derived fuel from municipal solid waste, especially in the developing countries [124].

The thermochemical conversion process of gasification is a mature, reliable and flexible technology, well known and it has been described extensively in literature [115,125–127]. Even though biomass gasification is a mature technology, some

technological barriers limit its large-scale commercial development. In particular, it has been observed that the main constraints in the implementation of biomass gasification are represented by: i) the variability of biomass feedstock physical properties, which requires a high flexibility of the gasifier, ii) the high moisture content of biomass since it decreases the energetic efficiency of the process, iii) the production of ash during the process as it can cause air pollution, iv) the presence of tar in the end products due to its tendency of causing fouling and plugging of the plant pipes and v) the handling and management of biomass feedstock [118].

In order to overcome some of the aforementioned technological barriers, a deep understanding of the different phenomena and operational parameters involved in the gasification process is required. To this aim, a mathematical modelling is a useful tool to understand the physical and chemical mechanisms that occur inside the gasifier. A numerical model allows to evaluate process performance on varying the biomass proprieties and operating parameters, providing a set of optimum operating conditions and designating the risks and limits of the system. Besides, a numerical model helps to reduce considerably the costs of research and development of new and innovative devices [128].

In following paragraphs, a comprehensive analysis of the thermodynamic equilibrium gasification models is presented. Especially, the reliability of the equilibrium models for the simulation of the gasification process as a function of the biomass properties and the operating conditions is assessed. This study aims to better understand in which conditions of practical interest such models can be applied with acceptable reliability, even neglecting tar and char formation to minimise model complexity. Indeed, in case of the analysis of complex energy systems as polygenerative plants a simple and flexible model can represent an easily usable tool for the evaluation of the optimal process parameters. To this aim, a thermodynamic equilibrium model implemented in a non-commercial script is proposed as case study. The developed model has been applied to a large number of experimental case studies available in the scientific literature, assessing thermodynamic equilibrium models performance as for gasification different biomasses and in different operating conditions.

4.2 Biomass gasification modelling

Mathematical models for the biomass gasification process can be categorized into: i) thermodynamic equilibrium models, ii) kinetic rate models, iii) computational fluid dynamics models (CFD) and iv) artificial neural networks (ANNs) models.

Thermodynamic equilibrium models are based on the assumption that the system of chemical reactions involved in the process reaches the state of thermochemical equilibrium inside the gasifier reactor [126,129]. Equilibrium models are able to predict the producer gas composition, the maximum yield and, the optimal conditions of energy efficiency and syngas heating value for the operation of each specific reactor according to biomass feedstock proprieties [115,125–127]. This approach does not require details of system geometry or estimation of the necessary time to reach the equilibrium [130].

Kinetic models are based on the mathematical description of the reaction kinetics of the main reactions and the hydrodynamic phenomena among phases that occur inside the gasification reactor [126,127]. Such models are able to predict the trend and composition of the product in different positions along a reactor, as well as the overall gasifier performance as a function of operating conditions and configuration of the gasifier [127,131]. Therefore, they constitute a useful approach to study gasification, especially for the design and optimization of gasifiers [125,126]. Application of kinetic models involves the knowledge of reaction rate, residence time, reactor hydrodynamics (e.g., superficial velocity, diffusion rate) and gasifier geometry. The key issues with kinetic modelling are the associated high cost for computation and the use of parameters that make them difficult to apply to different plants [126,132]. Indeed, kinetics modelling is quite complicated and requires several assumptions that have yet to be validated theoretically and experimentally measured.

Computational fluid dynamics (CFD) modelling is one of the most advanced tools for the analysis of the gasification process. CFD models are based on the solution of a set of mathematical equations based on conservation of mass, momentum, energy, and species over a discrete region of the gasifier reactor [115,126,127]. CFD simulations provide the temperature profiles of the gasifier, solid and gas phases, as well as a complete chemical and fluid mechanical analysis of the reactor bed. CFD analysis can be used for the optimization of the gasifier design and to study the characteristics of the gasification process such as operating parameters, kinetics and physical properties of the feedstock. However, comprehensive CFD simulations for biomass gasification are scarce, mainly due to the lack of large computational resources and the anisotropic nature of biomass [125].

Artificial neural networks (ANNs) models are a relatively new approach to model the gasification process. ANN technique concerns the ability of the system to learn by itself from previous experiences, finding patterns in the responses and improving the subsequent outputs, imitating some human features. ANN models are able to predict gas yield and syngas composition with sufficient accuracy [117,127]. Such models do not provide an analytical solution but only numerical results [115,127]. They do not require the mathematical description of the phenomena occurring in the process, the only input required is the input data sets. For this reason, they constitute a useful tool for simulating and scaling the complex biomass gasification process. Nevertheless, the application of ANN for biomass gasification is rather rare [117].

The choice of the most suitable modelling approach to investigate the biomass gasification process is determined by the scope of analysis and the available experimental data. Complex models (e.g., kinetic, CDF and ANNs models) provide detailed information on mechanisms. However, the computational cost and the number of input data required are usually high. Although equilibrium models are valid under chemical equilibrium conditions, they are valuable because they can predict the thermodynamic limits of a gasification system, leading to the design, evaluation and improvement of the process [130,131]. Furthermore, the equilibrium models can constitute a useful design support in evaluating the limiting possible behaviour of a complex system that is difficult or unsafe to reproduce experimentally or in commercial operation [131].

4.2.1 Literature review on thermodynamic equilibrium modelling

The thermodynamic equilibrium approach is based upon the assumption that the components react in a fully mixed condition for an infinite period of time. This assumption can be considered realistic when the residence time of the reactants in the gasification zone is long compared to the half-life of all the reactants; gasification temperature can be assumed as constant, and chemical mixing is almost perfect [133]. These conditions are met in some specific types of reactors, mainly in downdraft fixed-bed reactors, and at high temperatures (e.g. > 1500 K) [134]. However, the equilibrium state may not be reached in some gasifiers and under specific operative conditions, in particular for gasifiers in which the operating temperatures are relatively low. Nonetheless, thermodynamic equilibrium models have been extensively employed to investigate the biomass gasification process [135].

Equilibrium models can be further categorized as non-stoichiometric or stoichiometric equilibrium approaches. Stoichiometric models are adapted from the equilibrium constants of a set of reactions [132], while the nonstoichiometric models are developed on the Gibbs free energy minimization. This formulation requires only the elemental composition of biomass as input, therefore it is particularly suitable for cases in which the system of chemical reactions that take place in the gasifier is not fully known [115]; while for the application of the stoichiometric equilibrium models, the knowledge of the main chemical reactions and species involved in the process is required.

Zainal et al. [136] proposed a stoichiometric equilibrium model for a downdraft gasifier investigating the effects of initial moisture content in the biomass feedstock and the temperature in the gasification zone on the producer gas composition and the calorific value.

Li et al. [137] developed a thermodynamic equilibrium model based upon the minimization of Gibbs free energy to predict the performance of a circulating fluidized bed gasifier. The authors proposed a phenomenological model modifying a previous model through the introduction of an availability function that uses empirical data (e.g. unconverted carbon and methane) to consider the non-equilibrium factors.

Sharma [138] presented a stoichiometric equilibrium model of the global reduction reactions for char – gas and gas – gas reactions that occurs in the reduction zone of a downdraft gasifier. In order to predict accurately the reaction temperature, the model considers by energy equations the heat exchanges that take place in the reduction zone. The results have showed a reasonable agreement with data collected from various sources for downdraft biomass gasifiers.

Jarungthammachote et al. [139] employed a thermodynamic equilibrium model based upon the equilibrium constants to predict the producer gas composition. In order to improve the accuracy of simulation results, the authors modified the model multiplying the equilibrium constant with appropriate coefficients calculated on the basis of experimental data.

Baratieri et al. [140] presented an equilibrium model for the biomass gasification process modified according to experimental data. The model has been calibrated using the concentration of CH_4 and C_2H_4 measured experimentally and the amount of char residue. The results of the modified model predicted accurately the syngas composition for the gasification process in the analysed fluidized gasifier.

Barba et al. [141] developed the Gibbs Free Energy Gradient Method Model (GMM). The gasification process has been modelled in two steps: in the first step, the

raw material is decomposed to produce a carbonaceous residue and a primary gas. In the second stage, the gas previously produced changes its composition due to the occurrence of water shift and steam reforming reactions.

In [142], the GMM thermodynamic model was employed to simulate an experimental campaign carried out at the ENEA Research Centre of Trisaia (Italy), which showed good accuracy to reproduce the experimental results of steam gasification of Refuse-derived fuel.

An advanced two-stage fluidized bed gasification was modelled by Materazzi et al. [143] using a non-stoichiometric approach. The model has a systematic structure consisting of principles of atomic conservation and equilibrium calculation routines. The model has been validated employing the experimental data of a pilot plant.

Sreejith et al. [144] presented an equilibrium model for steam gasification of biomass based upon the minimization of Gibbs free energy to identify the optimum values for the reactor varying temperature and pressure. The gas phases have been modelled as real gases in accordance with the Redlich–Kwong equation of state. Kangas et al. [145] developed a non-stochiometric equilibrium model with the constrained Gibbs energy method. The assumed chemical system consists of 14 constituents in the gaseous phase, liquid water phase and two solid phases for char and ash. Six methods for modelling global or local equilibrium were implemented by varying the constrained species.

Mendiburu et al. [146] developed four thermodynamic equilibrium models for the downdraft gasifiers, called M1, M2, M3 e M4. The first model M1 is a general stoichiometric equilibrium model. Models M2, M3 and M4 have been obtained modifying the model M1. In particular, in the model M2 two multiplicative coefficients calculated using experimental data have been introduced in the equilibrium equations. Model M3 implements the correlations for the CO/CO_2 and CO/H_2 according to [147]. Model M4 implements the substitution of the formula for the calculation of equilibrium constants with the Arrhenius type relations.

To improve the accuracy of the prediction of pyrolysis products, Biagini et al. [148] developed a multizonal model adapted from the non-stoichiometric equilibrium approach. The proposed model simulates the bypass of the oxidation zone of some products of pyrolysis phase inside the gasifier introducing a repartition coefficient of the volatile matter.

Gagliano et al. [116] presented a stoichiometric model to simulate the gasification process through a downdraft gasifier filled with residual biomasses. The proposed model can predict the percentage of tar and char produced, as well as the chemical

species in the producer gas. A good agreement between experimental data and simulation data has been found.

Gambarotta et al. [149] developed a thermodynamic equilibrium model for the biomass gasification process in downdraft gasifiers. The model is able to predict not only the concentration of the main component of syngas but also the content of minor products, especially the pollutant substances containing nitrogen and sulphur (e.g., ammonia, hydrogen sulphide).

4.3 *Case study #5: Reliability of thermodynamic equilibrium gasification models for selected biomass types and compositions*

4.3.1 Material and methods

In the present chapter, the author presents an analytical model able to predict gasification average temperature of the biomass bed, composition and flow rate of the synthesis gas produced as well as its energy content. The proposed model describes the process of biomass gasification using a concentrated parameter approach [150,151].

The hypotheses at the core of the model are: i) steady state; ii) uniform and constant properties of biomass inside the gasifier; iii) local thermodynamic equilibrium; iv) complete chemical reactions (i.e., the reactions taking place completely stoichiometrically); v) uniform and constant temperature of biomass bed. Input data for calculation are: i) the mass flow rate of biomass feedstock; ii) temperature and volumetric flow rate of combustion air; iii) biomass composition.

For modelling purposes, the chemical formula of biomass is defined as $CH_xO_yN_z$, where x, y and z are the number of hydrogen, oxygen and nitrogen atoms per number of carbon atoms in the feedstocks, respectively [152]. The latter is calculable knowing the elemental composition of biomass based on ultimate and proximate analysis.

Assuming thermodynamic equilibrium, the biomass gasification process is modelled according to the following global reaction:

$$\begin{aligned} CH_xO_yN_z + wH_2O + m(O_2 + 3.76N_2) \\ = n_{H_2}H_2 + n_{CO}CO + n_{CO_2}CO_2 + n_{H_2O}H_2O + n_{CH_4}CH_4 \\ + \left(\frac{z}{2} + 3.76m\right)N_2 \end{aligned} \quad (4.1)$$

where w is the amount of moisture per mole of carbon and, m=O/C is the amount of oxygen per mole of carbon. The number of moles of the different species, n_i, on the right-hand side represents the unknown quantities of the problem. The moles produced of H_2, CO, CO_2, H_2O and CH_4 were determined by solving simultaneous five equations. The first three equations were related to mass balance on the involved chemical elements, as shown in Eqs. (4.2) – (4.4) [152–154].

Carbon mass balance:

$$n_{CO}CO + n_{CO_2}CO_2 + n_{CH_4}CH_4 - 1 = 0 \tag{4.2}$$

Hydrogen mass balance:

$$2n_{H_2} + 2n_{H_2O} + 4n_{CH_4} - x - 2w = 0 \tag{4.3}$$

Oxygen mass balance:

$$n_{CO} + 2n_{CO_2} + n_{H_2O} - w - 2m = 0 \tag{4.4}$$

The two additional equations were obtained under the assumption of chemical equilibrium, minimizing energy Gibbs free energy relative to the methanation reaction:

$$C + 2H_2 = CH_4 \tag{4.5}$$

and to the water – gas shift reaction:

$$CO + H_2O = CO_2 + H_2 \tag{4.6}$$

The equilibrium constants for the reactions (4.5) and (4.6) are given by the following equation [151,152,155]:

$$ln(K) = -\frac{\Delta G_T^0}{\bar{R}T} = -\frac{\sum_i v_i \overline{(\Delta g)}_{f,T,i}^0}{\bar{R}T} \tag{4.7}$$

where $\bar{R} = 8.314\ \left(\frac{kJ}{kmol \cdot K}\right)$ is the universal gas constant, ΔG_T^0 is the standard Gibbs function of reaction, T is the temperature and $\overline{(\Delta g)}_{f,T,i}^0$ is the standard Gibbs function of formation of the gaseous species in the producer gas at temperature the T. The latter can be evaluated employing the empirical equation below:

$$\overline{(\Delta g)}_{f,T}^0 = \bar{h}_f^0 - a'Tln(T) - b'T^2 - \frac{c'}{2}T^3 - \frac{d'}{3}T^4 + \frac{e'}{2T} + f' + g'T \tag{4.8}$$

The values of coefficients a', b', c', d', e', f' and g' are reported in [152] for the i-th component involved (i.e., CO, CO_2, CH_4, H_2O).

In this model, thermodynamic equilibrium was assumed for all chemical reactions in the gasification zone. Moreover, all gases were assumed to be ideal and all reactions

form at pressure 1 atm. Therefore, the equilibrium constants for methanation reaction and water gas shift reaction are given by ensuing relations [139,156,157]:

Methanation reaction:

$$K_1 = \prod_i x_i^{v_i} \left(\frac{p}{p_0}\right)^{\sum_i v_i} = \frac{n_{CO_2} \cdot n_{total}}{{n_{H_2}}^2} \tag{4.9}$$

Water gas shift reaction:

$$K_2 = \prod_i x_i^{v_i} \left(\frac{p}{p_0}\right)^{\sum_i v_i} = \frac{n_{CO_2} \cdot n_{H_2}}{n_{CO} \cdot n_{H_2O}} \tag{4.10}$$

where x_i is the mole fraction of species i in the ideal gas mixture, ν is the stoichiometric number (positive value for products and negative value for reactants), p_0 is the standard pressure and n_{total} is the total mole of producer gas. Using the equations (4.9) – (4.10), it is possible to calculate the concentration of products and reactants. Mass balances and chemical equilibrium relations equations are solved together with the energy conservation equation for the gasification process, allowing the gasification temperature prediction. The energy balance for this process can be written as:

$$\begin{aligned} h^0_{f,CH_xO_yN_z} + w h^0_{f,H_2O} + \frac{\dot{n}_{O_2}}{\dot{n}_{CH_xO_yN_z}} h_{T_{IN},O_2} + \frac{\dot{n}_{N_2}}{\dot{n}_{CH_xO_yN_z}} h_{T_{IN},N_2} \\ = n_{H_2} h_{T_{OUT},H_2} + n_{CO} h_{T_{OUT},CO} + n_{CO_2} h_{T_{OUT},CO_2} + n_{CH_4} h_{T_{OUT},CH_4} \\ + n_{H_2O} h_{T_{OUT},H_2O} \end{aligned} \tag{4.11}$$

where $h^0_{f,CH_xO_yN_z}$ and h^0_{f,H_2O} are the formation enthalpy of organic matter and water at reference condition (298 K and 101325 Pa) in kJ/kmol, respectively; n_i represents the number of moles produced, for the same chemical species, per mole of consumed fuel; lastly, $h_{T,i}$ is the enthalpy associated with the i-th chemical species at the temperature T, and it is the sum of the formation enthalpy and the difference of enthalpy between the state in which the substance is found and the reference status.

The enthalpy of formation for organic matter, $h^0_{f,CH_xO_yN_z}$, in reactant is calculated according to the relation suggested in [139]:

$$h^0_{f,CH_xO_yN_z} = LHV + \sum_{k=prod} [n_k (\bar{h}^0_f)_k] \tag{4.12}$$

where LHV is the lower heating value of the dry fraction of biomass estimated in accordance with the formula reported in [139]:

$$LHV = HHV - 9 \cdot H \cdot h_{fg} \tag{4.13}$$

where H is the mass fraction of hydrogen in the biomass, $h_{fg}$is the enthalpy of vaporization of water at reference conditions and HHV is the higher heating value calculated on the basis of biomass composition conforming to the following equation [156]:

$$HHV = 0.3491 \cdot C + 1.1783 \cdot H + 0.1005 \cdot S - 0.1034 \cdot O - 0.0151 \cdot N + \\ -0.0211 \cdot ash \tag{4.14}$$

where C, H, O, N, S and ash are the mass fraction of carbon, hydrogen, oxygen, nitrogen, sulphur and ash in the biomass.

The calculation of the temperature, the chemical composition and the volumetric flow rate of the syngas produced from biomass gasification process is based on an iterative process. Namely, the calculation procedure is based on the following steps: i) an average gasification temperature of the first attempt is assumed; ii) the mass conservation and chemical equilibrium equations are solved using the Newton-Rapson method [156] by that means obtaining the composition of the producer gas; iv) the energy conservation equation is solved determining the new average gasification temperature; v) the iterative method stops when convergence is achieved.

4.3.2 Results and discussion

The present study has been performed in cooperation with the research group from University of Naples Parthenope, which developed a thermodynamic equilibrium model using a commercial software, i.e., Aspen Plus®. In order to assess the strengths and weaknesses of non-commercial and commercial codes, a comparison between the results obtained from the two developed models has been carried out. In the following, the commercial software-based model is referred as “Aspen model”, whereas the non-commercial tool is referred as “Analytical model”.

For the purpose of evaluating the accuracy of the simulation results on varying the biomass properties and the gasification operating conditions, and evidencing advantages and disadvantages of employing such models the developed thermodynamic equilibrium models have been applied to different experimental data on downdraft gasifiers available in scientific literature.

In Table 4.1 and Table 4.2, the ultimate and proximate analysis of the different types of biomasses used in the experimental campaigns and the operating conditions of the simulated case studies have been summarized. Symbols C, H, O, N and S in Table 4.2 represent, respectively, the carbon, hydrogen, oxygen, nitrogen and sulphur

content in the biomass on dry basis (d.b.), while VM and FC are the volatile matter and fixed carbon, respectively.

Table 4.1 – Ultimate and proximate analysis of biomass used for the validation of models.

		Ultimate analysis [wt.% d.b.]					Proximate analysis [wt.% d.b.]		
Ref.	**Biomass**	**C**	**H**	**O**	**N**	**S**	**VM**	**FC**	**ASH**
[158]	Hazelnut shell	46.76	5.76	45.83	0.22	0.67	71.62	27.50	0.88
[159]	Rubber wood	50.60	6.50	42.00	0.20	-	80.10	19.20	0.70
[160]	Wood Pellets	52.05	5.82	40.85	0.28	0.01	77.70	21.30	1.00
[148]	Corn cobs	46.59	5.97	44.81	0.51	-	80.06	17.82	2.12
[148]	Wood pellets	47.88	5.68	44.16	0.18	-	80.63	17.27	2.10
[148]	Rice husks	41.23	5.21	36.50	0.45	-	67.95	15.45	16.6
[148]	Vine pruning	49.51	5.67	41.35	0.86	-	80.84	16.54	2.62
[161]	Coniferous wood	49.79	5.55	43.91	0.10	0.38	-	-	0.28

Table 4.2 – Gasifier operating conditions of the experimental tests used for the validation of models.

Ref.	**Biomass**	**Case**	**Biomass feeding rate [kg/h]**	**Air flow rate [Nm^3/h]**	**Equivalence ratio (ER)**	**Moisture content [wt.%]**
[158]	Hazelnut shell	1	1.73	2.82	0.449	12.5
		2	2.15	3.53	0.451	12.5
		3	2.64	4.01	0.418	12.5
		4	3.19	4.40	0.380	12.5
[159]	Rubber wood	5	27.39	43.00	0.406	18.5
		6	25.27	43.00	0.425	16.0
		7	23.46	43.00	0.455	14.7
		8	28.37	43.00	0.380	16.0
[160]	Wood pellets	9	4.10	5.50	0.301	7.0
		10	6.20	9.60	0.347	7.0
		11	6.40	8.70	0.305	7.0
		12	5.90	6.70	0.254	7.0
[148]	Corn cobs	13	59.00	69.30	0.279	10.1
		14	73.00	85.00	0.277	10.1
		15	73.00	88.70	0.287	10.1
[148]	Wood pellets	16	58.00	62.30	0.272	9.5
[148]	Rice husks	17	50.00	73.90	0.382	12.5
		18	63.00	100.50	0.414	12.5

[148]	Vine pruning	19	44.00	51.10	0.257	17.6
[161]	Coniferous wood	20	0.54	0.81	0.301	7.1
		21	0.56	0.91	0.322	7.1
		22	0.60	1.06	0.337	7.1
		23	0.60	1.14	0.368	7.1

The comparison between numerical and experimental results has been carried out in terms of: i) molar composition of syngas (e.g., CH_4, H_2, CO, CO_2 and N_2) and ii) average gasification bed temperature. The analytical model is able to predict the average gasification bed temperature; therefore, the model has been validated also comparing the temperature values obtained from simulation with the experimental temperature values. The comparison has been carried out using the data reported in [158] and [161] as these are the only works containing information on the gasification temperature, among those considered in this paper.

Present results have been obtained calibrating both the analytical and the Aspen models. In particular, the analytical model has been calibrated by calculating the K_1 and K_2 values that minimize the error between the experimental and the model results in terms of gas composition and average combustion bed temperature. As regards the Aspen model, the calibration is based on the Restricted Equilibrium Model.

The results of such a comparison, as a function of the equivalence ratio (ER), for the considered biomasses and case studies, are shown from Figure 4.1 to Figure 4.8 and in Table 4.3 and Table 4.4.

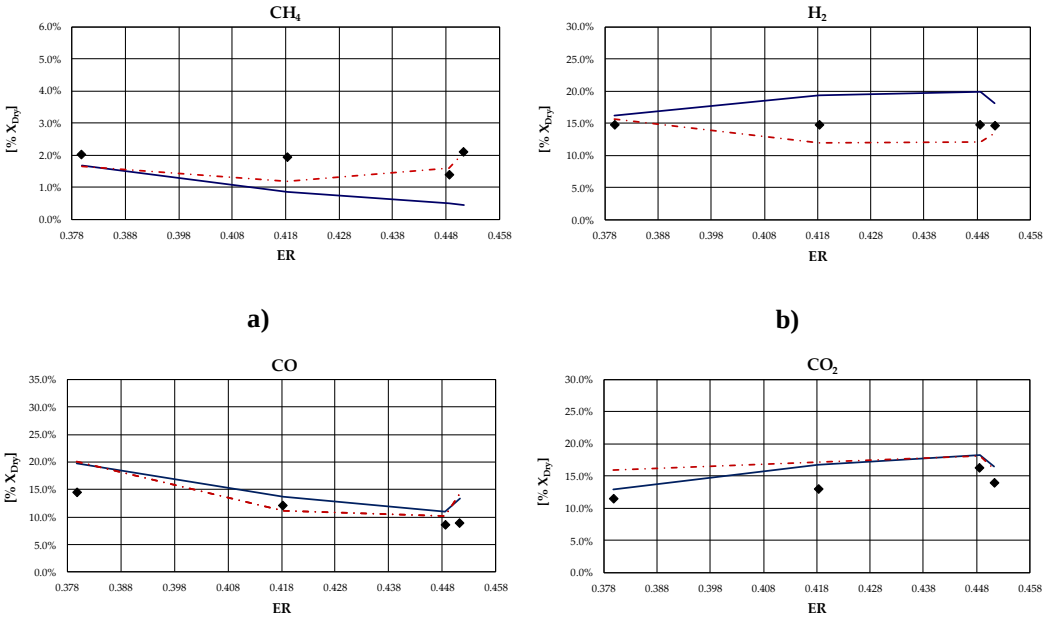

c) **d)**

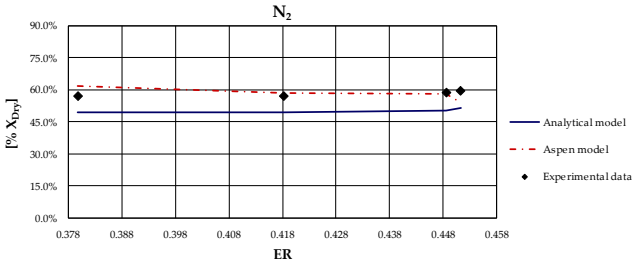

e)

Figure 4.1 – Comparison of syngas mole fraction composition between results of calibrated and not-calibrated analytical and Aspen models and experimental data relating to hazelnut shell [158]: a) CH_4 mole fraction; b) H_2 mole fraction; c) CO mole fraction; d) CO_2 mole fraction; e) N_2 mole fraction.

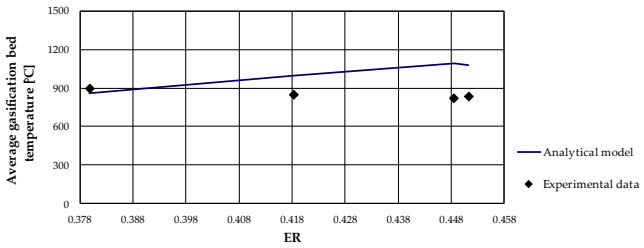

Figure 4.2 – Comparison of average gasification bed temperature between the analytical model results and experimental data relating to hazelnut shell [158].

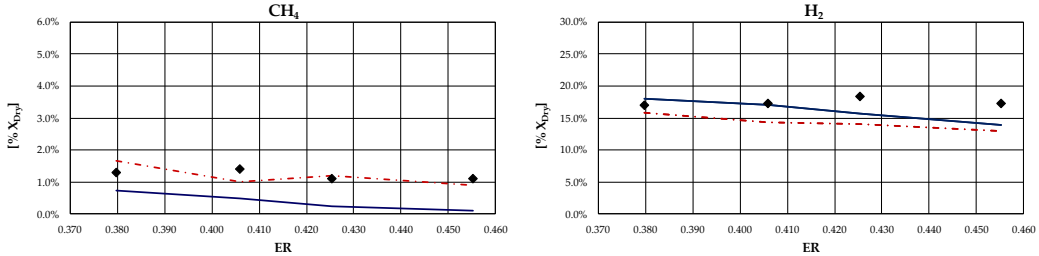

a) **b)**

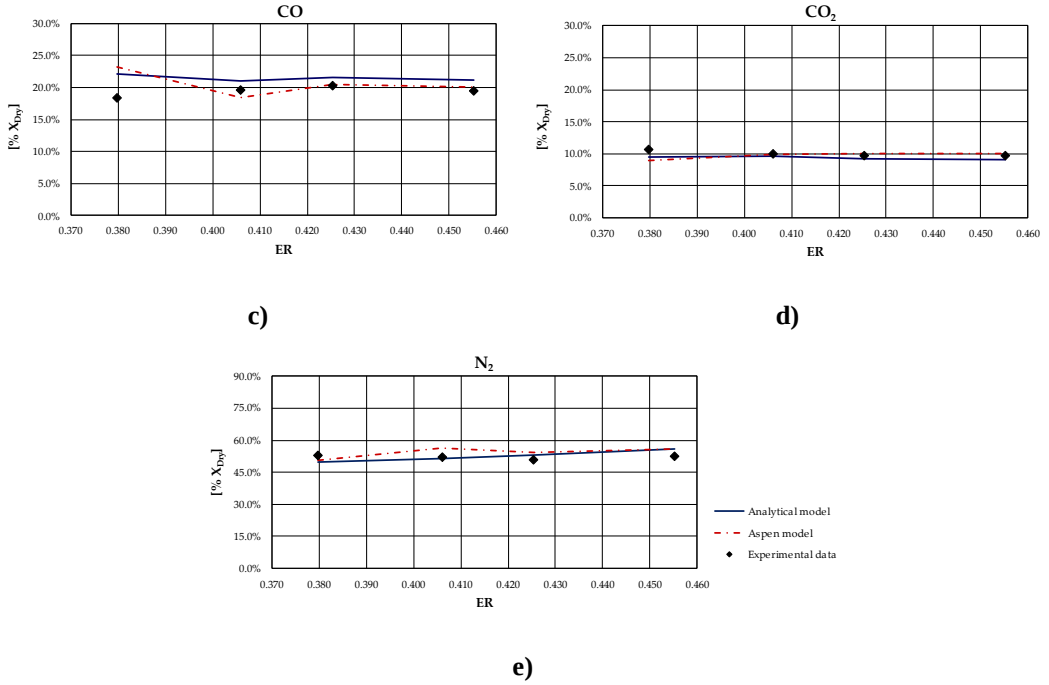

Figure 4.3 – Comparison of syngas mole fraction composition between results of calibrated and not-calibrated analytical and Aspen models and experimental data relating to rubber wood [159]: a) CH_4 mole fraction; b) H_2 mole fraction; c) CO mole fraction; d) CO_2 mole fraction; e) N_2 mole fraction.

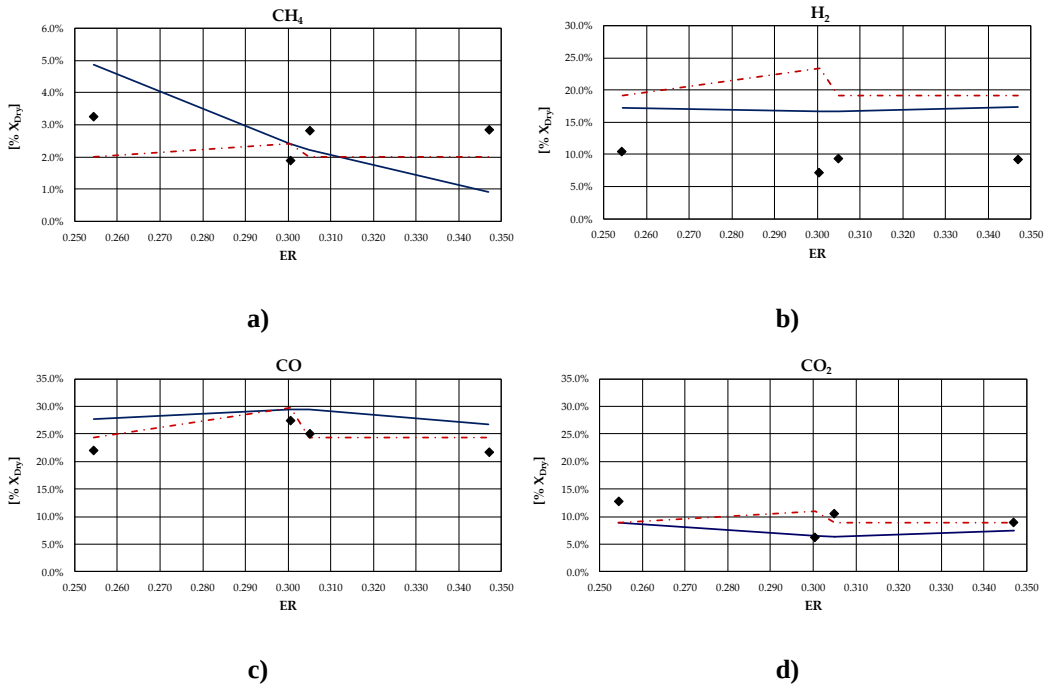

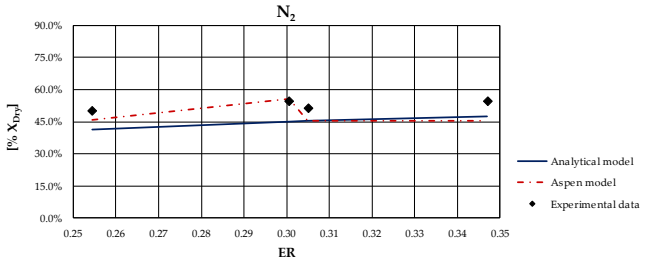

e)

Figure 4.4 – Comparison of syngas mole fraction composition between results of calibrated and not-calibrated analytical and Aspen models and experimental data relating to wood pellets [160]: a) CH_4 mole fraction; b) H_2 mole fraction; c) CO mole fraction; d) CO_2 mole fraction; e) N_2 mole fraction.

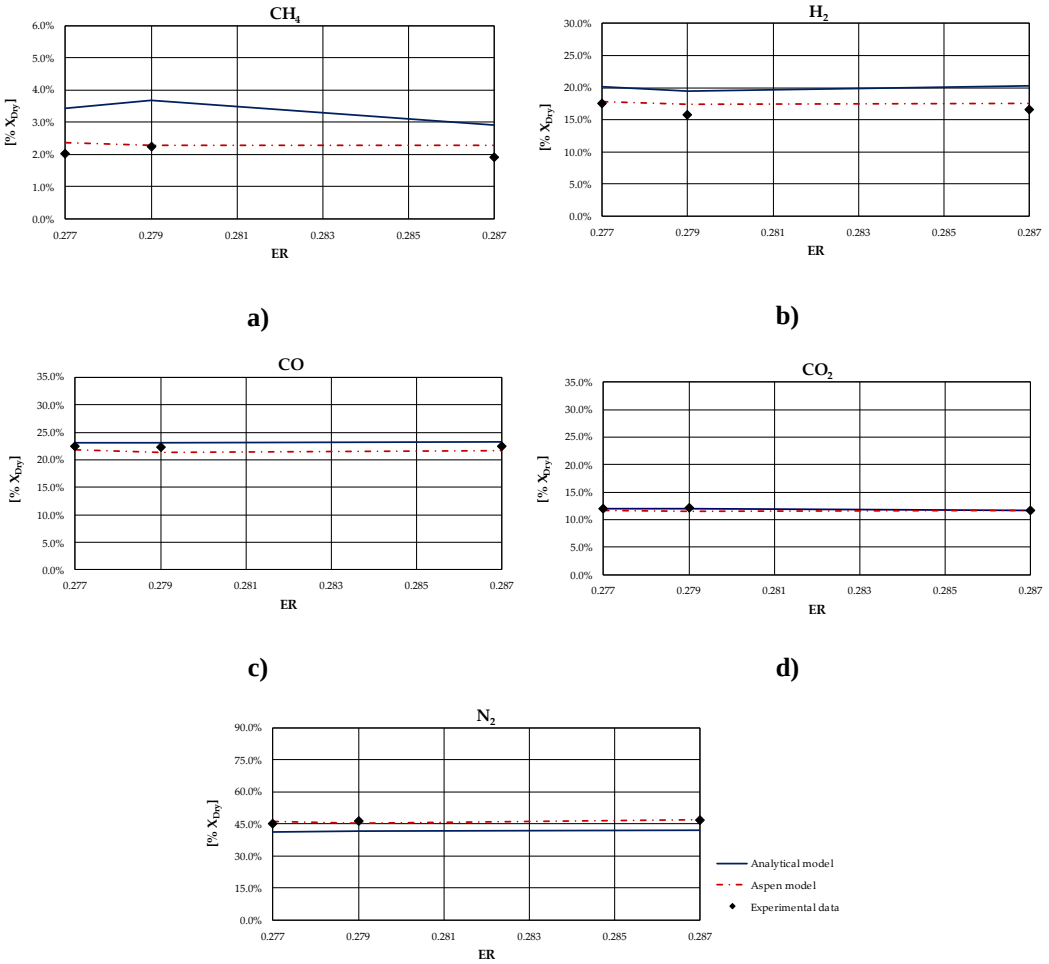

a) **b)** **c)** **d)** **e)**

Figure 4.5 – Comparison of syngas mole fraction composition between results of analytical and Aspen models and experimental data relating to corn cobs [148]: a) CH_4 mole fraction; b) H_2 mole fraction; c) CO mole fraction; d) CO_2 mole fraction; e) N_2 mole fraction.

Table 4.3 – Comparison of syngas mole fraction composition between results of analytical and Aspen models and experimental data relating to wood pellets [148].

	Analytical model	Aspen model	Experimental data
ER	0.272		
CH_4 [%]	3.6	2.3	2.3
H_2 [%]	19.4	17.5	16.7
CO [%]	24.5	21.4	21.3
CO_2 [%]	11.5	11.5	12.4
N_2 [%]	41.0	45.4	47.3

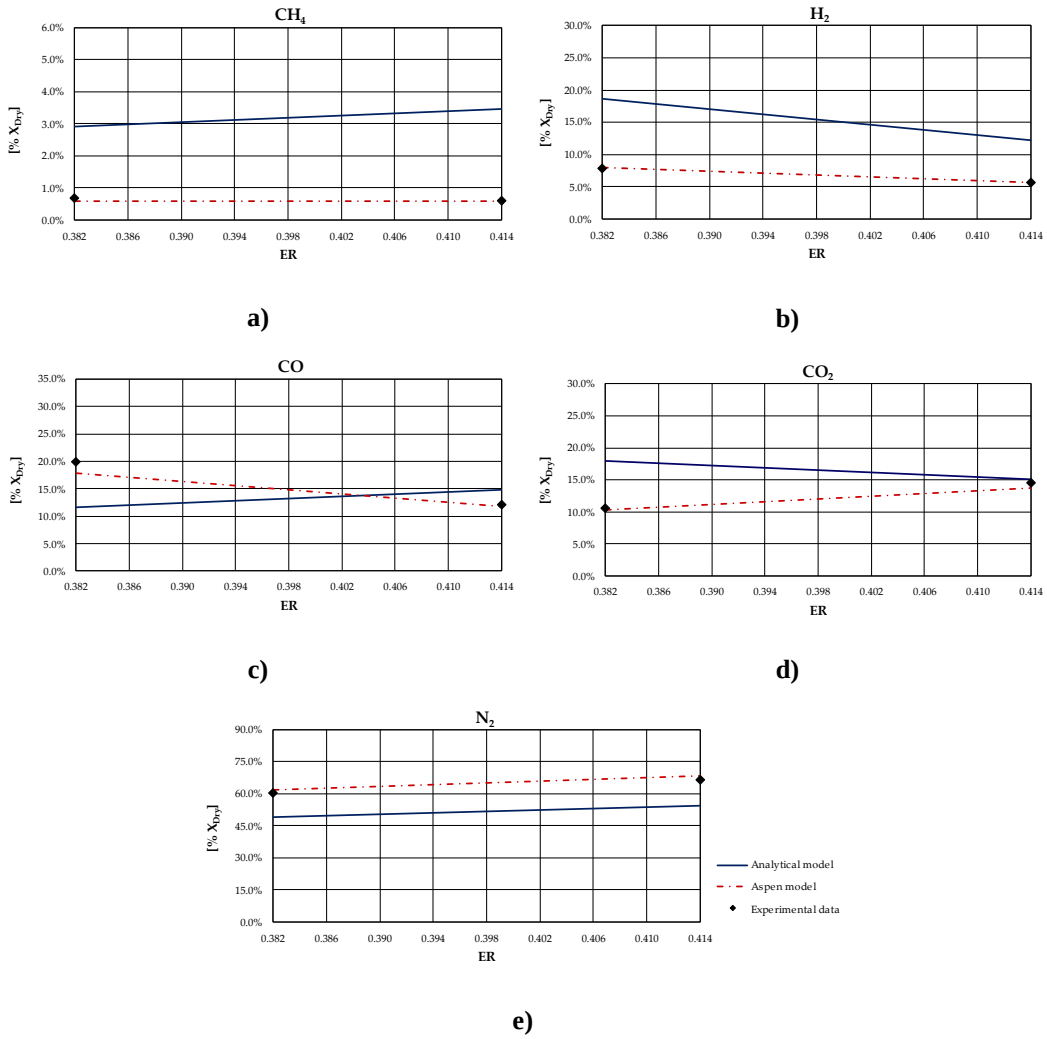

Figure 4.6 – Comparison of syngas mole fraction composition between results of calibrated and not-calibrated analytical and Aspen models and experimental data relating to rice husks [148]: a) CH_4 mole fraction; b) H_2 mole fraction; c) CO mole fraction; d) CO_2 mole fraction; e) N_2 mole fraction.

Table 4.4 – Comparison of syngas mole fraction composition between results of analytical and Aspen models and experimental data reported in [148].

	Analytical model	Aspen model	Experimental data
ER	0.257		
CH_4 (%)	3.8	2.7	2.6
H_2 (%)	21.8	18.3	17.1
CO (%)	23.1	23.4	21.7
CO_2 (%)	12.0	10.8	13.3
N_2 (%)	39.3	44.7	45.1

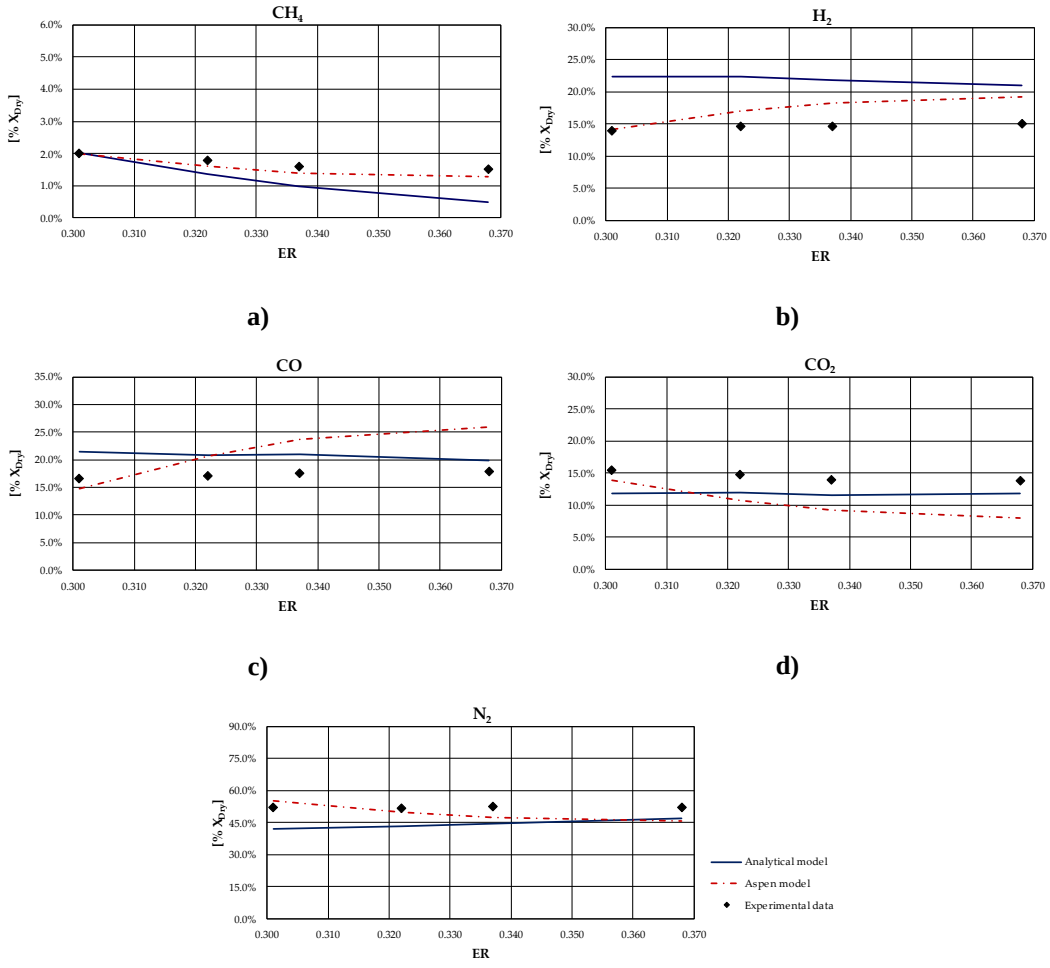

Figure 4.7 – Comparison of syngas mole fraction composition between results of analytical and Aspen models and experimental data relating to coniferous wood [161]: a) CH_4 mole fraction; b) H_2 mole fraction; c) CO mole fraction; d) CO_2 mole fraction; e) N_2 mole fraction.

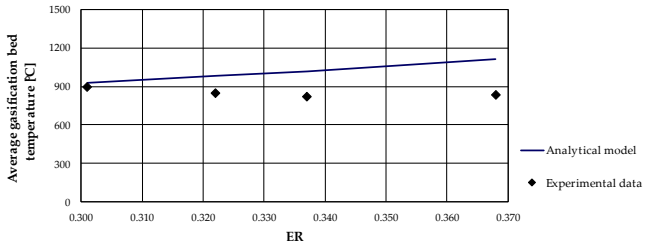

Figure 4.8 – Comparison of average gasification bed temperature between the analytical model results and experimental data relating to coniferous wood [161].

From the analysis of figures and tables, it can be observed that even though the proposed models are both based on the thermodynamic equilibrium hypothesis, significant differences can be observed in obtained results. In particular, CH_4 and H_2 molar fractions evaluated using the analytical model are characterized by a higher deviation from experimental values compared to the other synthesis gas components. In detail, CH_4 molar concentration is underestimated for the case studies in which the ER is higher. Conversely, it is overestimated for the case studies in which the ER is lower. Furthermore, CH_4 content decreases as ER increases for all types of biomasses, except for rice husks. The analytical model generally overestimates the H_2 molar fraction regardless of the biomass feedstock and operating condition of gasification process. A good agreement between the results of the analytical model and experimental values can be observed as regards the CO and CO_2 molar concentrations for all case studies analysed. The N_2 content tends to be underestimated by the analytical model for each simulated case, probably because of the restrictive hypothesis of complete carbon conversion on which the model is based. As regards the Aspen model, a generally satisfactory agreement between the numerical results and the experimental data can be observed, except for the campaign carried out in [160] for which the trend of the fuel compounds, CH_4 and H_2, is not adequately captured. Ignoring this last group of results, the highest average deviation be-tween the numerical and the experimental data is 23%, obtained for the first case of the campaign carried out in [158]. More in detail, the concentration of CH_4, which slightly decreases with the ER, is well predicted by the model. Such a result is promising since usually the compounds characterized by the lowest concentrations, such as methane, are the ones giving the highest deviations between numerical and experimental results. Also the trend of H_2 concentration, which slightly varies with the ER, is fairly predicted by the model, except for the campaign carried out in [159] and shown in Figure 4.3. This could be related to the variation of the moisture content that influences the H_2

concentration in the syngas. The concentrations of CO and CO_2 usually show an inverse trend due to the water shift reaction in which they are involved. Their trend, as well as that of N_2, is in excellent agreement with the experimental results. Obviously, the higher the ER the higher the dilution and thus the N_2 concentration.

As expected, obtained results evidence that the major limitation of both models relies in the thermodynamic equilibrium assumption and in neglecting tar and char. In fact, the results show that syngas composition is better reproduced for the biomass types characterized by a low ash content and consequently, a relatively high heating value. Indeed, the major deviations from experimental data have been obtained for cases of gasification of rice husks, whose ash content is about 16.6 % on dry basis, as can be noted in Figure 4.6. This can be ascribed to the fact that the model does not simulate the tar and char formation that in this case are a considerable part of the products of the gasification process.

Concerning the evaluation of average gasification bed temperature, as expected, as the ER increases the temperature increases, as can be observed from Figure 4.2 and Figure 4.8. Since the gasifier is assumed to be adiabatic, analytical model generally overestimates the gasification temperature and the deviation between numerical results and experiments increases as the ER increases.

In general, it can be seen how using a more advanced model of Restricted Equilibrium allows to obtain results closer to the experimental ones, minimizing the error between simulated and experimental data, especially for the concentrations of CH_4 and H_2 which being very low values are difficult to model. Nevertheless, in the case of absence of necessary information for the calibration, the use of the non-calibrated Aspen model produces non reliable results. Moreover, it does not predict the gasification temperature. On the contrary, the analytical model is more general and the calibration process allows to find out the optimal multiplying coefficients of K_1 and K_2 constants to be used as a function of the biomass type and ash content. Besides, the calculation of the gasification temperature is performed by solving the energy conservation equation.

In summary, the limit of this approach occurs in critical conditions in which the thermodynamic equilibrium is not likely achieved and biomass is characterized by high humidity content, ashes, tar and char.

In the future, the simulation of tar and char formation will be included in the model. In addition, the model will be implemented in a more complex modelling of polygenerative systems based on renewable sources with the aim of optimizing these systems from an energy and economic point of view.

Finally, since it based on a non-commercial home-made code, future improvements in its ability to predict methane and hydrogen concentration can be easily implemented.

CONCLUSIONS

In this work the complex issue of innovative use of the existing NG infrastructure, as well as the development of innovative technologies on natural gas transportation and distribution networks, has been address. The subject has been treated in a multidisciplinary manner, allowing the reader to have a broader view of the problem in its different facets. To this aim, numerous research experiences have been reported in the present thesis as case studies.

In *Chapter 1*, the subject of NG networks management in the event of fault occurrence is tackled employing the concept of resilience. Based on the literature review, one of challenges integral to assess the resilience of complex infrastructural systems, such as NG pipeline systems, is the development a holistic methodology able to take into account multiple factors, such as geometrical and topographic characteristic of the system, type of the fault, consumption scenario, recovery strategy etc., that impact on the state of service resulting from an unpredictable event.

To overcome such gap, the author proposed a novel resilience assessment methodology for acquiring, simulating, and processing the impact of failures on NG distribution networks (*case study #1*), with the aim to evaluate the behaviour and fragility of distribution networks, under different fault scenarios and network structures, as well as to evaluate the fault management strategies to minimize the disservice and to define possible structural improvement measures. In detail, the author proposed a resilience assessment methodology based on network simulation to improve the resilience of NG distribution networks through: i) the estimation of the impact of a generic fault in the network in terms of quality of the service and potential number of disrupted citizens; ii) the identification of possible critical areas in which users are more susceptible to disruptions; iii) the development of operational

management strategies; iv) the selective assessment of structural improvements in the network to reduce the risk of fault and improve the resilience of the network itself.

The proposed methodology has been experimented in a real case study of a natural gas distribution network in southern Italy showing the effectiveness of this approach capable of avoiding or minimizing the risk of service interruption, through:

i. the identification of the type of fault and the operating conditions with greatest impact;
ii. the analysis of hourly trend of the number of disrupted users/nodes and the appropriate programming of the restoration interventions;
iii. the development of targeted users breakdown as applicable recovery strategy (e.g., aiming at the disruption of a limited number of users that can be more easily reactivated after the fault has been repaired).

This approach may in the future be increasingly effective thanks to the greater availability of smart meters. These tools will allow distribution companies to better profile user consumptions on the basis of actual data form smart meters and to build increasingly precise and reliable structures and operating models for the network.

In *Chapter 2*, the author investigated the technical feasibility of the PtG concept to store intermittent RESs through the analysis and discussion of two different case studies.

In *case study #2*, a PtSNG plant coupled with a 12 MW wind farm has been designed and investigated by evaluating nominal and annual efficiencies for different sizes of the electrolysis unit. The analysed plant consists of four sections: (i) the electrolysis unit, (ii) the CO_2 methanation unit, (iii) the hydrogen storage unit, and (iv) the SNG upgrading unit. The main design specifications of the PtSNG plant regard the SNG composition (CH_4>95%, $H_2 \leq 5\%$, and CO_2 balance), and the capacity of the storage unit (minimum size to assure about 6.5 h of full load for the methanation unit with a small number of shutdowns and ON/OFF cycles). In order to define the plant operating conditions and the plant sizing in terms of mass and energy flows, an integrated thermochemical and electrochemical model has been developed. This model has allowed to assess the energy and mass balances as well as the performances

of each plant section in steady state conditions (i.e., full or partial load). The dynamic operation of the PtSNG plant has been investigated by developing a dynamic model that assess the mass and energy fluxes between the plant sections by following the control strategy of the storage unit, conceived to reduce the shutdowns and the ON/OFF cycles of the methanation unit with the minimum storage capacity. The findings obtained by applying the integrated steady state model and the dynamic model are:

i. the nominal overall efficiency, referred to the LHV and calculated by considering only the SNG as useful product, is equal to 44% for all the three plant sizes considered; in the full load operation, the SNG production is equal to 34.1, 102.4, and 204.9 kg/h, respectively;
ii. the rectifier efficiency (the efficiency of the AC/DC transformer) and the electrolysis unit efficiency mainly impact on the overall plant efficiency; thus, using more efficient devices (i.e., by assuming 98% and 70%), the overall nominal efficiency is 58.1%;
iii. in order to increase the plant performances, the heat generated during the methanation operation should been valorised using thermal storage or in power generation systems; to this end, further investigations and improvement of the developed models are required;
iv. the operation time diminishes with the plant capacity, reaching the greatest value (6047 h) for the 1 MW size configuration that shows also the smallest number of shutdowns (212);
v. the annual overall efficiency as well as the plant load factor achieves the greatest values (43.7%, LHV basis and 60%) for the 1 MW size configuration. The annual SNG production is equal to 179,000 Nm^3/year.

In *case study #3*, two heat recovery systems for a 1 MW (the DC wind power to the electrolysis unit) PtSNG plant coupled with a 12 MW wind farm have been presented. The common approach is based on the valorisation of the waste heat generated during the plant operation to self-sustain, from an energetic point of view, the standby conditions (hot-standby and cold-standby). In the first one (thermal storage configuration), the recovered thermal energy is used to satisfy the thermal energy

demand of the reactors during the standby periods by means of a thermal carrier (hydrogen). In the second one (electrical storage configuration), the stored thermal energy is used to produce electricity by means of an Organic Rankine Cycle (ORC) where iso-butane is used as the working fluid. This electrical energy is then stored in batteries, and it is used to meet the energy requirements of the electrical trace heating system of the methanation unit during the standby periods. The analysis has been performed by means of thermochemical and electrochemical models developed in the Aspen Plus environment to define the mass and energy balances in steady-state conditions and integrated with a dynamic model built in the Matlab language to forecast the plant operation time and the annual performance. The main constraint for the thermal recovery systems sizing is the minimisation of the storage devices (oil tanks for the thermal storage configuration or batteries for the electrical storage configuration) achieved by identifying the optimum combination between the hot- and cold-standby hours. To this end, statistical analysis of the plant standby hours distribution in terms of the average duration and frequency has been carried out. For the specific energy input profile, the maximum duration of the hot standby has been found equal to 19 h. Results of the thermal storage configuration have shown that the hydrogen flow rate needed to maintain the methanation reactors at the minimum catalyst temperature (250 °C) is equal to 6.5 kg/h at 367 °C, while the hot oil flow rate required to heat the hydrogen is equal to 31.5 kg/h and is stored at 387 °C. Results of the electric storage configuration have shown that the electric power generated is equal to 24 kW and the ORC cycle efficiency is 16.6%. The battery is sized for a capacity of 80 kWh, guaranteeing 19 h of hot standby and a cold restart by means of electrical trace heating. When the methanation unit is in operation and the ORC produces electrical energy, part of this is used for plant auxiliaries (12.3 kWh at full-load operation for 1 h), so the electrical energy useful to charge the battery is equal to 11.8 kWh, resulting in a battery charge time of 6.8 h. The overall nominal efficiencies obtained for the PtSNG plant are equal to 43.9% and 48.8% on LHV and HHV bases, respectively. When heat recovery systems are coupled to the plant, the annual efficiencies on an LHV basis have been found to be 44.0% and 44.3% for the thermal storage and electrical storage configurations, respectively. The results showed that the

internal heat recovery system positively impacted the annual efficiency. It is expected that this could lead to a decrease in the plant operational costs with an associated relatively low initial capital expenditure. Furthermore, the amount of waste heat recoverable from the methanation unit resulted in being significantly higher than the energy needed for the self-sustainment of the plant. Therefore, to achieve a considerable increase in the efficiency of the plant, it is necessary to couple the plant with other thermal or electrical utilises (e.g., district heating, cogeneration of SNG and power, etc.). In the event that a decision is made to carry out cogeneration of electricity to sell it to the grid, this could also be produced with more efficient systems than the ORC (e.g., steam turbine), but careful cost assessments are required both on initial investments and on possible revenues.

It has to be underlined that the results presented both in *case study #1* and *case study #2* are valid only for the specific hypotheses and technologies adopted, as well as for the specific profile of the electrical input and the chosen plant management strategy.

In *Chapter 3*, an overview of the effect of hydrogen injection on NG networks has been presented. As *case study #4*, the analysis of impact of hydrogen injection on the reliability of measuring devices that currently run on the existing NG infrastructures has been proposed.

In particular, the changes in thermodynamic properties of the gas mixtures with different H_2 contents (i.e., up to 25%vol) have been evaluated and the effects on the accuracy of volume conversion at standard conditions have been investigated. Moreover, the author has been presented and discussed the effect of H_2 injection in gas networks on static ultrasonic domestic gas meters, both from a theoretical and an experimental point of view. Finally, the impacts of hydrogen injection on NG quality measurements have been discussed from a theoretical point of view.

The results obtained show that injection of H_2 into natural gas significantly impacts the relative density, specific heat and higher calorific value and speed of sound (which is a critical parameter for ultrasonic static gas meters), while the Wobbe Index is less affected. In particular:

i. the relative density decreases as the H_2 content increases (e.g., for the investigated GAS 6 10%vol of H_2 is sufficient for the corresponding limit to be exceeded);
ii. the higher calorific value significantly decreases as the H_2 content increases (e.g., for gases characterized by a low content of CH_4, the calorific value is reduced by 20% when the hydrogen content is equal to 25%, exceeding the lower limit indicated by the ISO 12213-2 standard;
iii. the speed of sound increases up to 12.3% becoming generally higher than the accepted limit of 475 $m \cdot s^{-1}$ indicated by ISO 14236 for ultrasonic gas meters already at x_{H2} = 5%.

The trend of the compressibility factor Z as a function of H_2 injection was also analysed using the available calculation algorithms of ISO 12213-2 (complete composition), ISO 12213-3, AGA NX 19 and AGA NX 19 Mod. The obtained results show that the compressibility factor at high pressures is more influenced by the presence of hydrogen than at low pressures (e.g., Z increases in the range 0.10–0.14% at 5 bar and in the range 2.1–9.1% at 70 bar). Moreover, the pressure influence on Z is more significantly impactful at low H_2 contents. A similar behaviour has been found for the volume conversion factor.

In the end, no influence on the deterioration of metrological properties has been found for domestic G4 ultrasonic gas meters tested with the use of various gas mixtures with hydrogen content up to 10%. In fact, both the errors of indications and the weighted mean errors remained within the permissible limits, with measured errors not exceeding ±1% and WME within ±0.4%.

In *Chapter 4*, the author presents an overview of biomass gasification modeling approaches with the aim to evaluate their effectiveness as a modeling tool for the design and optimization of polygeneration plants based on biomass gasification. In fact, the necessity to build plant operating maps for efficiency optimization requires a significant number of simulations and thermodynamic equilibrium models may allow fast computations thanks to their relative simplicity. The main objective consists in the assessment of thermodynamic equilibrium models as a function of biomass type and

composition to better understand in which conditions of practical interest such models con be applied with acceptable reliability. To this aim, the author proposed an equilibrium model using a simulation tool implemented in a non-commercial script as *case study #5*. The present study has been performed in cooperation with the research group from University of Naples Parthenope, which developed a thermodynamic equilibrium model using a commercial software, i.e., Aspen Plus®. In order to assess the strengths and weaknesses of non-commercial and commercial codes, a comparison between the results obtained from the two developed models has been carried out.

The developed thermodynamic equilibrium models have been applied to different case studies on downdraft gasifiers available in the literature in order to evaluate the accuracy of the simulation results on varying the biomass type and composition and the operating conditions of the gasification process, also evidencing advances and disadvantages of both models. Obtained results have been compared with experiments in terms of: i) molar composition of syngas and ii) average gasification bed temperature.

In general, the simulation results are comparable with the experimental data for both models. Namely, the results show that the analytical model predicts the syngas composition with better accuracy for the biomass types characterized by a low ash content and consequently, a relatively high heating value. This can be ascribed to the fact that the model does not simulate the tar and char formation. As regards the Aspen model, it appears to fairly predict the syngas composition at different conditions of ER. However, if the properties of the treated biomass change, the accuracy of the model may be reduced. Even though CH4 and H2 syngas concentrations are typically very low and difficult to predict, values predicted by the Aspen model are in satisfactory agreement with experiments.

Finally, the developed models offer several advantages: i) not require details of system geometry or estimate the necessary time to reach the thermodynamic equilibrium; ii) employ a limited number of input data; iii) lack of need of employing correlation for the calculation of the biomass gasification temperature. In addition, the adoption of a general model also allows to obtain quickly results in the case it is necessary to simulate numerous operating conditions.

APPENDIX A

A.1 Methanation Unit Modelling

In order to validate the proposed TREMP model, shown in Figure A.1, a comparison of experimental data reported in [66] with the simulated results using the present model was performed. The experimental data refers to results obtained by experiments on high-temperature methanation carried out in the bench-scale unit ADAM I [162]. The methanation plant ADAM I consisted of three adiabatic fixed bed methanation reactors including recycle according to the TREMP process. As shown in Table A.1, a good agreement is observed between the experimental data and results predicted from the proposed model. The feeding gas flow rate is 535 Nm^3/h (composition is 65.45% mol H_2, 9.84% mol CO, 8.96% mol CO_2, 11.3% mol CH_4), at 300 °C and 27.3 bar.

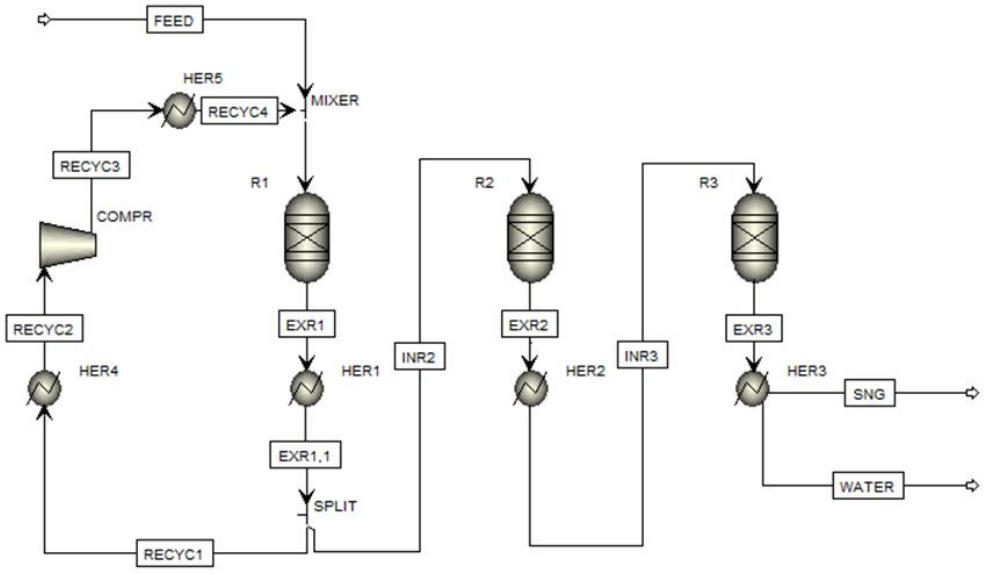

Figure A.1 – Flowsheet of the methanation process model.

Table A.1 – Simulation results compared with experimental data of ADAM I.

	R1 Inlet		R1 Exit		R2 Exit		R3 Exit		SNG	
	[30]	model	[30]	model	[30]	model	[30]	model	[30]	model

Temperature [°C]	300	299	604	595	451	451	303	302	23	23
Pressure [bar]	27.2	27.3	27.1	27.1	27.05	27.05	27	27	27	27
Flow rate [Nm^3/h]	1416	1416.0	1255	1252.0	348	346.6	334	336.2	191	190.4
Gas composition [vol. %]										
H_2	36.88	36.74	20.96	19.29	8.10	7.50	1.77	1.63	3.11	2.88
CO	4.28	4.30	1.17	0.94	0.00	0.05	0.00	0.00	0.00	0.00
CO_2	6.13	5.93	4.46	4.09	2.07	1.81	0.95	0.37	1.67	0.66
CH_4	28.12	28.16	37.44	38.40	44.36	44.64	47.28	47.55	82.95	83.96
H_2O	19.19	19.25	29.82	30.94	38.84	39.21	43.06	43.45	0.10	0.14
N_2	5.41	5.61	6.15	6.35	6.64	6.80	6.93	7.00	12.16	12.37

A.1 The storage control strategy flow chart

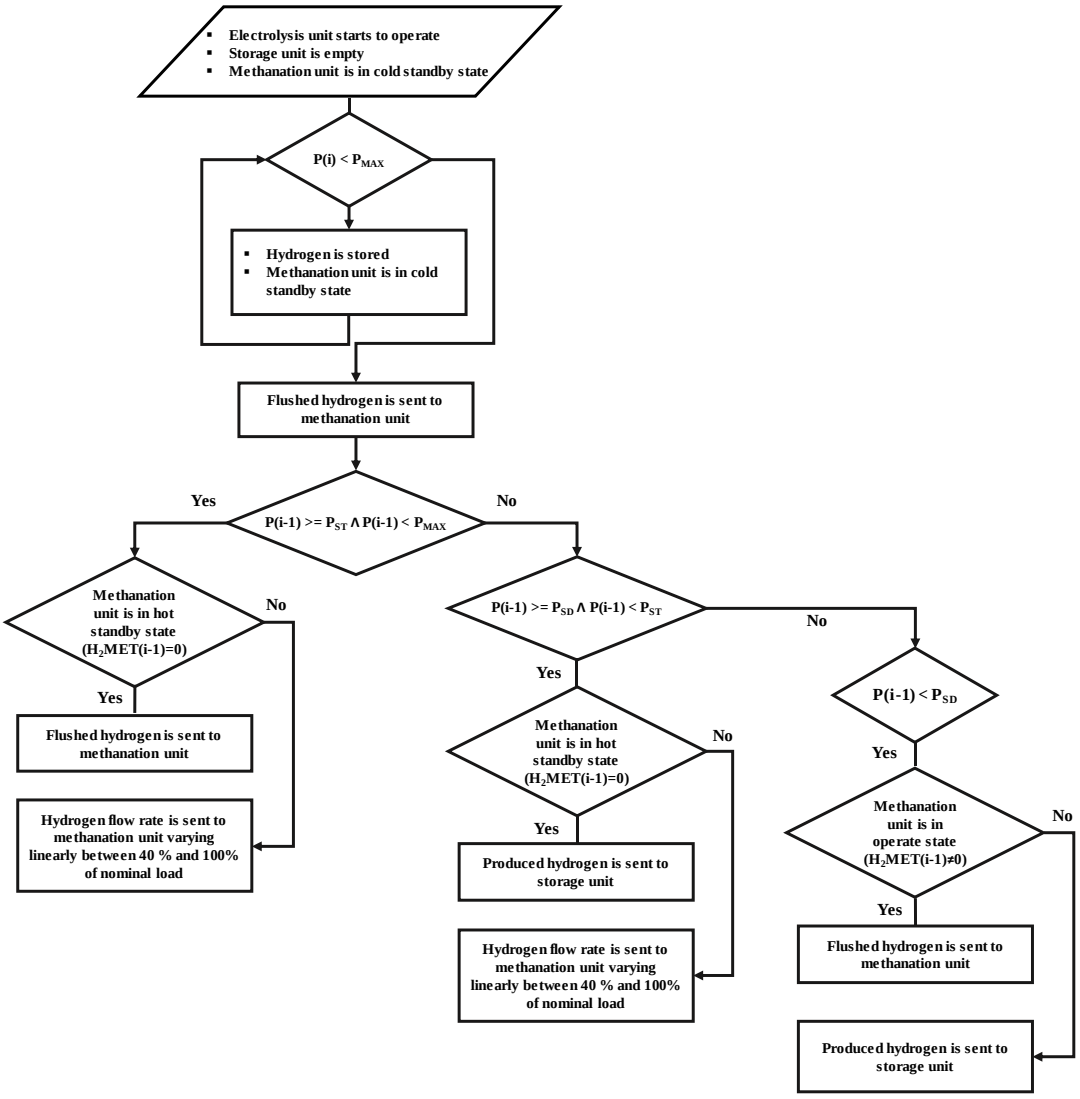

Figure A.2 – Flowchart of the storage control strategy.

APPENDIX B

Methanation Unit Modelling

The methanation unit has been modelled by using Aspen Plus software. The flowsheet of the model is shown in Figure B.0.1. Adiabatic Plug Flow Reactor (PFR) blocks have been used to simulate the methanation process. The thermodynamic and transport properties of the components are calculated using the RKSMHV2 property method. This property method, based on the Redlich–Kwong–Soave equation of state with modified Huron–Vidal mixing rules, is used for mixtures of non-polar and polar compounds, in combination with light gases.

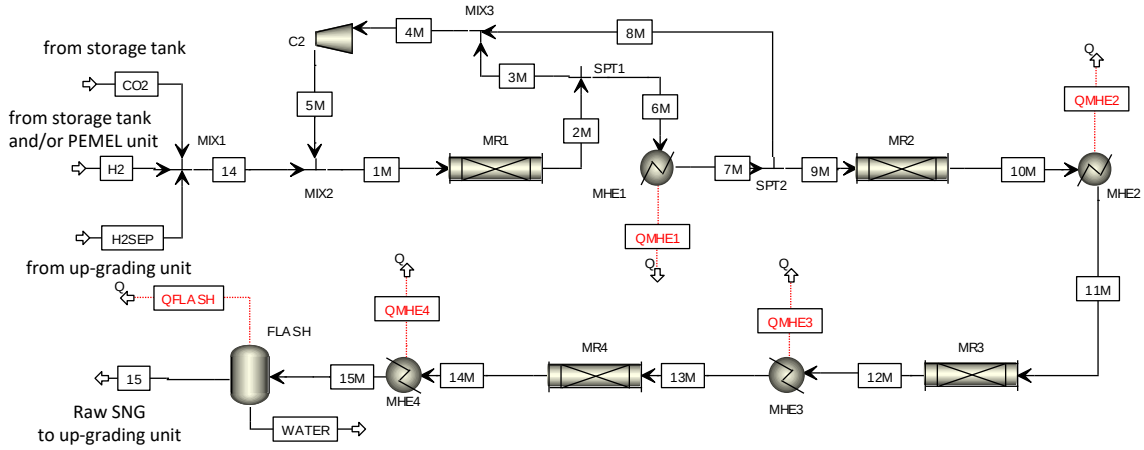

Figure B.0.1 – Flowsheet of CO_2 methanation unit.

The kinetic model developed by Xu and Froment has been applied to calculate the catalytic reaction rates as in [72].

The following three reaction are considered:

CO methanation:

$$CO + 3H_2 \rightarrow CH_4 + H_2O \qquad \Delta H^0_{298} = -206\ kJ/mol \qquad \text{(B.1)}$$

CO_2 methanation:

$$CO_2 + 4H_2 \rightarrow CH_4 + 2H_2O \qquad \Delta H^0_{298} = -165\ kJ/mol \tag{B.2}$$

Water gas shift:

$$CO_2 + H_2 \rightarrow CH_4 + H_2O \qquad \Delta H^0_{298} = +41\ kJ/mol \tag{B.3}$$

The corresponding rate equations are given by the equations below, whose kinetic parameter values are summarized in Table A1.

CO methanation:

$$r_1 = \frac{k_1}{p_{H_2}^{2.5}} \cdot \frac{p_{CH_4} \cdot p_{H_2O} - \frac{p_{H_2}^3 \cdot p_{CO}}{K_1}}{DEN^2} \tag{B.4}$$

CO_2 methanation:

$$r_2 = \frac{k_2}{p_{H_2}^{3.5}} \cdot \frac{p_{CO} \cdot p_{H_2O}^2 - \frac{p_{H_2}^4 \cdot p_{CO_2}}{K_2}}{DEN^2} \tag{B.5}$$

Water gas shift:

$$r_3 = \frac{k_3}{p_{H_2}} \cdot \frac{p_{CO} \cdot p_{H_2O} - \frac{p_{H_2} \cdot p_{CO_2}}{K_3}}{DEN^2} \tag{B.6}$$

where:

$$DEN = 1 + K_{CO}p_{CO} + K_{H_2}p_{H_2} + K_{CH_4}p_{CH_4} + \frac{K_{H_2O}p_{H_2O}}{p_{H_2}} \tag{B.7}$$

The pre-exponential factors $A(k_i)$ and $A(K_j)$ are determined from $k_{i,T}$ and $K_{j,T}$, while E_i and ΔH_j values can be calculated by the Arrhenius and van't Hoff equations:

$$k_i = A(k_{i,T}) \cdot \exp\left(\frac{-E_i}{RT}\right) \tag{B.8}$$

$$K_i = A(K_{i,T}) \cdot \exp\left(\frac{-\Delta H_i}{RT}\right) \tag{B.9}$$

$$K_j = A(K_{j,T}) \cdot \exp\left(\frac{-\Delta H_j}{RT}\right) \tag{B.10}$$

$$A(k_i) = k_{i,T} \cdot \exp\left(\frac{E_i}{RT}\right) \tag{B.11}$$

$$A(K_j) = K_{j,T} \cdot \exp\left(\frac{\Delta H_j}{RT}\right) \quad \text{(B.12)}$$

where:

- i = 1,2,3 and j = CH_4, H_2O, CO, H_2;
- k_1, k_2, k_3 are the rate coefficient of Eqs. (B.5) – (B.7), respectively;
- K_1, K_2, K_3 are the rate coefficient of Eqs. (B.5) – (B.7), respectively;
- $K_{CH_4}, K_{CO}, K_{H_2}$ are the adsorption constants of reaction for CH_4, CO and H_2;
- K_{H_2O} is the desorption constant of H_2O;
- $A(k_i)$ is pre-exponential factor of the rate coefficient, k_i;
- $A(K_j)$ is pre-exponential factor of the rate coefficient, K_j;
- E_i is the activation energy of reaction *i*-th;
- ΔH_j is the enthalpy change of reaction or adsorption;
- p is the partial pressure.

Table B.0.1 – Parameters of the reaction rate by Xu and Froment [163].

Parameter	Value
$A(k_1)$ [kmol bar^1 kg$_{cat}^{-1}$ h^{-1}]	$4.225 \cdot 10^{15}$
$A(k_2)$ [kmol bar$^{1/2}$ kg$_{cat}^{-1}$ h^{-1}]	$1.020 \cdot 10^{15}$
$A(k_3)$ [kmol bar$^{1/2}$ kg$_{cat}^{-1}$ h^{-1}]	$1.955 \cdot 10^{6}$
$A(K_{CH_4})$ [bar^{-1}]	$6.65 \cdot 10^{-4}$
$A(K_{H_2})$ [bar^{-1}]	$6.12 \cdot 10^{-9}$
$A(K_{CO})$, [bar^{-1}]	$8.23 \cdot 10^{-5}$
$A(K_{H_2O})$	$1.77 \cdot 10^{5}$
$A(K_1)$ [bar^2]	$5.375 \cdot 10^{10}$
$A(K_2)$ [bar^2]	$4.707 \cdot 10^{12}$
$A(K_3)$	$1.142 \cdot 10^{-2}$
E_1 [kJ mol^{-1}]	240.1
E_2 [kJ mol^{-1}]	243.9
E_3 [kJ mol^{-1}]	67.13
ΔH_1 [kJ mol^{-1}]	−206.1
ΔH_2 [kJ mol^{-1}]	−165.0
ΔH_3 [kJ mol^{-1}]	+41.15
ΔH_{CH_4} [kJ mol^{-1}]	−38.28
ΔH_{H_2} [kJ mol^{-1}]	−82.90
ΔH_{H_2O} [kJ mol^{-1}]	88.68
ΔH_{CO} [kJ mol^{-1}]	−70.65

REFERENCES

[1] European Commission. Communication from the Commission to the European Parliament, the Council, the European Economic and Social Committee and the Committee of the Regions Commission Work Programme 2017 Delivering a Europe That Protects, Empowers and Defends COM/2016/0710 Final 2019. Available online at: https://eur-lex.europa.eu/resource.html?uri=cellar:b828d165-1c22-11ea-8c1f-01aa75ed71a1.0006.02/DOC_1&format=PDF (last accessed on 26 May 2022).

[2] Directive (EU) 2018/2001 of the European Parliament and of the Council of 11 December 2018 on the Promotion of the Use of Energy from Renewable Sources. Official Journal of the European Union, L328/82, Brussels, Belgium, 2018. Available online at: https://eur-lex.europa.eu/legal-content/EN/TXT/PDF/?uri=CELEX:32018L2001&from=EN (last accessed on 26 May 2022).

[3] European Commission. European Green Deal: Commission proposes transformation of EU economy and society to meet climate ambitions. Available online at: https://ec.europa.eu/info/sites/default/files/european-green-deal-communication_en.pdf (last access on 26 May 2022).

[4] COM(2005) 576 final GREEN PAPER ON A EUROPEAN PROGRAMME FOR CRITICAL INFRASTRUCTURE PROTECTION 2005.

[5] Gasser P, Lustenberger P, Cinelli M, Kim W, Spada M, Burgherr P, et al. A review on resilience assessment of energy systems. Sustainable and Resilient Infrastructure 2021;6:273–99. https://doi.org/10.1080/23789689.2019.1610600.

[6] Holling CS. Resilience and Stability of Ecological Systems. Annu Rev Ecol Syst 1973;4:1–23. https://doi.org/10.1146/annurev.es.04.110173.000245.

[7] Bruneau M, Chang SE, Eguchi RT, Lee GC, O'Rourke TD, Reinhorn AM, et al. A Framework to Quantitatively Assess and Enhance the Seismic Resilience of Communities. Earthquake Spectra 2003;19:733–52. https://doi.org/10.1193/1.1623497.

[8] Zio E. Challenges in the vulnerability and risk analysis of critical infrastructures. Reliability Engineering & System Safety 2016;152:137–50. https://doi.org/10.1016/j.ress.2016.02.009.

[9] US Department of Homeland Security. National infrastructure protection plan, partnering to enhance protection and resiliency 2009.

[10] NIAC. CRITICAL INFRASTRUCTURE RESILIENCE FINAL REPORT AND RECOMMENDATIONS 2009.

[11] American Society of Mechanical Engineers (ASME). Innovative Technological Institute (ITI). Washington, D.C.: ASME ITI, LLC; 2009.

[12] Haimes YY, Crowther K, Horowitz BM. Homeland security preparedness: Balancing protection with resilience in emergent systems. Syst Engin 2008;11:287–308. https://doi.org/10.1002/sys.20101.
[13] Vugrin, E. D., Warren, D. E., Ehlen, M. A., & Camphouse, R. C. (2010). A framework for assessing the resilience of infra n.d.
[14] Alessandri A, Filippini R. Evaluation of Resilience of Interconnected Systems Based on Stability Analysis. vol. 7722, 2013. https://doi.org/10.1007/978-3-642-41485-5_16.
[15] Hollnagel E, Woods DD, Leveson N, editors. Resilience engineering: concepts and precepts. Aldershot, England ; Burlington, VT: Ashgate; 2006.
[16] Erker S, Stangl R, Stoeglehner G. Resilience in the light of energy crises – Part I: A framework to conceptualise regional energy resilience. Journal of Cleaner Production 2017;164:420–33. https://doi.org/10.1016/j.jclepro.2017.06.163.
[17] Liu W, Song Z. Review of studies on the resilience of urban critical infrastructure networks. Reliability Engineering & System Safety 2020;193:106617. https://doi.org/10.1016/j.ress.2019.106617.
[18] Esposito S, Giovinazzi S, Elefante L, Iervolino I. Performance of the L'Aquila (central Italy) gas distribution network in the 2009 ($$\mathrm{{M}}_\mathrm{{w}}$$ M w 6.3) earthquake. Bull Earthquake Eng 2013;11:2447–66. https://doi.org/10.1007/s10518-013-9478-8.
[19] Ellison, James F., et al. Natural Gas Network Resiliency to a "Shakeout Scenario" Earthquake. 2013 n.d.
[20] Carvalho R, Buzna L, Bono F, Masera M, Arrowsmith DK, Helbing D. Resilience of Natural Gas Networks during Conflicts, Crises and Disruptions. PLoS ONE 2014;9:e90265. https://doi.org/10.1371/journal.pone.0090265.
[21] Cimellaro GP, Villa O, Bruneau M. Resilience-Based Design of Natural Gas Distribution Networks. J Infrastruct Syst 2015;21:05014005. https://doi.org/10.1061/(ASCE)IS.1943-555X.0000204.
[22] Golara A, Esmaeily A. Quantification and Enhancement of the Resilience of Infrastructure Networks. J Pipeline Syst Eng Pract 2017;8:04016013. https://doi.org/10.1061/(ASCE)PS.1949-1204.0000250.
[23] Wadhawan Y, Neuman C. Evaluating Resilience of Gas Pipeline Systems Under Cyber-Physical Attacks: A Function-Based Methodology. Proceedings of the 2nd ACM Workshop on Cyber-Physical Systems Security and Privacy - CPS-SPC '16, Vienna, Austria: ACM Press; 2016, p. 71–80. https://doi.org/10.1145/2994487.2994488.
[24] Hauser P, Hobbie H, Most D. Resilience in the German natural gas network: Modelling approach for a high-resolution natural gas system. 2017 14th International Conference on the European Energy Market (EEM), Dresden, Germany: IEEE; 2017, p. 1–6. https://doi.org/10.1109/EEM.2017.7981942.
[25] Kyriakidis M, Lustenberger P, Burgherr P, Dang VN, Hirschberg S. Quantifying Energy Systems Resilience-A Simulation Approach to Assess Recovery. Energy Technol 2018;6:1700–6. https://doi.org/10.1002/ente.201700841.
[26] Su H, Zio E, Zhang Z-J, Xiong C-Z, Dai Q-S, Wu Q-W, et al. Development of an integrated dynamic model for supply security and resilience analysis of natural

gas pipeline network systems. Petroleum Science 2021:S1995822621000972. https://doi.org/10.1016/j.petsci.2021.10.002.
[27] Marino A, Zio E. A framework for the resilience analysis of complex natural gas pipeline networks from a cyber-physical system perspective. Computers & Industrial Engineering 2021;162:107727. https://doi.org/10.1016/j.cie.2021.107727.
[28] UNI 10576, 2018. Gas Pipelines Protection during Undergrounds Works.
[29] Ficco G. Metrological performance of diaphragm gas meters in distribution networks. Flow Measurement and Instrumentation 2014;37:65–72. https://doi.org/10.1016/j.flowmeasinst.2014.03.005.
[30] Ficco G, Celenza L, Dell'Isola M, Frattolillo A, Vigo P. Experimental evaluation of thermal mass smart meters influence factors. Journal of Natural Gas Science and Engineering 2016;32:556–65. https://doi.org/10.1016/j.jngse.2016.04.025.
[31] Canale L, Cortellessa G, Dell'Isola M, Ficco G, Frattolillo A, Zuena F, et al. A comparative analysis among Standard Load Profiles for Natural Gas consumption simulation at urban scale, Rome, Italy: 2019. https://doi.org/10.26868/25222708.2019.210602.
[32] Coelho PM, Pinho C. Considerations about equations for steady state flow in natural gas pipelines. J Braz Soc Mech Sci & Eng 2007;29:262–73. https://doi.org/10.1590/S1678-58782007000300005.
[33] Osiadacz AJ, Pienkosz K. Methods of steady-state simulation for gas networks. International Journal of Systems Science 1988;19:1311–21. https://doi.org/10.1080/00207728808547163.
[34] SIEMENS AG. PSS SINCAL 10.0 GAS, Gas Calculation in Pipe Networks n.d.
[35] Elaoud S, Hafsi Z, Hadj-Taieb L. Numerical modelling of hydrogen-natural gas mixtures flows in looped networks. Journal of Petroleum Science and Engineering 2017;159:532–41. https://doi.org/10.1016/j.petrol.2017.09.063.
[36] Brkić D. Iterative Methods for Looped Network Pipeline Calculation. Water Resour Manage 2011;25:2951–87. https://doi.org/10.1007/s11269-011-9784-3.
[37] Brkić D, Praks P. An Efficient Iterative Method for Looped Pipe Network Hydraulics Free of Flow-Corrections. Fluids 2019;4:73. https://doi.org/10.3390/fluids4020073.
[38] Brkić D, Praks P. Short Overview of Early Developments of the Hardy Cross Type Methods for Computation of Flow Distribution in Pipe Networks. Applied Sciences 2019;9:2019. https://doi.org/10.3390/app9102019.
[39] Kinsman P, Lewis J, Great Britain, Health and Safety Executive. Report on a study of international pipeline accidents. Great Britain, Health and Safety Executive; 2000.
[40] API. API RP 581, Recommended Practice 581, Risk Based Resource Document 2000.
[41] EGIG. 9th Report of the European Gas Pipeline Incident Data Group (period 1970 – 2013) 2015.
[42] Goodfellow GD, Lyons DCJ, Haswell DJV. UKOPA Pipeline Product Loss Incidents and Faults Report (1962 – 2016) 2018.

[43] Han ZY, Weng WG. An integrated quantitative risk analysis method for natural gas pipeline network. Journal of Loss Prevention in the Process Industries 2010;23:428–36. https://doi.org/10.1016/j.jlp.2010.02.003.
[44] Han ZY, Weng WG. Comparison study on qualitative and quantitative risk assessment methods for urban natural gas pipeline network. Journal of Hazardous Materials 2011;189:509–18. https://doi.org/10.1016/j.jhazmat.2011.02.067.
[45] Mazza A, Bompard E, Chicco G. Applications of power to gas technologies in emerging electrical systems. Renewable and Sustainable Energy Reviews 2018;92:794–806. https://doi.org/10.1016/j.rser.2018.04.072.
[46] Götz M, Lefebvre J, Mörs F, McDaniel Koch A, Graf F, Bajohr S, et al. Renewable Power-to-Gas: A technological and economic review. Renewable Energy 2016;85:1371–90. https://doi.org/10.1016/j.renene.2015.07.066.
[47] MARCOGAZ. Overview of test results and regulatory limits for hydrogen admission into existing natural gas infrastructure and end use 2019.
[48] Vandewalle J, Bruninx K, D'haeseleer W. Effects of large-scale power to gas conversion on the power, gas and carbon sectors and their interactions. Energy Conversion and Management 2015;94:28–39. https://doi.org/10.1016/j.enconman.2015.01.038.
[49] Blanco H, Nijs W, Ruf J, Faaij A. Potential of Power-to-Methane in the EU energy transition to a low carbon system using cost optimization. Applied Energy 2018;232:323–40. https://doi.org/10.1016/j.apenergy.2018.08.027.
[50] Götz M, Lefebvre J, Mörs F, McDaniel Koch A, Graf F, Bajohr S, et al. Renewable Power-to-Gas: A technological and economic review. Renewable Energy 2016;85:1371–90. https://doi.org/10.1016/j.renene.2015.07.066.
[51] Graf F, Götz M, Henel M, Schaaf T, Tichler R. Technoökonomische Studie von Power-to-Gas-Konzepten. 2014.
[52] Lehner M, Tichler R, Steinmüller H, Koppe M. Power-to-Gas: Technology and Business Models. 1st ed. 2014. Cham: Springer International Publishing : Imprint: Springer; 2014. https://doi.org/10.1007/978-3-319-03995-4.
[53] Gassner M, Maréchal F. Thermo-economic process model for thermochemical production of Synthetic Natural Gas (SNG) from lignocellulosic biomass. Biomass and Bioenergy 2009;33:1587–604. https://doi.org/10.1016/j.biombioe.2009.08.004.
[54] E&E Consultant. Etude portant sur l'hydrogène et la méthanation comme procédé de valorisation de l'électricité excédentaire. 2014.
[55] Zauner A, Böhm H, Rosenfeld DC, Tichler R. Innovative large-scale energy storage technologies and Power-to-Gas concepts after optimization - D7.7 - Analysis on future technology options and on techno-economic optimization. 2019.
[56] Bhandari R, Trudewind CA, Zapp P. Life cycle assessment of hydrogen production via electrolysis – a review. Journal of Cleaner Production 2014;85:151–63. https://doi.org/10.1016/j.jclepro.2013.07.048.
[57] Schmidt O, Gambhir A, Staffell I, Hawkes A, Nelson J, Few S. Future cost and performance of water electrolysis: An expert elicitation study. International Journal of Hydrogen Energy 2017;42:30470–92. https://doi.org/10.1016/j.ijhydene.2017.10.045.

[58] Ursua A, Gandia LM, Sanchis P. Hydrogen Production From Water Electrolysis: Current Status and Future Trends. Proc IEEE 2012;100:410–26. https://doi.org/10.1109/JPROC.2011.2156750.
[59] Wang M, Wang Z, Gong X, Guo Z. The intensification technologies to water electrolysis for hydrogen production – A review. Renewable and Sustainable Energy Reviews 2014;29:573–88. https://doi.org/10.1016/j.rser.2013.08.090.
[60] Carmo M, Fritz DL, Mergel J, Stolten D. A comprehensive review on PEM water electrolysis. International Journal of Hydrogen Energy 2013;38:4901–34. https://doi.org/10.1016/j.ijhydene.2013.01.151.
[61] Schiebahn S, Grube T, Robinius M, Tietze V, Kumar B, Stolten D. Power to gas: Technological overview, systems analysis and economic assessment for a case study in Germany. International Journal of Hydrogen Energy 2015;40:4285–94. https://doi.org/10.1016/j.ijhydene.2015.01.123.
[62] Ghaib K, Ben-Fares F-Z. Power-to-Methane: A state-of-the-art review. Renewable and Sustainable Energy Reviews 2018;81:433–46. https://doi.org/10.1016/j.rser.2017.08.004.
[63] Schaaf T, Grünig J, Schuster MR, Rothenfluh T, Orth A. Methanation of CO2 - storage of renewable energy in a gas distribution system. Energ Sustain Soc 2014;4:2. https://doi.org/10.1186/s13705-014-0029-1.
[64] Lehner M, Tichler R, Steinmüller H, Koppe M. Power-to-Gas: Technology and Business Models. Cham: Springer International Publishing; 2014. https://doi.org/10.1007/978-3-319-03995-4.
[65] Bailera M, Lisbona P, Romeo LM, Espatolero S. Power to Gas projects review: Lab, pilot and demo plants for storing renewable energy and CO2. Renewable and Sustainable Energy Reviews 2017;69:292–312. https://doi.org/10.1016/j.rser.2016.11.130.
[66] Kopyscinski J. Production of synthetic natural gas in a fluidized bed reactor: understanding the hydrodynamic, mass transfer, and kinetic effects. ETH Zurich, 2010. https://doi.org/10.3929/ETHZ-A-006031831.
[67] Haldor Topsøe. From solid fuels to substitute natural gas (SNG) using TREMP. 2008.
[68] Neubert M. Franz., Catalytic Methanation for Small- and Mid-Scale SNG Production. ProQuest Dissertations Publishing. 202 n.d.
[69] Rönsch S, Schneider J, Matthischke S, Schlüter M, Götz M, Lefebvre J, et al. Review on methanation – From fundamentals to current projects. Fuel 2016;166:276–96. https://doi.org/10.1016/j.fuel.2015.10.111.
[70] Schildhauer TJ, Biollaz SM, editors. Synthetic natural gas from coal, dry biomass, and power-to-gas applications. Hoboken, New Jersey: Wiley; 2016.
[71] Porubova J, Bazbauers G, Markova D. Modeling of the Adiabatic and Isothermal Methanation Process. Scientific Journal of Riga Technical University Environmental and Climate Technologies 2011;6. https://doi.org/10.2478/v10145-011-0011-5.
[72] Chauvy R, Dubois L, Lybaert P, Thomas D, De Weireld G. Production of synthetic natural gas from industrial carbon dioxide. Applied Energy 2020;260:114249. https://doi.org/10.1016/j.apenergy.2019.114249.

[73] Gorre J, Ruoss F, Karjunen H, Schaffert J, Tynjälä T. Cost benefits of optimizing hydrogen storage and methanation capacities for Power-to-Gas plants in dynamic operation. Applied Energy 2020;257:113967. https://doi.org/10.1016/j.apenergy.2019.113967.
[74] Gorre J, Ortloff F, van Leeuwen C. Production costs for synthetic methane in 2030 and 2050 of an optimized Power-to-Gas plant with intermediate hydrogen storage. Applied Energy 2019;253:113594. https://doi.org/10.1016/j.apenergy.2019.113594.
[75] Salomone F, Giglio E, Ferrero D, Santarelli M, Pirone R, Bensaid S. Techno-economic modelling of a Power-to-Gas system based on SOEC electrolysis and CO2 methanation in a RES-based electric grid. Chemical Engineering Journal 2019;377:120233. https://doi.org/10.1016/j.cej.2018.10.170.
[76] European Commission. Horizon 2020-Programme Fuel Cells and Hydrogen Joint Undertaking (Fch 2 Ju) Topic H2020-Jti-Fch-201. Available online at: https://www.fch.europa.eu/sites/default/files/AWP%202020.pdf (last accessed on 26 May 2022).
[77] Dannesboe C, Hansen JB, Johannsen I. Catalytic methanation of CO_2 in biogas: experimental results from a reactor at full scale. React Chem Eng 2020;5:183–9. https://doi.org/10.1039/C9RE00351G.
[78] Frank E, Gorre J, Ruoss F, Friedl MJ. Calculation and analysis of efficiencies and annual performances of Power-to-Gas systems. Applied Energy 2018;218:217–31. https://doi.org/10.1016/j.apenergy.2018.02.105.
[79] Van Leeuwen C, Zauner A. D8.3 - Report on the costs involved with PtG technologies and their potentials across the EU. Brussels: EU Horizon 2020 Project STORE&GO; 2018.
[80] Tschiggerl K, Sledz C, Topic M. Considering environmental impacts of energy storage technologies: A life cycle assessment of power-to-gas business models. Energy 2018;160:1091–100. https://doi.org/10.1016/j.energy.2018.07.105.
[81] Fendt S, Buttler A, Gaderer M, Spliethoff H. Comparison of synthetic natural gas production pathways for the storage of renewable energy: Comparison of synthetic natural gas production pathways. WIREs Energy Environ 2016;5:327–50. https://doi.org/10.1002/wene.189.
[82] Perna A, Moretti L, Ficco G, Spazzafumo G, Canale L, Dell'Isola M. SNG Generation via Power to Gas Technology: Plant Design and Annual Performance Assessment. Applied Sciences 2020;10:8443. https://doi.org/10.3390/app10238443.
[83] Inkeri E, Tynjälä T, Karjunen H. Significance of methanation reactor dynamics on the annual efficiency of power-to-gas -system. Renewable Energy 2021;163:1113–26. https://doi.org/10.1016/j.renene.2020.09.029.
[84] European Commission. A hydrogen strategy for a climate-neutral Europe COM(2020) 301 final 2020. Available online at: https://ec.europa.eu/energy/sites/ener/files/hydrogen_strategy.pdf (last accessed on 26 May 2022).
[85] Messaoudani Z labidine, Rigas F, Binti Hamid MD, Che Hassan CR. Hazards, safety and knowledge gaps on hydrogen transmission via natural gas grid: A

critical review. International Journal of Hydrogen Energy 2016;41:17511–25. https://doi.org/10.1016/j.ijhydene.2016.07.171.
[86] Witkowski A, Rusin A, Majkut M, Stolecka K. Analysis of compression and transport of the methane/hydrogen mixture in existing natural gas pipelines. International Journal of Pressure Vessels and Piping 2018;166:24–34. https://doi.org/10.1016/j.ijpvp.2018.08.002.
[87] Stetsenko AA, Nedzelsky SD, Naumenko VA. The effect of hydrogen on the physical properties of natural gas and the metrological characteristics of its metering systems. Metrolog and Instr 2020:45–50. https://doi.org/10.33955/2307-2180(6)2019.45-50.
[88] DVGW (Hg.): Entwicklung von modularen Konzepten zur Erzeugung, Speicherung und Einspeisung von Wasserstoff und Methan ins Erdgasnetz.
[89] Iskov H, Jensen J. Field test of hydrogen in the natural gas grid, Amsterdam: 2006.
[90] Dehaeseleer J. The effects of injecting hydrogen (renewable gases) 2018.
[91] Jaworski J, Kułaga P, Blacharski T. Study of the Effect of Addition of Hydrogen to Natural Gas on Diaphragm Gas Meters. Energies 2020;13:3006. https://doi.org/10.3390/en13113006.
[92] Jaworski J, Dudek A. Study of the Effects of Changes in Gas Composition as Well as Ambient and Gas Temperature on Errors of Indications of Thermal Gas Meters. Energies 2020;13:5428. https://doi.org/10.3390/en13205428.
[93] Instytut Nafty i Gazu – Państwowy Instytut Badawczy, Łach M. Dokładność wyznaczania współczynnika ściśliwości gazu z podwyższoną zawartością wodoru – porównanie metod obliczeniowych. NG 2016;72:329–38. https://doi.org/10.18668/NG.2016.05.04.
[94] UNI EN ISO 6976:2017 Natural gas - Calculation of calorific values, density, relative density and Wobbe indices from composition.
[95] Ludwig's Applied Process Design for Chemical and Petrochemical Plants. Elsevier; 2007. https://doi.org/10.1016/B978-0-7506-7766-0.X5000-3.
[96] Coker AK, Ludwig EE. Ludwig's applied process design for chemical and petrochemical plants. 4th ed. Amsterdam ; Boston: Elsevier Gulf Professional Pub; 2007.
[97] AGA REPORT #10 (2003) Speed of Sound in Natural Gas and Other Related Hydrocarbon Gases.
[98] UNI EN ISO 12213-2:2010 Natural gas - Calculation of compression factor Calculation using molar-composition analysis.
[99] Jaeschke M, Humphreys AE. Standard GERG virial equation for field use: simplification of the input data requirements for the GERG virial equation; an alternative means of compressibility factor calculation for natural gases and similar mixtures. Als Ms. gedr. Düsseldorf: VDI-Verl; 1992.
[100] Farzaneh-Gord M, Mohseni-Gharyehsafa B, Toikka A, Zvereva I. Sensitivity of natural gas flow measurement to AGA8 or GERG2008 equation of state utilization. Journal of Natural Gas Science and Engineering 2018;57:305–21. https://doi.org/10.1016/j.jngse.2018.07.014.
[101] BS EN 14236:2018 Ultrasonic domestic gas meters n.d.

[102] International Organization of Legal Metrology. OIML R 137—1 & 2 International Recommendation. Gas Meters. Part 1 and Part 2.
[103] Available online at: https://www.inficon.com/en/products/micro-gc-fusion-gas-analyzer, (last accessed 26 May 2022).
[104] Available online at: https://www.intergaz.eu/produkty/analiza-jakosci-gazu/analizatory/chromatograf-encal-3000/, (last accessed 26 May 2022).
[105] Available online at: https://envag.com.pl/produkty/chromatografy-przemyslowe/chromatografy/przemyslowy-modulowy-chromatograf-gazowy-maxum-edy (last accessed 26 May 2022).
[106] Available online at: https://www.perkinelmer.com/pl/product/rga-column-set-with-h2-channel-n6107033, (last accessed 26 May 2022).
[107] Available online at: https://www.perkinelmer.com/pl/product/arnel-model-1115ppc590-narl8105, (last accessed 26 May 2022).
[108] Available online at: https://tools.thermofisher.com/content/sfs/brochures/BR-10484-Natural-Gas-Analyzers-BR10484-EN.pdf, (last accessed 26 May 2022).
[109] Available online at: https://www.thermofisher.com/order/catalog/product/NATGASC20211?SID=srch-srp-NATGASC20211, (last accessed 26 May 2022).
[110] Available online at: https://www.agilent.com/cs/library/applications/5991-0275EN.pdf, (last accessed 26 May 2022).
[111] Available online at: https://www.agilent.com/cs/library/brochures/5991-4156EN_LR.pdf, (last accessed 26 May 2022).
[112] Available online at: https://www.shimadzu.com/an/system-gc/n9j25k00000fndbr.html, (last accessed 26 May 2022).
[113] Available online at: https://www.shimadzu.com/an/products/gaschromatography/application specific-system-gc/natural-gas-analysis/index.html, (last accessed 26 May 2022).
[114] Basu P. Biomass gasification and pyrolysis: practical design and theory. Burlington, MA: Academic Press; 2010.
[115] Ramos A, Monteiro E, Rouboa A. Numerical approaches and comprehensive models for gasification process: A review. Renewable and Sustainable Energy Reviews 2019;110:188–206. https://doi.org/10.1016/j.rser.2019.04.048.
[116] Gagliano A, Nocera F, Patania F, Bruno M, Castaldo DG. A robust numerical model for characterizing the syngas composition in a downdraft gasification process. Comptes Rendus Chimie 2016;19:441–9. https://doi.org/10.1016/j.crci.2015.09.019.
[117] Patra TK, Sheth PN. Biomass gasification models for downdraft gasifier: A state-of-the-art review. Renewable and Sustainable Energy Reviews 2015;50:583–93. https://doi.org/10.1016/j.rser.2015.05.012.
[118] Sansaniwal SK, Pal K, Rosen MA, Tyagi SK. Recent advances in the development of biomass gasification technology: A comprehensive review. Renewable and Sustainable Energy Reviews 2017;72:363–84. https://doi.org/10.1016/j.rser.2017.01.038.
[119] Speight JG. Handbook of gasification technology: science, technology, and processes. Hoboken, NJ: Wiley-Scrivener; 2020.

[120] Hrbek J. Past, present and future of thermal gasification of biomass and waste. Acta Innovations 2020:5–20. https://doi.org/10.32933/ActaInnovations.35.1.
[121] Maroušek J, Maroušková A, Kůs T. Shower cooler reduces pollutants release in production of competitive cement substitute at low cost. Energy Sources, Part A: Recovery, Utilization, and Environmental Effects 2020:1–10. https://doi.org/10.1080/15567036.2020.1825560.
[122] Speight JG, TotalBoox, TBX. Gasification of Unconventional Feedstocks. Elsevier Science; 2014.
[123] Škapa S, Vochozka M. Waste energy recovery improves price competitiveness of artificial forage from rapeseed straw. Clean Techn Environ Policy 2019;21:1165–71. https://doi.org/10.1007/s10098-019-01697-x.
[124] Yang Y, Liew RK, Tamothran AM, Foong SY, Yek PNY, Chia PW, et al. Gasification of refuse-derived fuel from municipal solid waste for energy production: a review. Environ Chem Lett 2021;19:2127–40. https://doi.org/10.1007/s10311-020-01177-5.
[125] Mazaheri N, Akbarzadeh AH, Madadian E, Lefsrud M. Systematic review of research guidelines for numerical simulation of biomass gasification for bioenergy production. Energy Conversion and Management 2019;183:671–88. https://doi.org/10.1016/j.enconman.2018.12.097.
[126] Ahmed TY, Ahmad MM, Yusup S, Inayat A, Khan Z. Mathematical and computational approaches for design of biomass gasification for hydrogen production: A review. Renewable and Sustainable Energy Reviews 2012;16:2304–15. https://doi.org/10.1016/j.rser.2012.01.035.
[127] Baruah D, Baruah DC. Modeling of biomass gasification: A review. Renewable and Sustainable Energy Reviews 2014;39:806–15. https://doi.org/10.1016/j.rser.2014.07.129.
[128] Lenhard R, Malcho M, Jandačka J. Modelling of Heat Transfer in the Evaporator and Condenser of the Working Fluid in the Heat Pipe. Heat Transfer Engineering 2019;40:215–26. https://doi.org/10.1080/01457632.2018.1426225.
[129] Silva IP, Lima RMA, Silva GF, Ruzene DS, Silva DP. Thermodynamic equilibrium model based on stoichiometric method for biomass gasification: A review of model modifications. Renewable and Sustainable Energy Reviews 2019;114:109305. https://doi.org/10.1016/j.rser.2019.109305.
[130] Rodrigues R, Muniz AR, Marcilio NR. EVALUATION OF BIOMASS AND COAL CO-GASIFICATION OF BRAZILIAN FEEDSTOCK USING A CHEMICAL EQUILIBRIUM MODEL. Braz J Chem Eng 2016;33:401–14. https://doi.org/10.1590/0104-6632.20160332s00003479.
[131] Karmakar MK, Datta AB. Generation of hydrogen rich gas through fluidized bed gasification of biomass. Bioresource Technology 2011;102:1907–13. https://doi.org/10.1016/j.biortech.2010.08.015.
[132] Sharma P, Gupta B, Pandey M, Singh Bisen K, Baredar P. Downdraft biomass gasification: A review on concepts, designs analysis, modelling and recent advances. Materials Today: Proceedings 2020:S2214785320366785. https://doi.org/10.1016/j.matpr.2020.08.789.

[133] Safarian S, Unnþórsson R, Richter C. A review of biomass gasification modelling. Renewable and Sustainable Energy Reviews 2019;110:378–91. https://doi.org/10.1016/j.rser.2019.05.003.
[134] Puig-Arnavat M, Bruno JC, Coronas A. Review and analysis of biomass gasification models. Renewable and Sustainable Energy Reviews 2010;14:2841–51. https://doi.org/10.1016/j.rser.2010.07.030.
[135] Ferreira S, Monteiro E, Brito P, Vilarinho C. A Holistic Review on Biomass Gasification Modified Equilibrium Models. Energies 2019;12:160. https://doi.org/10.3390/en12010160.
[136] Zainal ZA, Ali R, Lean CH, Seetharamu KN. Prediction of performance of a downdraft gasifier using equilibrium modeling for different biomass materials. Energy Conversion and Management 2001;42:1499–515. https://doi.org/10.1016/S0196-8904(00)00078-9.
[137] Li XT, Grace JR, Lim CJ, Watkinson AP, Chen HP, Kim JR. Biomass gasification in a circulating fluidized bed. Biomass and Bioenergy 2004;26:171–93. https://doi.org/10.1016/S0961-9534(03)00084-9.
[138] Sharma S, Sheth PN. Air–steam biomass gasification: Experiments, modeling and simulation. Energy Conversion and Management 2016;110:307–18. https://doi.org/10.1016/j.enconman.2015.12.030.
[139] Jarungthammachote S, Dutta A. Thermodynamic equilibrium model and second law analysis of a downdraft waste gasifier. Energy 2007;32:1660–9. https://doi.org/10.1016/j.energy.2007.01.010.
[140] Baratieri M, Pieratti E, Nordgreen T, Grigiante M. Biomass Gasification with Dolomite as Catalyst in a Small Fluidized Bed Experimental and Modelling Analysis. Waste Biomass Valor 2010;1:283–91. https://doi.org/10.1007/s12649-010-9034-6.
[141] Barba D, Prisciandaro M, Salladini A, Mazziotti di Celso G. The Gibbs Free Energy Gradient Method for RDF gasification modelling. Fuel 2011;90:1402–7. https://doi.org/10.1016/j.fuel.2010.12.022.
[142] Barba D, Capocelli M, Cornacchia G, Matera DA. Theoretical and experimental procedure for scaling-up RDF gasifiers: The Gibbs Gradient Method. Fuel 2016;179:60–70. https://doi.org/10.1016/j.fuel.2016.03.014.
[143] Materazzi M, Lettieri P, Mazzei L, Taylor R, Chapman C. Thermodynamic modelling and evaluation of a two-stage thermal process for waste gasification. Fuel 2013;108:356–69. https://doi.org/10.1016/j.fuel.2013.02.037.
[144] Sreejith CC, Arun P, Muraleedharan C. Thermochemical Analysis of Biomass Gasification by Gibbs Free Energy Minimization Model—Part: I (Optimization of Pressure and Temperature). International Journal of Green Energy 2013;10:231–56. https://doi.org/10.1080/15435075.2011.653846.
[145] Kangas P, Hannula I, Koukkari P, Hupa M. Modelling super-equilibrium in biomass gasification with the constrained Gibbs energy method. Fuel 2014;129:86–94. https://doi.org/10.1016/j.fuel.2014.03.034.
[146] Mendiburu AZ, Carvalho JA, Coronado CJR. Thermochemical equilibrium modeling of biomass downdraft gasifier: Stoichiometric models. Energy 2014;66:189–201. https://doi.org/10.1016/j.energy.2013.11.022.

[147] Ratnadhariya JK, Channiwala SA. Experimental studies on molar distribution of CO/CO2 and CO/H2 along the length of downdraft wood gasifier. Energy Conversion and Management 2010;51:452–8. https://doi.org/10.1016/j.enconman.2009.10.007.
[148] Biagini E, Barontini F, Tognotti L. Development of a bi-equilibrium model for biomass gasification in a downdraft bed reactor. Bioresource Technology 2016;201:156–65. https://doi.org/10.1016/j.biortech.2015.11.057.
[149] Gambarotta A, Morini M, Zubani A. A non-stoichiometric equilibrium model for the simulation of the biomass gasification process. Applied Energy 2018;227:119–27. https://doi.org/10.1016/j.apenergy.2017.07.135.
[150] Zhou H, Long Y, Meng A, Li Q, Zhang Y. Classification of municipal solid waste components for thermal conversion in waste-to-energy research. Fuel 2015;145:151–7. https://doi.org/10.1016/j.fuel.2014.12.015.
[151] Zoski CG, editor. Handbook of electrochemistry. 1st ed. Amsterdam ; Boston: Elsevier; 2007.
[152] Petersen I, Werther J. Experimental investigation and modeling of gasification of sewage sludge in the circulating fluidized bed. Chemical Engineering and Processing: Process Intensification 2005;44:717–36. https://doi.org/10.1016/j.cep.2004.09.001.
[153] Shuen J. A Coupled Implicit Method for Chemical Non-equilibrium Flows at All Speeds. Journal of Computational Physics 1993;106:306–18. https://doi.org/10.1006/jcph.1993.1110.
[154] Vayenas CG, Debenedetti PG, Yentekakis I, Hegedus LL. Cross-flow, solid-state electrochemical reactors: a steady state analysis. Ind Eng Chem Fund 1985;24:316–24. https://doi.org/10.1021/i100019a007.
[155] Chapman S, Cowling TG, Park D. The Mathematical Theory of Non-Uniform Gases. American Journal of Physics 1962;30:389–389. https://doi.org/10.1119/1.1942035.
[156] Channiwala SA, Parikh PP. A unified correlation for estimating HHV of solid, liquid and gaseous fuels. Fuel 2002;81:1051–63. https://doi.org/10.1016/S0016-2361(01)00131-4.
[157] Silberberg MS, Licoccia S. Chimica: la natura molecolare della materia e delle sue trasformazioni. Milano: McGraw-Hill; 2016.
[158] Dogru M, Howarth CR, Akay G, Keskinler B, Malik AA. Gasification of hazelnut shells in a downdraft gasifier. Energy 2002;27:415–27. https://doi.org/10.1016/S0360-5442(01)00094-9.
[159] Jayah TH, Aye L, Fuller RJ, Stewart DF. Computer simulation of a downdraft wood gasifier for tea drying. Biomass and Bioenergy 2003;25:459–69. https://doi.org/10.1016/S0961-9534(03)00037-0.
[160] Plis P, Wilk RK. Theoretical and experimental investigation of biomass gasification process in a fixed bed gasifier. Energy 2011;36:3838–45. https://doi.org/10.1016/j.energy.2010.08.039.
[161] Antolini D, Ail SS, Patuzzi F, Grigiante M, Baratieri M. Experimental investigations of air-CO2 biomass gasification in reversed downdraft gasifier. Fuel 2019;253:1473–81. https://doi.org/10.1016/j.fuel.2019.05.116.

[162] Höhlein B, Niessen H, Range J, Schiebahn HJR, Vorwerk M. Methane from synthesis gas and operation of high-temperature methanation. Nuclear Engineering and Design 1984;78:241–50. https://doi.org/10.1016/0029-5493(84)90308-X.

[163] Xu J, Froment GF. Methane steam reforming, methanation and water-gas shift: I. Intrinsic kinetics. AIChE J 1989;35:88–96. https://doi.org/10.1002/aic.690350109.

LIST OF PUBLICATIONS

1. Moretti, L.; Arpino, F.; Cortellessa, G.; Dell'Isola, M.; Ficco, G.; Grossi, G.; Di Palma, M.; Vanoli L. Analytical and numerical modelling of biomass gasification in downdraft gasifiers. Accettato per la pubblicazione su Journal of Physics: Conference Series

2. Grossi, G.; Arpino, F.; Buonanno, G.; Cortellessa, G.; Moretti, L.; Nagano, H.; Stabile, L. A Eulerian-Lagrangian approach for the CFD analysis of airborne disease transmission in a car cabin. Accettato per la pubblicazione su Journal of Physics: Conference Series

3. Moretti, L.; Arpino, F.; Cortellessa, G.; Di Fraia, S.; Di Palma, M.; Vanoli, L. Reliability of Equilibrium Gasification Models for Selected Biomass Types and Compositions: An Overview. Energies 2021, 15, 61, doi:10.3390/en15010061

4. Dell'Isola, M.; Ficco, G.; Moretti, L.; Jaworski, J.; Kułaga, P.; Kukulska–Zając, E. Impact of Hydrogen Injection on Natural Gas Measurement. Energies 2021, 14, 8461, doi:10.3390/en14248461

5. Candelaresi, D.; Moretti, L.; Perna, A.; Spazzafumo, G. Heat Recovery from a PtSNG Plant Coupled with Wind Energy. Energies 2021, 14, 7660, doi:10.3390/en14227660

6. Dell'Isola, M.; Ficco, G.; Moretti, L.; Perna, A.; Candelaresi, D.; Spazzafumo, G. Impact of hydrogen injection on thermophysical properties and measurement reliability in natural gas networks. E3S Web of Conferences 2021, 312, 01004, https://doi.org/10.1051/e3sconf/202131201004

7. Arpino, F.; Canale, L.; Cortellessa, G.; D'Alessio, R.; Dell'Isola, M.; Ficco, G.; Moretti, L.; Vigo, P.; Zuena, F. Environmental Effect on Temperature Measurement in Natural Gas Network Balance. Journal of Physics: Conference Series 2021, 1868, 012028, doi:10.1088/1742-6596/1868/1/012028

8. Arpino, F.; Cortellessa, G.; Canale, L.; Dell'Isola, M.; Ficco, G.; Moretti, L.; Zuena, F.; Rinaldi, F. A 0D-3D Approach for Numerical Analysis of Waste to Energy Plants: A Case Study. Journal of Physics: Conference Series 2021, 1868, 012023, doi:10.1088/1742-6596/1868/1/012023

9. Perna, A.; Moretti, L.; Ficco, G.; Spazzafumo, G.; Canale, L.; Dell'Isola, M. SNG Generation via Power to Gas Technology: Plant Design and Annual Performance Assessment. Applied Sciences 2020, 10, 8443, doi:10.3390/app10238443

10. Dell'Isola, M.; Ficco, G.; Lavalle, L.; Moretti, L.; Tofani, A.; Zuena, F. A Resilience Assessment Simulation Tool for Distribution Gas Networks. Journal of Natural Gas Science and Engineering 2020, 84, 103680, doi:10.1016/j.jngse.2020.103680